FABRICATION AND MODELING OF HIGH EFFICIENCY AND STABILIZED P-TYPE PASSIVATED EMITTER REAR SILICON SOLAR CELLS (PERC)

A Dissertation
Presented to
The Academic Faculty

by

Eunhwan Cho

In Partial Fulfillment
of the Requirements for the Degree
Doctor of Philosophy in the
School of Electrical and Computer Engineering

Georgia Institute of Technology

FABRICATION AND MODELING OF HIGH EFFICIENCY AND STABILIZED P-TYPE PASSIVATED EMITTER REAR SILICON SOLAR CELLS (PERC)

Approved by:

Dr. Ajeet Rohatgi, Advisor
School of Electrical and Computer Engineering
Georgia Institute of Technology

Dr. Andrew F. Peterson
School of Electrical and Computer Engineering
Georgia Institute of Technology

Dr. Thomas K. Gaylord
School of Electrical and Computer Engineering
Georgia Institute of Technology

Dr. Haomin Zhou
School of Mathematics
Georgia Institute of Technology

Dr. Bernard Kippelen
School of Electrical and Computer Engineering
Georgia Institute of Technology

Date Approved: May 1, 2017

This work is dedicated to

my father, Cumsuk Cho,

my mother, Youngja Han,

my sister, Hyunju Cho,

and my wife, Go Eun Kim for all their love and support.

ACKNOWLEDGEMENTS

First and foremost, I would like to express my sincere gratitude to my advisor, Dr. Rohatgi, for the opportunity and resources to pursue my research. Dr. Rohatgi led me to develop a deeper understanding of solar cell physics and exposed me with a variety of topics and ideas. His advice and guide on my research encouraged me to learn more and become a better scientist. Also, I appreciate his tremendous time and support to finish this thesis. His advice on both research as well as on my career has been invaluable.

I would like to thank my committee members: Dr. Thomas K. Gaylord, Dr. Bernard Kippelen, Dr. Andrew F. Peterson and Dr. Haomin Zhou, not only for their time and service but also for the various view points on my research, insightful comments and suggestions which encouraged me to widen my research.

I am truly grateful to the former and current group members of the University Center of Excellence for Photovoltaics Research and Education (UCEP). Special thanks to Dr. Young-Woo Ok for his support, guidance and valuable discussions. I also acknowledge the gratitude to Dr. Kyungsun Ryu, Dr. Moon-Hee Kang, Dr. Yuguo Tao, Dr. Ian Cooper, Dr. John Renshaw, Dr. Jiun-Hong Lai, Dr. Chia-Wei Chen and Steven Ning for insightful technical discussions on solar cell physics and device modeling and sharing of their expertise on solar cell fabrication processes. I am grateful to Ajay Upadhyaya, Vijay Upadhyaya, Brian Rounsaville, John Keith Tate, Francesco Zimbardi, Charles Calloway, James Keane, Malka Kadish, Keenan Jones, Elizabeth Lori Chang and Devin Carter for their extensive assistance with equipment maintenance, active support and cooperation in research, and to Carla East for excellent administrative support with care and kindness. I am also thankful to Keeya Madini, Andrew Marcus Tam, Ying-Yuan Huang and Aditi Jain for their true relationship and generous support.

I would like to thank all Suniva R&D group members including Dr. Atul Gupta, Dr. Adam Payne, Dr. Vijay Yelunder, Dr. Arnab Das, Vinodh Chandrasekaran, Preston Davis, Liladhar Dahal, Linu Abraham, Julie Bixler and Threa Tan for their technical support and cooperation in my research.

I am grateful to SunEdison research scientists including M. Jeff Binns, Jason Guo, Jesse Appel and Henry Hieslmair, and Amtech company vice president, James Hwang for their support with excellent project opportunities and valuable technical discussions.

I would like to express appreciation to Jinwook Yang, Sanggyu Kim and Chanho Kim for their friendship throughout my Ph.D years. I am indebted to them for their advice and help whenever I was in need. I will miss traveling different countries together, walking on the campus for breeze, cooking food and discussing general topics which refreshed my mind.

Research in this thesis was supported by the U.S. Department of Energy, the Silicon Solar Consortium (SiSoC) and SunEdison corporation.

TABLE OF CONTENTS

LIST OF TABLES

LIST OF FIGURES

LIST OF SYMBOLS AND ABBREVIATIONS

2D	Two-dimensional
3D	Three-dimensional
AC	Alternating current
Ag	Silver
Al	Aluminium
Al_2O_3	Aluminium oxide
Al-BSF	Aluminum-back-surface field
ALD	Atomic layer deposition
AM1.5	Air mass 1.5
AR	Antireflection
ARC	Anti-reflection coating
ARCO	Atlantic Richfield Company
B	Boron
B-O	Boron-oxygen
BOS	Balance of System
BSF	Back surface field
BSR	Back surface reflectance
BSRV	Back surface recombination velocity
CCz	Continuous Cz
CO_2	Carbon dioxide
Cox	Oxide capacitance
C-V or CV	Capacitance-voltage
Cz	Czochralski
D	Carrier diffusivity

D_{amp}	Ambipolar diffusion coefficient
D_{it}	Interface state density
DC	Direct current
DI	Deionized
DOE	Department of Energy
η	Efficiency
E_c	Conduction band edge
E_g	Bandgap energy
E_t	Trap energy level
E_v	Valence band edge
ECV	Electrochemical capacitance-voltage
FF	Fill factor
FN tunneling	Fowler-Nordheim tunneling
Fraunhofer ISE	Fraunhofer Institute for Solar Energy Systems
FSF	Front surface field
FSRV	Front surface recombination velocity
FTIR	Fourier transform infrared spectroscopy
FZ	Float-zone
G	Generation rate
Ga	Gallium
GW	Gigawatt
HF	Hydrofluoric acid
HIT	Heterojunction with intrinsic thin-layer
I	Electric current
I_{mp}	Electric current at maximal power point
I_{sc}	Short circuit electric current
IBC	Interdigitated back contact

IEA	International Energy Agency
In	Indium
IPA	Isopropyl alcohol
IQE	Internal quantum efficiency
IR	Infrared
ITRPV	International Technology Roadmap for Photovoltaic
I-V	Electric current-voltage
$J_{ob,bulk}$	Bulk contribution of J_{ob}
J_{ob}	Base saturation current density
J_{ob}'	BSF contribution of J_{ob}
$J_{oe,field}$	Passivated field contribution of J_{oe}
$J_{oe,metal}$	Metal contribution of J_{oe}
J_{oe}	Emitter saturation current density
J_{rec}	Minority emitter recombination current
J_{sc}	Short-circuit current density
J_o	Saturation current density
$J'_{ob,field}$	Passivated field contribution of J_{ob}
$J'_{ob,metal}$	Metal contribution of J_{ob}
k or k_B	Boltzmann constant
KOH	Potassium hydroxide
KV	Kilovolt
kwh	Kilowatt-hour
L	Carrier diffusion length
LCOE	levelized cost of electricity
LID	Light-induced degradation
LIV	Light Electric current-voltage
μ	Carrier mobility

m_e	Electron rest mass
mc	Multi crystalline
MOS	Metaloxidesemiconductor
MW	Megawatt
Δn	Excess carrier density
n^+	Heavily phosphorus doped region
N_{base}	Base doping concentration
$N_{emitter}$	Emitter doping concentration
N_2	Nitrogen
N_A	Acceptor concentration
N_c	Electron effective density of states
N_D	Donor concentration
n_i	Intrinsic carrier concentration
n_s	Surface electron concentration
N_{ST}	Density of surface states
N_t	Density of trapping defects
N_v	Hole effective density of states
$NaNO_2$	Sodium Nitrite
Ns	Surface concentration
O_2	Oxygen
P	Phosphorus
P_{in}	Input power
P_{out}	Output power
p^+	Heavily boron doped
p_s	Surface hole concentration
PC1D	Personal computer one dimensional - device simulation
PECVD	Plasma enhanced chemical vapor deposition

PERC	Passivated emitter and rear cell
PERT	Passivated emitter, rear totally-diffused
PL	Photoluminescence
p-n junction	Positive-negative junction
$POCl_3$	Phosphoryl chloride (=phosphorus oxychloride)
PV	Photovoltaic
q	Electron charge
Q	Charge amount
Q_f	Fixed oxide charge density
QSSPC	Quasi-steady-state photoconductance
R_{bf} or R_{busbar}	Busbar resistance
R_{finger}	Metal gridline resistance
R_{sh}	Shunt-resistance
R_b or $R_{substrate}$	Base substrate resistance
R_c or $R_{contact}$	Contact resistance
R_e or $R_{emitter}$	Emitter resistance
R_R	Radiative recombination rate
R_s	Series-resistance
RF	Radio Frequency
σ_n	Electron capture cross section
σ_p	Hole capture cross section
S or SRV	Surface recombination velocity
S_{eff}	Effective back surface recombination velocity
S_{eff}	Effective surface recombination velocity
S_{no}	Surface recombination velocity for electron
S_{po}	Surface recombination velocity for hole
SEM	Scanning electron microscopy

Si	Silicon
SiN_x	Silicon nitride
SiO_2	Silicon oxide
SRH	Shockley-Read-Hall recombination
STC	Standard test conditions
τ	Minority carrier lifetime
τ_{Auger}	Intrinsic Auger minority carrier lifetime
τ_{bulk}	Bulk lifetime
τ_{eff}	Effective minority carrier lifetime
τ_{n0}	Electron lifetime
τ_{p0}	Hole lifetime
τ_{SRH}	Intrinsic SRH minority carrier lifetime
T	Temperature
TCAD	Technology Computer Aided Design
TMA	Trimethylaluminum
U	Volume recombination rate
U_{s1}	Surface recombination rate
UV	Ultraviolet
V	Voltage
V_{mp}	Voltage at maximal power point
V_{oc}	Open-circuit voltage
$V_{\mathrm{th,n}}$ or $V_{\mathrm{e,th}}$	Electron thermal velocity
$V_{\mathrm{th,n}}$ or $V_{\mathrm{h,th}}$	Hole thermal velocity
V_{th}	Thermal velocity
Vfb	Flat band voltage

SUMMARY

Since the industrial revolution, there has been a rapid increase in the world′s electricity consumption. This has brought about a large amount of CO_2 emission from the use of fossil fuels such as oil, coal and natural gas, causing global warming. Growing concern about global warming led to development of more alternative energy sources. Among the various renewable energy options available today, photovoltaics (PV) is most attractive because sunlight, the fuel for solar cells, is essentially unlimited, clean and free. The challenge with PV has been the cost, which has been declining rapidly but is still slightly more expensive than fossil fuels in most parts of the world. The cost of PV can be further reduced by increasing solar cell efficiency. Currently, most of the PV industry fabricates p-type boron doped silicon solar cells, which show 0.5-1% degradation in absolute efficiency after a few days of sunlight exposure. Reduction or elimination of this light-induced degradation can also reduce the cost of PV. Therefore, the goal of this thesis is to achieve low-cost high efficiency commercial ready screen-printed p-type silicon solar cells with little or no light-induced degradation by a combination of fundamental understanding of loss mechanisms and technological innovations.

In Chapter II of this thesis, physics and operating principle of silicon solar cells are reviewed including key solar cell parameters and optical and electrical loss mechanisms. Chapter III surveyed topics related to this thesis such as screen printing technology and light-induced degradation.

Chapter IV summarizes the in depth study of two promising emitter formation technologies, $POCl_3$ diffusion and phosphorus ion implantation were investigated to achieve higher cell efficiency. In this study, commercial size baseline cells with full Al-BSF solar cells were fabricated using widely used p-type single crystalline Cz Si wafers as well as cast multicrystalline Si wafers with some defects. Since high bulk

lifetime is crucial for higher efficiency and bulk lifetime is controlled by impurities and defects in Si, the ability of these two techniques to getter or extract impurities during processing was investigated. Formation of both $POCl_3$ diffused and ion implanted emitters showed the promise and ability to getter bulk impurities but the gettering efficiency of $POCl_3$ diffusion was found to be superior. This was the result of higher phosphorus concentration observed near the surface in $POCl_3$ diffused emitter, which creates more sites and misfit dislocations to provide a better sink for impurities near the surface. In addition, $POCl_3$ diffusion provides double side gettering during the diffusion process while ion implantation is done only on one side. This was confirmed by in-depth measurements and analysis of iron concentration in the bulk and bulk lifetime in the Cz and cast Si wafers before and after $POCl_3$ diffusion and phosphorus implantation. Ion implantation dose was varied in the range of 1-3e15 cm^{-2} to vary the surface phosphorus concentration (N_s) and see the impact of dose on gettering. Large area screen printed commercial ready cells with full Al-BSF were fabricated and analyzed in this task to support the findings of bulk lifetime and J_{oe} studies. In the case of cast quasi-mono solar cells, with more defects, the $POCl_3$ diffused emitter gave ∼0.4% higher cell efficiency (18.6%) compared to the implanted emitter (18.2%). This was consistent with higher bulk lifetime (∼200us vs ∼340us) measured in the $POCl_3$ diffused wafers compared to ion implanted samples. However, J_{oe} of ion implanted emitter was superior but it was unable to overcome the negative effect of lower bulk lifetime in the cast material. In contrast, ion implanted Cz Si solar cells showed ∼0.3% higher absolute efficiency (19.4% vs 19.1%) due to lower J_{oe} (67fA/cm^2 vs 215fA/cm^2) compared to the $POCl_3$ diffused cells. Lower J_{oe} of the implanted cells is the result of in-situ oxide surface passivation during implant anneal. The $POCl_3$ diffused emitters have only SiNx passivation while implanted emitters have SiO_2/SiNx passivation. It is important to note that in the case of Cz cells, positive effect of lower J_{oe} was able to overcompensate the negative impact of lower bulk lifetime. Device

modeling showed that this is because lifetime above 250us has no appreciable effect on the efficiency of full Al-BSF cell structure but lower J_{oe} gives higher V_{oc} and efficiency. Thus, ion implantation was found to be superior for higher quality Cz materials but $POCl_3$ diffusion gave better efficiency for lower quality cast silicon materials. Since ion implanted Cz cells gave best efficiency, we selected phosphorus ion implantation and Cz silicon wafers to achieve high efficiency in remaining tasks.

In Chapter V, we switched from baseline cells with full Al-BSF to a more advanced cell structure, called PERC (Passivated Emitter Rear Cell) which involoves dielectric passivation and local Al-BSF on the back. This concept improves back surface passivation and back reflection, which can improve cell efficiency by $\sim$1% absolute compared to the full Al-BSF baseline cells. Structure and fabrication process of the PERC cells were described in detail in this chapter. In this chapter, two modifications were introduced to the traditional screen printed contact technology in an attempt to raise the cell efficiency. First, five busbar technology was implemented instead of widely used three and four busbars on PERC solar cell by optimizing the number of gridlines. This was accomplished through grid design modeling program which minimizes the shadowing and resistive losses and calculates the efficiency as a function of the number of busbars and gridlines. Our modeling shows that five busbar technology with 90 gridlines can reduce total series resistance of the PERC cell to $\sim$0.5 ohm-cm^2 compared to 0.72 ohm-cm^2 for the three-busbar PERC cell. This raised the FF from 78.9% to 79.9%, resulting in enhanced solar cell efficiency from 20.2% to 20.5%. Secondly, fine gridline screen printing technology was developed to increase solar cell efficiency by reducing shading loss. We developed fine girdline printing by altering screen design, paste and printing parameters. Gridlines of 50um width were achieved as opposed to $\geq$65um by increasing the number of mesh wires in the screen from 360 to 650 (per inch) in conjunction with slightly thinner mesh wires (14um vs 15um). Narrower gridlines reduced the shading loss from 6.6% to 5.6% and increased

J_{sc} by 0.2mA/cm^2 and the cell efficiency by another 0.1% absolute from 20.5% to 20.6%.

In Chapter VI, we implemented a novel high throughput plasma charging method to inject negative charge in the dielectrics for field-effect surface passivation of p-type bifacial PERC solar cells and n-type bifacial PERT. In the case of n-PERT, negative charge was injected on the front SiO_2/SiNx stack on top of the boron emitter while in the p-PERC negative charge was injected in the rear SiO_2/SiNx stack on top of the p-base. Negative charge injection was performed by a novel low cost plasma charging tool and method developed by Amtech corporation. C-V measurements on the MOS structures showed that this tool can indeed inject negative charge up to $\geq$1e13cm^{-2} easily in the SiO_2/SiNx stack. The negative charge was shown to be mostly trapped in the SiNx layer and accumulated at the SiO_2/SiNx interface. Detailed analysis showed that the emitter saturation current density (J_{oe}) of SiO_2/SiNx passivated boron emitter (85ohm/sq) decreased from $\sim$80fA/cm^2 to $\sim$50fA/cm^2 after 7.9e12cm^{-2} negative charge injection. This J_{oe} value is equivalent to the J_{oe} of widely used Al_2O_3/SiNx (negative fixed charge) passivated boron emitter, suggesting that this simple and low-cost technique can be used to replace the more expensive and hazardous PECVD Al_2O_3 deposition tool in industry. Large area (239 cm^2) n-type bifacial PERT and p-type bifacial PERC cells were fabricated and injected with negative charge. It was shown that cell efficiencies increased by 1.35% and 0.23% absolute for n-PERT (from 19.00% to 20.35%) and p-PERC (from 19.95% to 20.18%) cells, respectively, after 1E13 cm^{-2} negative charge injection in SiO_2/SiNx stack. N-type PERT cells showed an increase in all the key cell parameters including V_{oc} (ΔV_{oc}, 12mV), J_{sc} (ΔJ_{sc}, 1.6mA/cm^2) and FF (ΔFF, 0.5%). Detailed characterization and modeling revealed that negative charge injection transformed the boron emitter surface in n-PERT cell from depletion mode to accumulation mode, reducing the recombination at the surface defects. This is because SRH recombination decreases rapidly when one type of

carrier concentration is much greater than the other. In case of p-type PERC cell, efficiency increased only by 0.23% absolute mainly due to increase in FF (ΔFF, 0.6%) and small increase in J_{sc} (ΔJ_{sc}, 0.1mA/cm^2). This is because C-V measurements on MOS structure showed that p-PERC back surface was inverted before negative charge injection due to large positive charge in the dielectric stack in conjunction with low boron doping in the base. Inversion layer provided excellent passivation due to much higher electron concentration than hole concentration. When negative charge injection transformed the back surface from inversion to accumulation, with much higher hole concentration, there was little change in passivation. However, parasitic shunting or leakage of minority carriers at the back contact was reduced or eliminated because back surface now primarily has majority carriers. In addition, it was found that negative charge injection also improved effective lifetime at lower injection below V_{oc}. Both these factors contributed to the observed increase in FF. This novel plasma charging method enhanced both bifacial n-type PERT and p-type PERC cell efficiencies by negative charge injection.

In Chapter VII, selective emitter technology was implemented by developing an etch-back process to replace the homogeneous phosphorus emitter in the PERC cell. Selective emitter design uses a heavily doped n^{++} region underneath the metal contact area and a much lighter diffusion in the field region (non-metal contact area), reducing both metal-induced recombination as well as field emitter recombination. In order to achieve this, a chemical etch-back process was developed, consisting of four steps: printing resist for masking heavily diffused regions, formation of porous silicon layer in between the resist by chemical etching, removal of resist masking, and removal of porous silicon by chemical etching. Using the etch-back process, large area screen printed selective emitter PERC solar cells were fabricated with 60 ohm/sq n^{++} grid region and 130 ohm/sq field region in between, replacing the standard 60 or 90 ohm/sq homogeneous emitters in PERC cells. Selective emitter cell achieved the best

efficiency of 20.49% representing an absolute efficiency increase of 0.60% over the 60 ohm/sq homogeneous emitter (19.89 %) and 0.26% increase over the 90 ohm/sq homogeneous emitter (20.23%). This demonstrates the merit of using selective emitter in PERC cells.

In Chapter VIII, a technology roadmap for PERC cells was developed by extensive Sentaurus 2D device modeling to outline how to raise its efficiency to ∼23% by practical and manufacturable technology developments. Key material and device parameters as well as cell design were varied to project the best way to raise PERC cell efficiency to ∼23%. Modeling showed that the baseline 20.6% PERC solar cell with homogeneous emitter can get to 23% efficiency by nine technology enhancements including 1) floating busbar: which reduces J_{oe} to give 0.1% efficiency increase, 2) charge injection: which removes of shunt mechanisms by forming accumulation layer and give additional 0.1% efficiency increase, 3) optimized selective emitter: which reduces J_{oe} further and gives 0.3% increase, 4) screen printing of 30 um wide fingers: which provides 0.4% efficiency increase, 5) screen printing of 0.5mm wide busbars: which gives 0.2% efficiency increase, 6) formation of void free and ∼7um thicker local Al-BSF instead of 0-2um: which gives additional 0.1% efficiency increase, 7) achieving higher bulk lifetime (2ms): which gives 0.6% efficiency increase, 8) self-aligned selective emitter (13/130 ohm/sq) with ∼ 30um wide n^{++} region (formed by laser doping and plating): which provides 0.6% efficiency increase and 9) implementation of 15 wire busbar technology which reduces series resistance and gives 0.2% efficiency increase. All these nine technologies are discussed in more detail in Chapter 8 to raise the PERC cell efficiency to 23%.

Light-induced degradation or LID is a well known phenomenon and problem which can reduce PERC cell efficiency by ∼1% in absolute due to the formation of B-O (boron-oxygen) complexes under light exposure. Therefore, in Chapter IX and X, an attempt was made to substantially reduce or eliminate LID in PERC cells. In

Chapter IX, indium (In) doped p-type Cz (Czochralski) silicon wafers were used to replace widely used boron (B) doped Cz Si wafers. Performance potential and LID response of commercial size In-doped Si solar cells were investigated for the first time. Prior to LID, In- and B-doped baseline cells with full Al-BSF gave nearly identical efficiencies (19.2%). However, In-doped PERC cells gave ∼0.3% lower efficiency (20.3 %) compared to the B-doped cells (20.6 %) due to lower bulk lifetime and higher BSRV. This may be attributed to inactive or unionized indium atoms which can form recombination centers. After the LID at ∼0.8 sun illumination for 48 hours at 37°C, low and high resistivity B-doped cells showed 0.9% and 0.4% efficiency degradation, respectively. In contrast, In-doped cells showed no loss in performance after the illumination. Thus, in spite of slightly lower starting efficiency, In-doped PERC cells showed no LID and surpassed the B-doped PERC cell efficiency by 0.3 - 0.5% after LID. This shows the promise of In-doped cells for higher stabilized efficiency, which makes them an attractive candidate for PV applications.

In Chapter X, a B-O deactivation treatment (also called regeneration) was developed and studied using a combination of light and heat to deactivate or passivate B-O complexes. Three regeneration treatments were investigated (200°C/3 suns/30s, 75°C/1 sun/48 hours and 130°C/2 suns/1.5 hours) before and after the LID test in an attempt to eliminate LID either by preventing the formation of active B-O complexes or by passivating them by hydrogen during the regeneration cycle. It has been suggested that hydrogen in bulk Si is tied to impurities like B but under light and heat exposure it dissociates and changes its state from H+ to H0 and migrates to B-O complexes to passivate them. However, at higher temperature some of the passivated B-O-H complexes can revert back to degraded state (B-O) or annealed state (dissociated B and O). Pre-LID efficiencies of PERC and baseline full Al-BSF cells were ∼20.4% and 19.2%, respectively. After LID, efficiencies of PERC and full Al-BSF cells dropped to 19.5% and 18.5%, respectively, due to the formation of B-O

complexes. PERC cells showed a much greater loss in absolute cell efficiency (0.9% vs 0.6%) because the degradation in bulk lifetime also eroded the benefit of superior BSRV in PERC cells. The 200°C/3 suns/30s regeneration treatment prior to LID reduced the efficiency degradation from 0.9% to 0.1% in PERC cells and from 0.6% to 0.3% in full Al-BSF cells. The low temperature (75°C/1 sun/48 hours) regeneration reduced the efficiency loss to 0.1-0.2% and 0.3% in PERC and full Al-BSF cells, respectively, again indicating that regeneration is more effective in PERC cells. This is because PERC cell had more hydrogen in the bulk Si due to double side SiNx and higher injection level or fermi level split due to higher V_{oc}. This helped in the creation of more neutral hydrogen (H+ -> H0) which migrates to passivate the B-O complexes. Notice that both high and low temperature regeneration conditions were unable to reach 100% stabilization, likely because at high temperature (200°C) some of the passivated B-O complexes reverted back to annealed or destabilized states during regeneration and at low temperature (75°C) the regeneration was so slow that even after 48 hours of regeneration some B-O complexes remained active. Thus, an intermediate temperature regeneration condition at 130°C at 2 suns for 1.5 hours was attempted. This condition finally achieved full passivation or stabilization because regeneration was fast enough to passivate all the B-O complexes without triggering the destabilization or annealed paths. Therefore, optimized regeneration process can lead to full stabilization in PERC as well as full Al-BSF cells.

In summary, large area screen-printed p-type PERC solar cells (239 cm^2) were achieved in this research with an efficiency of ∼20.6% through a combination of device modeling, several technology developments and process integrations. In addition, a technology roadmap was developed to achieve 23% efficient PERC solar cells by Sentaurus 2D device modeling. Finally, a substantial reduction or elimination of light induced degradation was achieved by fabricating In-doped PERC solar cells and by an optimized regeneration treatment of B-doped PERC cells under light and heat.

This research resulted in 11 publications in high-impact journals and international refereed conference proceedings. The research in this thesis was supported by incubator project with Amtech corporation and FPACE I project, both funded by U.S. Department of Energy, and new material test project funded by SunEdison corporation.

CHAPTER I

INTRODUCTION

1.1 Statement of the Problem

Rapid increase in the world′s energy consumption (Figure 1) is accompanied by a large amount of CO_2 emission (Figure 2) because ∼80% of the energy today is derived from fossil fuels such as oil, coal and natural gases [1]. Unfortunately, CO_2 accounts for ∼65% of the emitted greenhouse gases that contribute to global warming or increase in the Earth′s temperature [2]. Therefore, Kyoto Protocol was adopted in 1997 to retard global warming by reducing greenhouse gas concentration. Concerns about the harmful effects also led the development of more alternative energy sources. The International Energy Agency (IEA) reported that the share of total world electricity generation by renewable energy sources need to increase from 19% currently to 57% by 2050 to limit the average global temperature increase to less than 2°C [3].

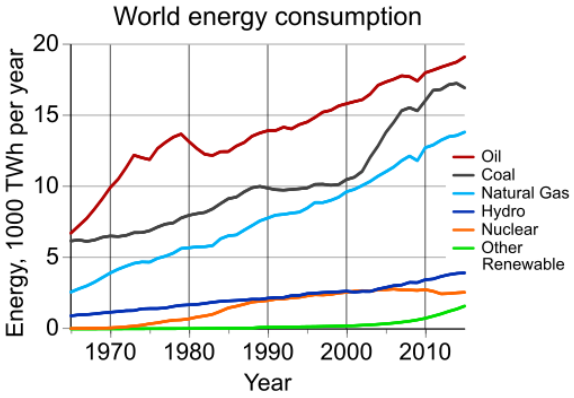

Figure 1: Global energy consumption (1965-2015) [4].

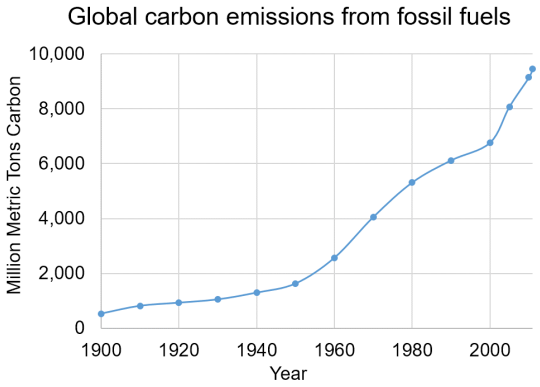

Figure 2: Global carbon emissions from fossil fuels (1900-2011) [5].

Among the various renewable energy options available today, photovoltaics is most attractive because solar energy, which is the fuel for solar cells, is essentially unlimited, clean and free, and solar cells can directly convert sunlight into electricity with no undesirable impact on the environment. In addition, amount of solar energy incident on the Earth in one hour (1.20×10^{14}kwh) is more than the annual world energy consumption (1.14×10^{14}kwh) [6]. Moreover, photovoltaics is noise-free, safe and compatible with on-site installation. The only challenge is cost, which has been declining rapidly. Figure 3 shows the rapid increase (>35% per year) in installed PV capacity in the world. Figure 4 shows the learning curve of PV which indicates every time cumulative installed PV doubles in the world, PV module price drops by 21.5%. Since 1976, installed PV has grown ~600,000 times from 0.4MW to 227GW in 2015 and module prices have decreased from \$100/W to \$0.6/W or more than 100 times.

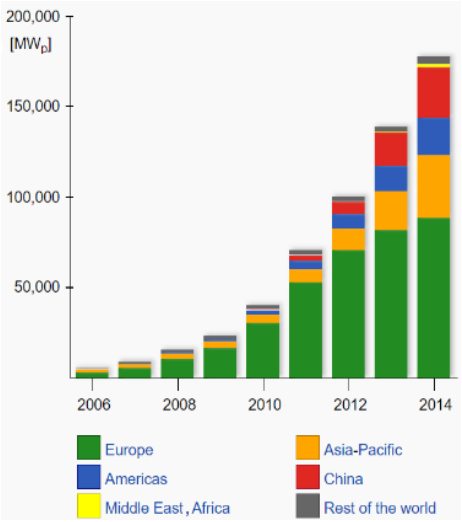

Figure 3: Worldwide cumulative capacity in megawatts [7].

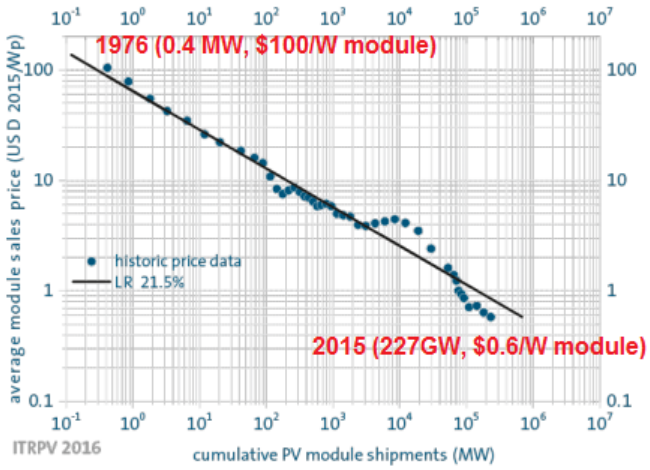

Figure 4: Learning curve for module price (USD/Watt) as a function of cumulative PV module shipments (Megawatts,MW) [8].

However, the cost of PV is still little more expensive than that of fossil fuels in most parts of the world. PV industry can produce levelized cost of electricity (LCOE) at 7-18 cents/kwh today for residential, commercial and utility scale applications (Figure 5) compared to the 2020 target value of ~6 cents/kwh for utility scale applications

in the US, which is often defined as grid parity [9–11]. Figure 5 also shows that the Department of Energy has recently set a new target of 3 cents/kwh for LCOE which is half of the grid parity today.

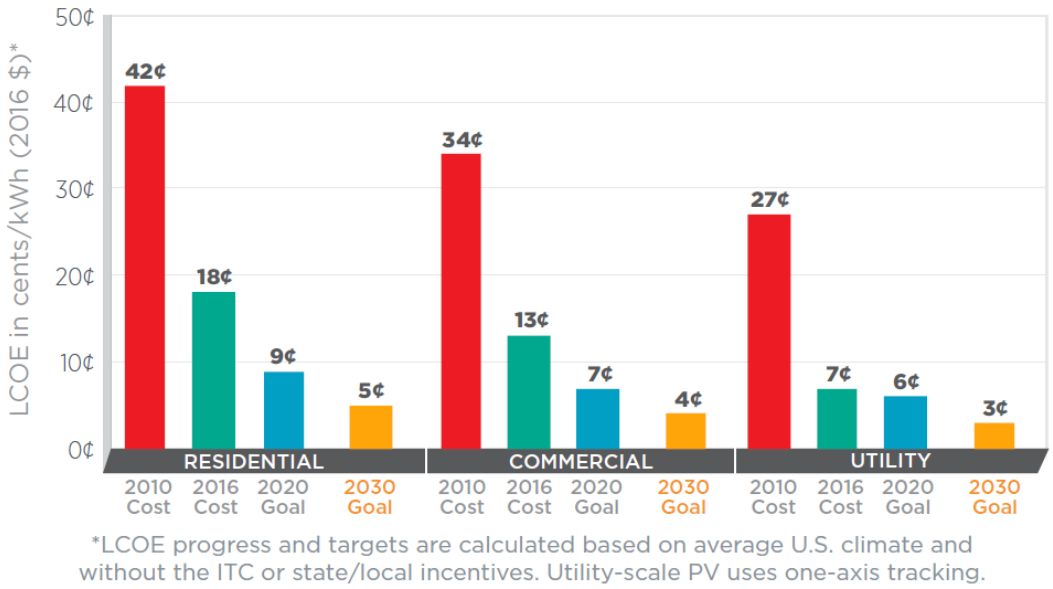

Figure 5: LCOE values and SunShot goals for the residential, commercial and utility-scale sectors.

This can be accomplished partly by increasing solar cell efficiency while maintaining low-cost. Moreover, most of the current PV industry fabricates p-type boron doped silicon solar cells, which show 0.5-1% degradation [12] in absolute efficiency after a few days of sunlight exposure. Reduction or elimination of this light-induced degradation can also reduce the cost of PV.

Therefore, the goal of this thesis is to achieve low-cost higher cell efficiency commercial ready screen-printed silicon solar cells with little or no light-induced degradation by a combination of fundamental understanding of loss mechanisms, technology innovations, and formation of commercial size solar cells.

1.2 Specific Research Objectives

1.2.1 Improving the efficiency of p-type PERC silicon solar cells

Higher solar cell efficiency is the most effective way to reduce the levelized cost of electricity (LCOE) from PV because it reduces module cost as well as the installation and balance of system cost for a given power output. That is why PV industry and many research groups are currently focusing on achieving higher efficiency solar cells without appreciably increasing the cell processing cost.

Crystalline silicon (Si) accounts for more than 90% of the solar cells produced today and about 95% of all the Si cells are fabricated on p-type Si wafers [13]. This is because of the well-established technology and equipment base for p-type cell fabrication, lower wafer price, and lower cell processing cost compared to n-type cells. Figure 6 shows the two most popular p-type solar cell structures that are currently being manufactured.

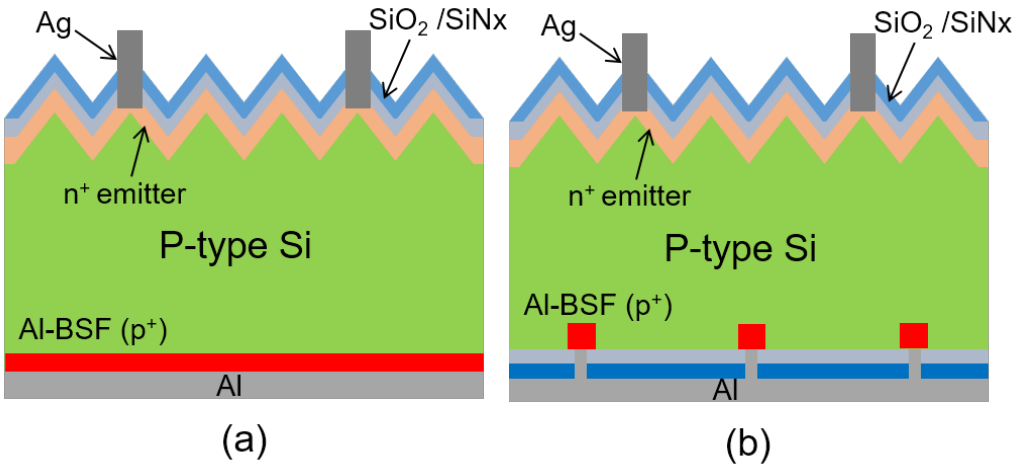

Figure 6: Structures of (a) baseline full Al-BSF and (b) advanced PERC solar cells.

Baseline cell structure (Figure 6(a)) incorporates full aluminum back surface field (BSF) and the advanced passivated emitter rear cell (PERC) structure (Figure 6(b)) involves local Al-BSF through a passivating back dielectric. Full Al-BSF or baseline cell structure is simpler and slightly cheaper to fabricate but it gives about ∼1%

lower efficiency than the advanced PERC cells. p-type PERC has recently become the most desirable cell structure to attain high efficiency at low cost because it only adds couple of simple steps to the standard baseline cell fabrication sequence but it gives much higher efficiency. Many companies have already started producing PERC cells with PERC production capacity approaching 5 GW in 2015 [14], while many others are planning to switch from baseline to PERC technology. Cost benefit of PERC technology is dictated by its efficiency potential, therefore, a key objective of this thesis is to achieve higher efficiency PERC cells by technology innovations and develop a technology roadmap by device modeling to achieve even higher efficiency. The second major objective is to reduce or eliminate the widely observed light-induced degradation in PERC cells. Above goals will be accomplished by following tasks in this research.

1.2.1.1 Task 1: Comparison of $POCl_3$ source tube diffusion and phosphorus ion implantation technologies for emitter formation of p-type solar cells

There are multiple options for producing the n-type emitter on p-base solar cells. In this task, liquid $POCl_3$ source diffusion and phosphorus ion-implantation will be investigated to form high quality emitters to achieve higher cell efficiency. Cell efficiency is a strong function of the bulk lifetime in p-base and emitter saturation current density (J_{oe}). Higher bulk lifetime and lower J_{oe} are good for cell efficiency. $POCl_3$ diffusion may have an advantage in terms of bulk lifetime because double side diffusion can getter or extract defects and impurities from both sides of the wafer. However, ion-implantation allows the growth of a thermal oxide on the emitter at no cost during the implantation anneal, which may provide better emitter surface passivation or lower J_{oe}. Because of this tradeoff, it is not clear which technology can give higher cell efficiency and it may be a function of starting quality of p-type material. Therefore, the objective of this task is to quantify the bulk lifetime enhancement and emitter saturation current density reduction for these two promising technologies to

provide quidlines for achieving high efficiency. Currently, ∼60% of p-type cells are made on low-cost multicrystalline silicon wafers, which are cheaper but have more defects, and ∼30% are made on higher quality single crystalline Czochralski (Cz) grown silicon [13]. Multi-crystalline material may benefit more from gettering than Cz. Therefore, in this study both Cz and cast quasi-mono silicon wafers will be used to evaluate the merit of $POCl_3$ diffusion and ion-implantation in order to quantitatively establish which technology is more suitable for high efficiency on the two most dominant p-type Si materials used for PV.

1.2.1.2 Task 2: Analytical modeling, design and development of multi-busbar and fine gridline printing

In this task, two advanced features will be introduced into the traditional screen printed contact technology to raise the cell efficiency. First, 5 busbars will be used to reduce series resistance instead of widely used 3 and 4 busbars. Secondly, fine gridline printing will be developed to reduce gridline width from ∼65um to ≤50um. Besides technology development, grid modeling will be used to design the grid patterns to optimize the trade-off between resistive and shadow losses and predict the efficiency improvement from these two contact technology enhancements. Technology enhancements will be applied individually as well as in combination to PERC solar cells to validate the predicted solar cell efficiency improvement.

1.2.1.3 Task 3: Field-effect passivation by charge injection into SiNx using a novel low-cost plasma charging method

Field effect passivation by negative charge is important for back surface of p-type PERC cell and front boron emitter surface of n-type PERT cell. Negative charge can form majority carrier rich accumulation layer, which reduces the minority carrier recombination and shunting associated with depletion and inversion layers. Currently, Al_2O_3 passivation is widely used for these cells due to its large negative fixed charge. However, Al_2O_3 tool has high operation cost and safety related issues due to the

use of TMA precursor. In this task, a novel plasma charging tool is used to inject negative charge into the SiNx/SiO_2 passivation stack and its impact is compared with Al_2O_3 passivation. Large area bifacial n-type PERT and p-type PERC cells will be fabricated, characterized and analyzed before and after negative charge injection.

1.2.1.4 Task 4: Implementation of selective emitter PERC solar cells by etch-back process

Reduced recombination is the key to high efficiency. Selective emitter uses a heavily doped n^{++} region underneath the metal contact area and a much lighter diffusion in the field region (non-metal contact area). This reduces both metal-induced recombination as well as field emitter recombination. Therefore, in this task, emitter bulk and surface recombinations will be minimized by replacing homogeneous emitter by selective emitter. This should result in lower emitter saturation density (J_{oe}) and higher V_{oc} and efficiency.

1.2.1.5 Task 5: Sentaurus 2D device simulations to develop a roadmap for high efficiency PERC solar cells

In this task, an efficiency roadmap will be developed by Sentaurus 2D modeling to raise the efficiency of a p-type PERC to ∼23% by practical and manufacturable technology developments. Key material property and device parameters as well as cell design will be varied to outline the best way to raise a PERC cell efficiency to ∼23%. Extensive 2D modeling will be performed using advanced Sentaurus device modeling program to establish its efficiency potential and a technology roadmap. Impact of selective emitter, bulk lifetime, and contact design will be assessed quantitatively by modeling to establish target values for these parameters.

1.2.2 Development of stabilized p-type silicon solar cells

Silicon PV industry currently produces more than 95% Si cells on p-type boron doped silicon [13]. However, these cells are known to suffer from light-induced degradation (LID) in cell efficiency due to the formation of boron-oxygen (B-O) complexes, which can degrade bulk lifetime and absolute cell efficiency by 0.5%-1% [15]. This degradation increases in higher efficiency PERC cells [12]. Since B-O complexes are the source of LID, it can be reduced or eliminated by choosing n-type material, reducing oxygen and boron concentrations in the wafer, deactivating the B-O complexes, or replacing boron (B) dopant with gallium (Ga) or indium (In). Therefore, a second major objective of this thesis is to achieve higher stabilized PERC solar cell efficiency through following tasks.

1.2.2.1 Task 6: Fabrication and analysis of In-doped PERC solar cells

In this task, In-doped p-type Cz Si wafers will be used to replace B-doped wafers. Performance potential and LID response of commercial size In-doped Si solar cells will be investigated to eliminate LID in p-type PERC cells. Large-area screen-printed In-doped PERC solar cells will be fabricated and characterized. Their LID performance will be compared to B-doped PERC solar cells to quantify the absolute efficiency as well as the difference in efficiency before and after LID.

1.2.2.2 Task 7: Understanding and development of regeneration treatment to eliminate LID in B-doped cells

B-O deactivation treatment (also called regeneration treatment) has become an active of investigation to reduce LID and achieve high stabilized efficiency. Even though LID happens under light, it has been shown recently that appropriate light exposure at elevated temperature can actually recover LID or prevent it from happening. This is a promising approach because it can be applied at the end of cell processing, and it maintains higher bulk lifetime by eliminating the LID phenomena

in high efficiency PERC cells. In this task, regeneration technology will be developed and studied using a combination of light and heat to deactivate or passivate B-O complexes. Attempt will be made to understand the mechanism and optimize the process to minimize the LID in B-doped Cz samples.

CHAPTER II

PHYSICS AND OPERATION OF SILICON SOLAR CELLS

2.1 Basic Operation of a Solar Cell

Solar cell is a large p-n (positive-negative) junction device (Figure 7) which separates light generated electrons and holes by band bending effect. Separated electrons and holes flow to the load through metal contacts. Fundamental physics of each step is discussed in the following subsections.

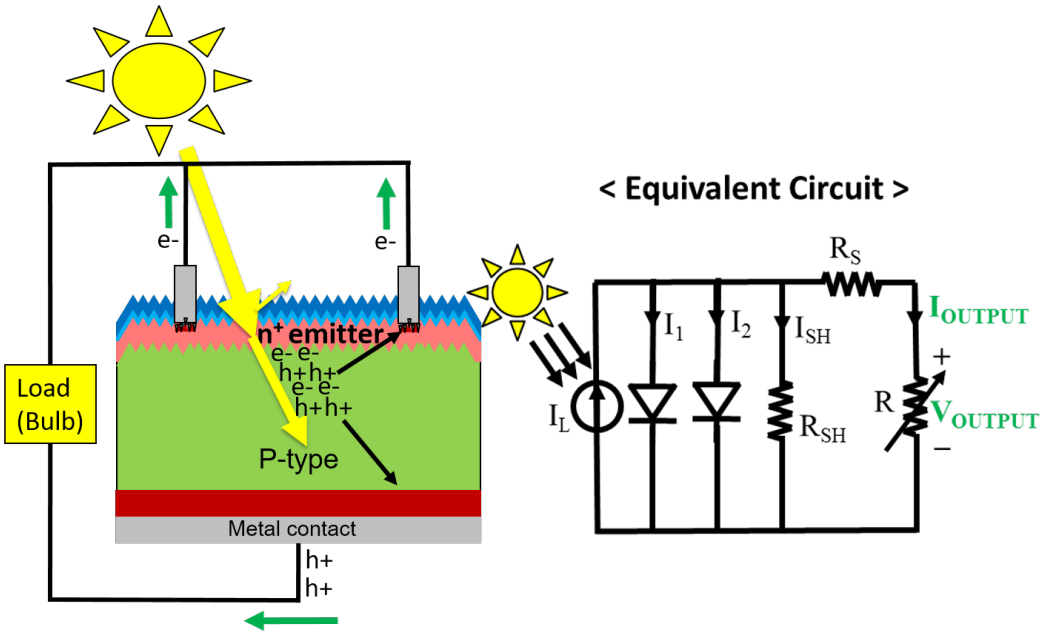

Figure 7: Schematic of basic operation of a silicon solar cell and its equivalent circuit.

2.1.1 Generation of electrons and holes in a silicon solar cell by sunlight.

Sunlight has a wide range of wavelengths (280nm $\sim$ 4000nm) as shown in Figure 8 with different spectral irradiance for each wavelength.

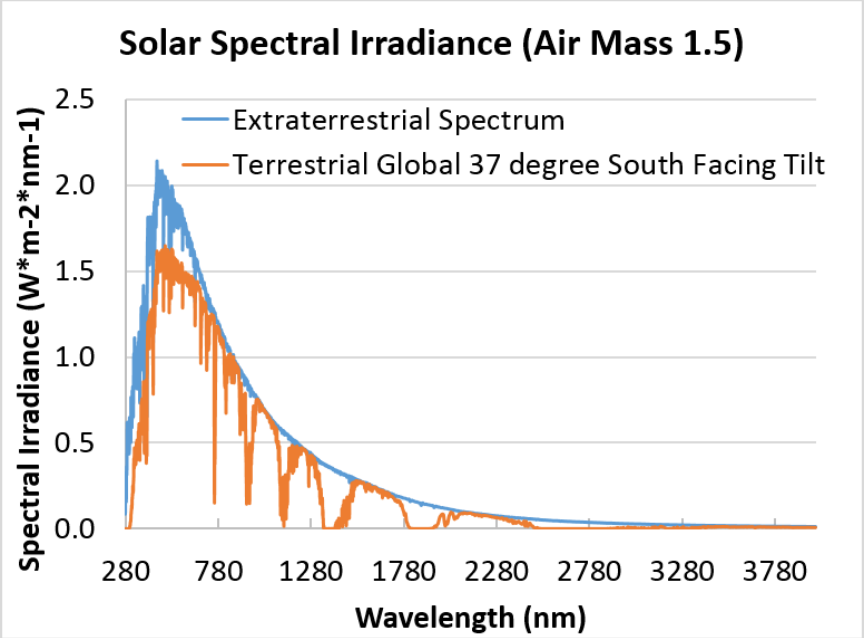

Figure 8: Solar spectral irradiance for extraterrestrial and terrestrial spectrum [16].

Figure 8 shows that sunlight arriving above the earth atmosphere (space) has higher spectral irradiance than sunlight striking the Earth's surface (terrestrial spectrum). This is because of the Rayleigh scattering by dust particles and small molecules and absorption by air molecules (O_2, H_2O and CO_2). Also, only the wavelength with energy greater than the bandgap of semiconductor can generate electron-hole pairs, therefore, a very significant amount of solar energy gets wasted ($\sim$23% for silicon).

2.1.2 Separation of electrons and holes by p-n junction.

As shown in Figure 9, when a p-n junction is formed by bringing the phosphorus doped n-type and boron doped p-type silicon together, electrons in n-doped silicon diffuse into p-doped silicon and vice versa.

This diffusion flow leaves positively charged donor ions in n-doped silicon side and negatively charged acceptor ions in p-doped silicon side, creating an electric field in an area called depletion or space charge region. Once the electric field force is equal to the diffusion flow force, the p-n junction attains an equilibrium state, creating

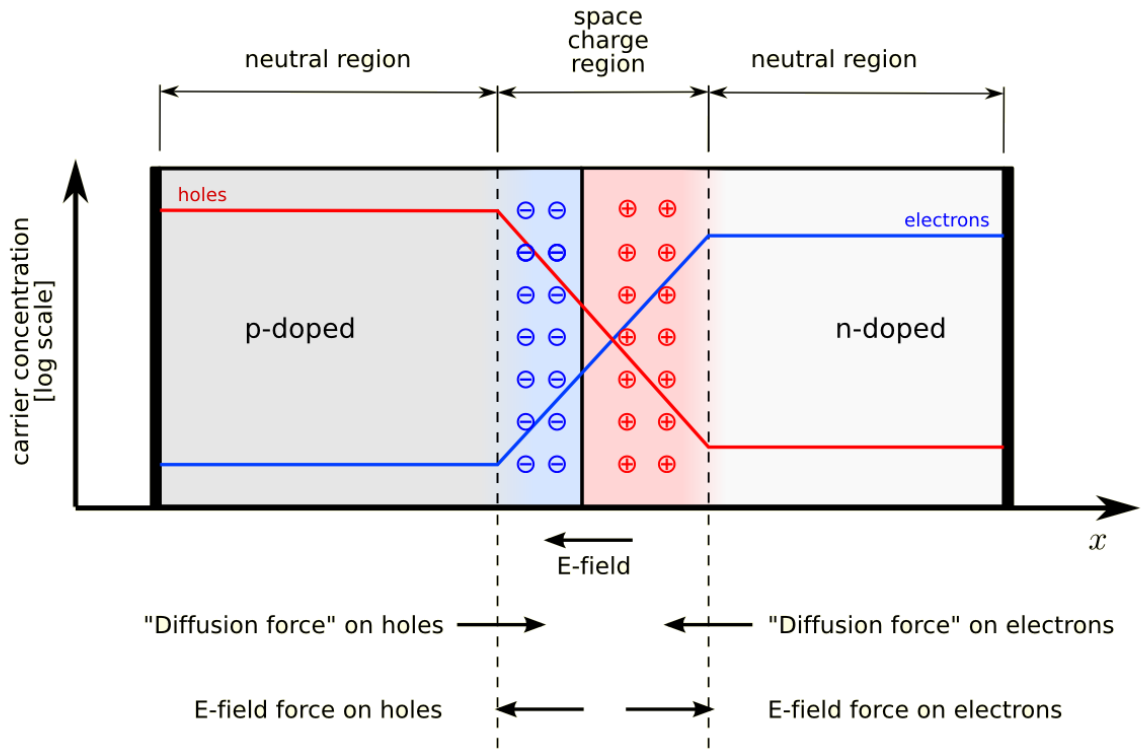

Figure 9: A p-n junction in thermal equilibrium with zero-bias voltage applied [17].

band bending due to its different Fermi levels in p-type and n-type regions as shown in Figure 10.

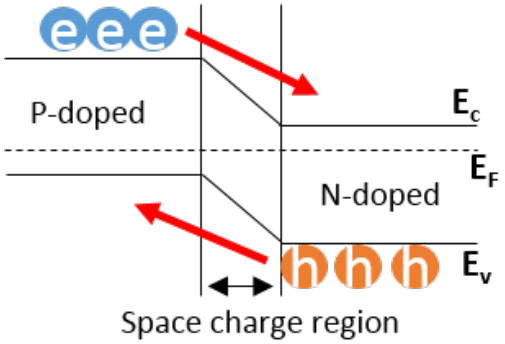

Figure 10: Band diagram of a p-n junction.

The band bending (Figure 10) seperates the light generated electron and hole pairs by transporting electrons in n-doped region and holes to p-doped region, resulting in charge separation or photovoltage also referred to as photovoltaic effect.

2.1.3 Flow of electrons and holes to external loads via metal contacts in p- and n-doped regions.

After light-generated electron and hole pairs are separated, electrons and holes are transferred from silicon to metal ohmic contact and moved to the external loads. Heavy doping is important underneath metal contact to reduce significant electron-hole recombination losses. This is because metal contact region has a high density of states around the Fermi level, resulting in a high recombination velocity at the silicon-metal contact (Figure 11). Maximum recombination velocity at the metal-Si interface is limited by electron or hole thermal velocity ($v_{e/h,th}$) given by,

$$v_{e/h,th} = \sqrt{\frac{3kT}{m_{e/h}}} \quad (\sim 10^7 cm/s \quad at \quad 300k), \tag{1}$$

where k is boltzmann constant, T is temperature and $m_{e/h}$ is electron or hole rest mass.

Heavy doping can reduce the metal-induced recombination by introducing band bending which favors one type of carriers at metal-Si interface and thereby reduces electron-hole recombination.

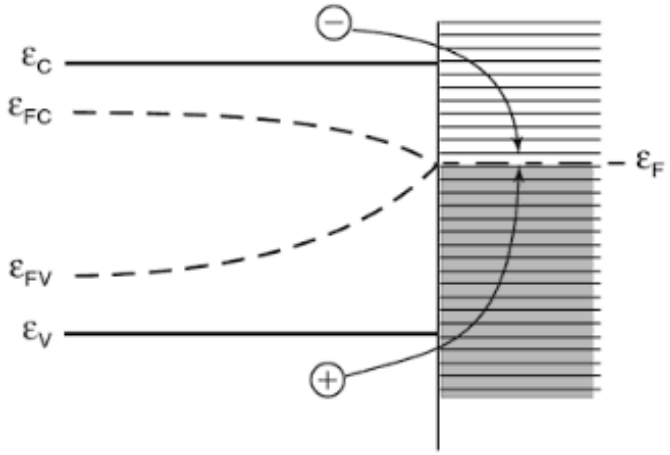

Figure 11: The continuous distribution of a high density of states around the Fermi energy in a metal results in a high interface recombination velocity at a semiconductor-metal contact [18].

2.2 Key Solar Cell Parameters

Figure 12 shows the typical I-V and P-V curves. Conversion efficiency of a solar cell is defined as the following Equation,

$$Efficiency\,(\eta) = \frac{P_{\text{out}}}{P_{\text{in}}} = \frac{V_{\text{mp}} * I_{\text{mp}}}{P_{\text{in}}} = \frac{V_{\text{oc}} * I_{\text{sc}} * FF}{P_{\text{in}}}, \quad FF = \frac{V_{\text{mp}} * I_{\text{mp}}}{V_{\text{oc}} * I_{\text{sc}}} \qquad (2)$$

, where P_{out} is power output of a solar cell, P_{in} is power input from incident sunlight ($100mW/cm^2$ for standard test conditions (STC)), V_{mp} is voltage at maximal power point, I_{mp} is electric current at maximal power point, V_{oc} is open-circuit voltage, I_{sc} is short-circuit current and FF is fill factor.

I-V characteristic curve of a solar cell is shown in Figure 12.

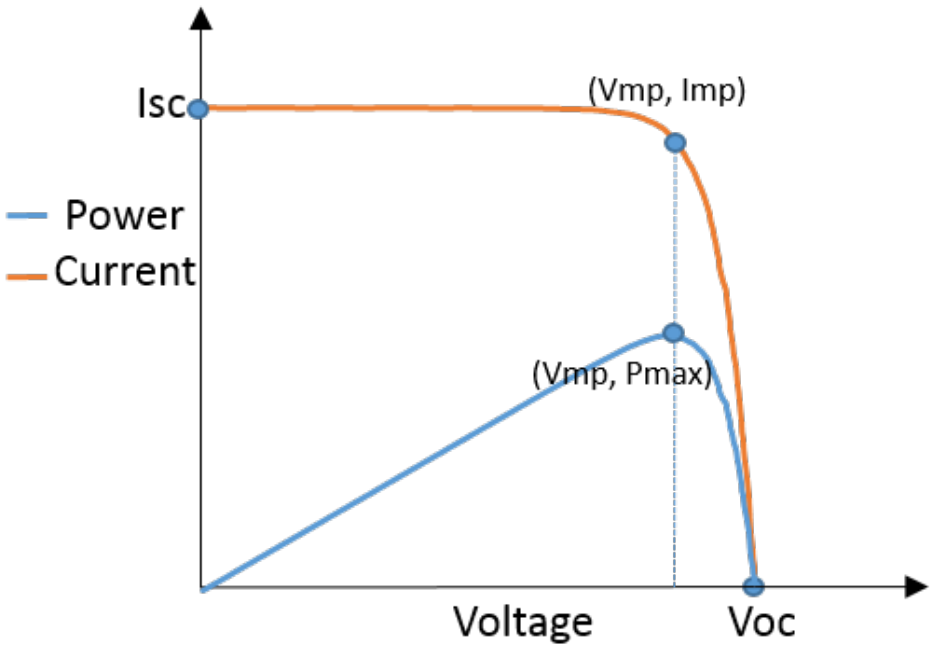

Figure 12: I-V characteristic curve of a solar cell.

Important parameters characterizing a solar cell are V_{oc}, I_{sc}, and FF. Increase in any of these three parameters leads to higher efficiency solar cells.

2.3 Loss Mechanisms in Silicon Solar Cells

The theoretical limit of a single junction silicon solar cell efficiency is 29.3% at one-sun [19]. Recently, research labs such as Panasonic and Sunpower reported 25∼25.6% efficiencies at one-sun [20,21]. The gap between theoretical limit and the present solar cell efficiency is due to the following electrical, optical and resistive losses.

1) Optical losses: reflectance, metal shading, and incomplete absorption (main impact on J_{sc}).

2) Electron and hole recombination due to Radiative, Auger, and Shockley Read Hall mechanisms in the bulk, surfaces and diffused regions (main impact on V_{oc}).

3) Parasitic resistance losses: series and shunt resistances (main impact on FF).

These losses are discussed in more detail in the following subsections.

2.3.1 Optical loss

2.3.1.1 Reflection of silicon surface

Figure 13 shows that bare silicon material reflects more than 30% of sunlight for wavelengths ≤1000nm.

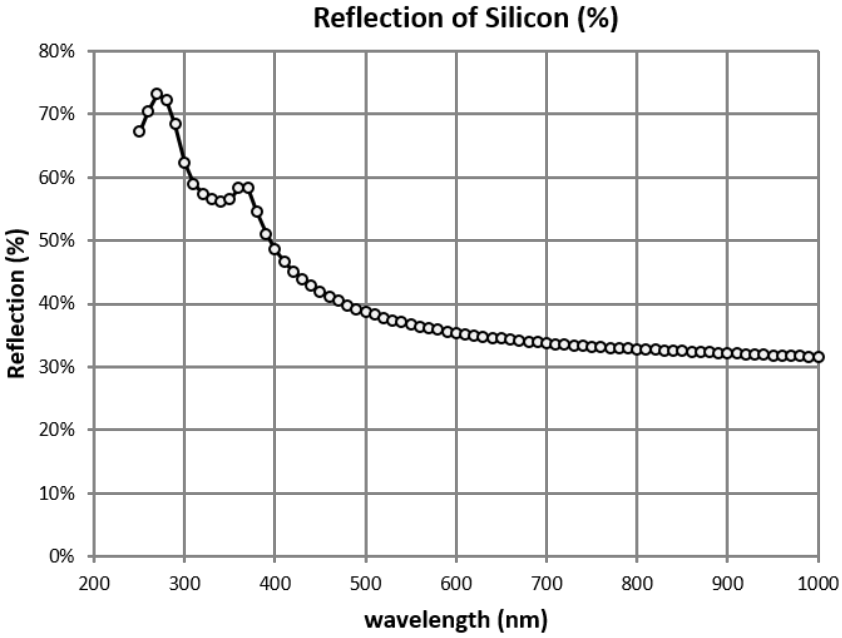

Figure 13: Reflection of silicon as a function of wavelength. [22]

In order to reduce surface reflectance, solar cell industry applies anti-reflection coating and implements texturing. Anti-reflection (AR) coating is formed by depositing additional layer(s) on top of silicon surface. If the thickness and index of the AR coating are selected such that the light reflected from the air/AR coating interface undergoes destructive interference with the light reflected from the Si/AR coating interface, then reflectance can be minimized and most of the light will go into Si (Figure 14).

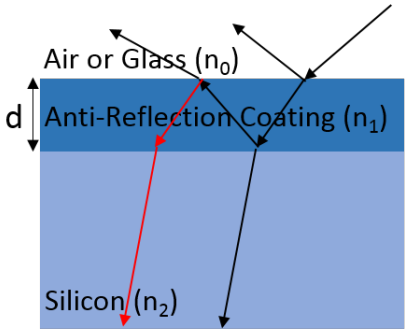

Figure 14: Schematic of anti-reflection coating concept (n_0, n_1 and n_2 are refractive indexes of air or glass, anti-reflection coating and silicon, respectively.

Specific refractive index and thickness combinations of the anti-reflection coating are necessary to achieve the lowest reflectance as indicated by the following Fresnel equation,

$$R = \frac{{r_1}^2 + {r_2}^2 + 2r_1 r_2 cos\theta}{1 + {r_1}^2 {r_2}^2 + 2r_1 r_2 cos\theta}, \theta = \frac{2\pi n_1 d_1}{\lambda}, r_1 = \frac{n_0 - n_1}{n_0 + n_1}, r_2 = \frac{n_1 - n_2}{n_1 + n_2}, \quad (3)$$

where n is the refractive index and d is anti-reflection coating thickness [23].

The minimum reflection R_{min} for a given λ is derived from Equation (3) when $n_1 d_1 = \lambda/4$:

$$R_{\min} = \frac{(n_0 n_0 - {n_1}^2)^2}{(n_0 n_0 + {n_1}^2)^2}. \quad (4)$$

Notice that R_{min} at that λ is zero when ${n_1}^2 = n_0 * n_2$. Also, thickness (d) of anti-reflection coating is designed to produce minimum reflection at 600 nm to minimize the average weighted reflectance of usable sunlight, even though the refractive index

of dielctric coating and reflectance of silicon surface have a wide range of values for sunlight spectrum from 250nm to 1200nm. This single layer anti-reflection coating method can reduce the average weighted reflectance from 30% for bare silicon to 10%. Multi-layers of anti-reflection coating can further reduce reflection but technique is more complex and expensive [24].

Second method to reduce reflectance is by texturing the silicon surface as shown in Figure 15. Texturing (100) surface results in pyramid like patterns which allows double bounce for the light beam before it can escape, reducing the reflectance from 30% to ∼9%. Dilute KOH (potassium hydroxide) solutions are commonly used for texturing (100) silicon surface. Using the combination of texturing and anti-reflection coating, reflectance of sunlight can be reduced to below 4% [23].

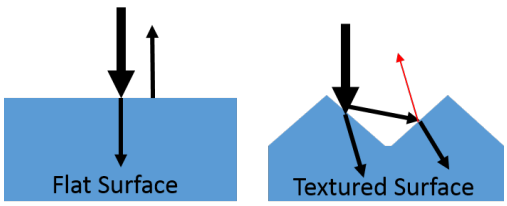

Figure 15: Schematic design of reflectances for flat surface and textured surface. [25]

2.3.1.2 Front metal shading loss

Another optical loss is from front metal shading. A silicon solar cell needs metal contacts to transport electrons and holes to the load. Figure 16 is a picture of typical three busbar (thick vertical lines)/ 89 gridlines (thin horizontal lines) screen printed front metal contact used for silicon solar cells. Since metal lines block ∼6% of the total area or incident sunlight, only ∼94% of total area is available for transmission of light.

This loss can be reduced by decreasing the number of lines and the width of the lines. This, however, results in increased series resistance and increases power loss because carriers have to travel longer distance before they can be collected by metal contact. Therefore, optimization of grid design is necessary to increase solar cell

Figure 16: Picture of regular 3 busbar front contact silicon solar cell.
efficiency.

2.3.1.3 Incomplete sunlight absorption

Silicon material limits generation of electron-hole pairs for certain part of the spectrum of sunlight because of its band gap 1.12eV (≤1100nm). Wavelengths with energy below 1.12eV are not absorbed which limits available energy for a silicon solar cell to 882 W/m^2 out of 1000 W/m^2 (AM1.5). Recent study by Green and Keevers [26,27] show that intrinsic silicon at 300K can absorb sunlight spectrum upto 1450nm (≥ 0.75eV), since silicon solar cell can also absorb sub-bandgap (≤1.12eV) wavelength (≥1100nm) due to impurity photovoltaic effect and band-gap narrowing (≤ 10%). Thickness of silicon wafer (generally ≤ 210 um), also, limits the absorption of light (Figure 17).

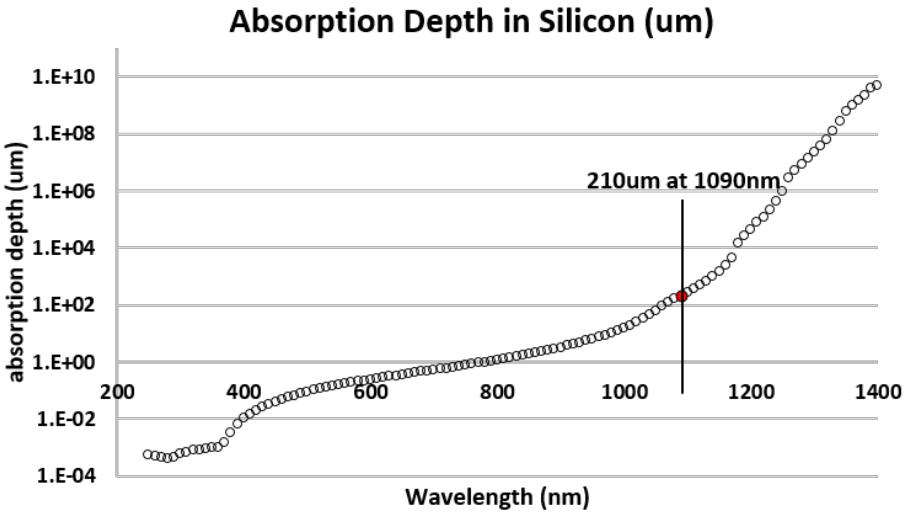

Figure 17: Absorption depth in silicon as a function of wavelength at 300k. [22]

This loss can be reduced by light trapping which increases the path length before light can escape. Combination of a good back-side reflector and front texturing can accomplish that as shown in Figure 18(b). Textured front surface and reflector result in increased optical path length as shown in Figure 18(c).

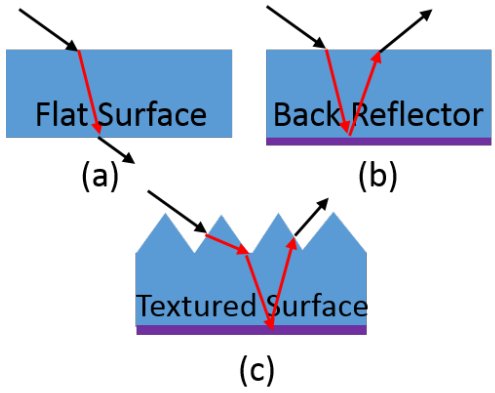

Figure 18: Light trapping methods: (a) no light trapping (b) back side reflector (c) textured surface with back side reflector.

These optical losses mainly affect on J_{sc} of solar cell as shown by the following Equation,

$$J_{\mathrm{sc}} = \int_{Eg}^{\infty} q * N_{\mathrm{ph}}(\lambda) * [1 - R(\lambda)] * IQE(\lambda) d\lambda \tag{5}$$

where Eg is band-gap energy of silicon, N_{ph} is light generated the number of photon, $R(\lambda)$ is a reflectance of solar cell and $IQE(\lambda)$ is internal quantum efficiency of solar cell.

2.3.2 Electron and hole recombination losses

Generated electrons and holes in the silicon wafers experience three well-known electron and hole recombination loss mechanisms: Radiative, Auger and Shockley Read Hall. To quantify recombination losses within the wafer, the minority carrier lifetime, τ, is used. This lifetime is the average amount of time that generated electrons survive before recombining as described by the following Eqaution,

$$\tau = \frac{\Delta n}{U}, \tag{6}$$

where τ is lifetime (s), U is volume recombination rate (cm^{-3}/s) and Δn is generated electron concentration (cm^{-3}), respectively.

2.3.2.1 Radiative recombination

Radiative recombination (reverse of photon absorption) happens when the generated electrons in conduction band (Ec) and holes in valence band (Ev) recombine directly from Ec to Ev. This recombination generates a photon energy which is equal to silicon energy band gap. This recombination rate in indirect band-gap materials such as silicon is low since in indirect band-gap materials minimum energy of conduction band and maximum energy of valence band do not line up so phonon is required for momentum change to facilitate the absorption as shown in Figure 19. On the other hand, this recombination is dominant in direct band gap materials such as GaAs.

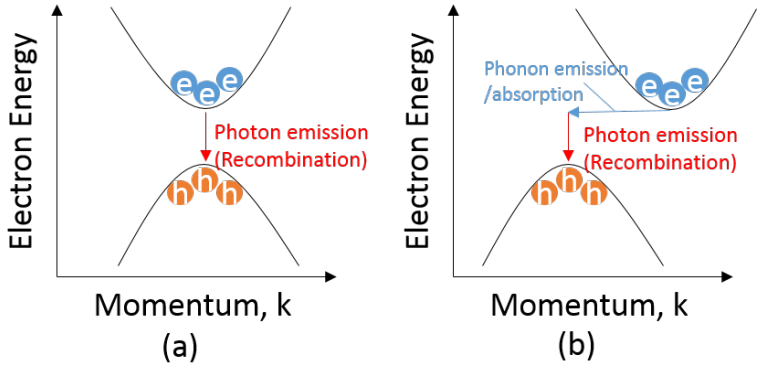

Figure 19: Radiative recombination in semiconductors: (a) direct band gap (b) indirect band gap.

The total radiative recombination rate (R_R, cm^{-3}/sec) is proportional to the product of the concentration of occupied states (electrons, n) in the conduction band and that of unoccupied states in the valence band (holes, p) as shown by Equation,

$$R_R = B * n * p, \tag{7}$$

where B is a constant for a given semiconductor material (ex. $B_{silicon}$=1.8*10^{-15}cm^3/sec).

Net recombination rate (U_R, cm^{-3}/sec) including generation rate (G, cm^{-3}/sec) is also described by Equation,

$$U_R = R_R - G = B(np - {n_i}^2). \tag{8}$$

2.3.2.2 Auger recombination

Auger recombination (reverse of impact ionization) is a phenomenon that generated electrons and holes in Ec and Ev recombine and transfer its energy to another majority carrier instead of emitting light (photon energy). These excited majority carriers return to the band edge by releasing thermal energy as shown in Figure 20.

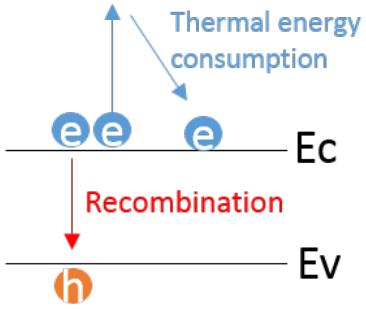

Figure 20: Auger recombination with associated excess energy given to an electron in conduction band.

Auger recombination rate is given by:

$$\begin{aligned} For\ p-type: U_A &= C_p * n * p^2, \\ For\ n-type: U_A &= C_n * n^2 * p, \end{aligned} \tag{9}$$

where C_p ($C_{p,silicon}$=1.2*10^{-31}cm^6/sec) and C_n ($C_{n,silicon}$=2.8*10^{-31}cm^6/sec)) are constants for a given semiconductor material. This recombination limits minority carrier lifetime, especially in the heavy doping regions such as emitter and back surface field (BSF).

2.3.2.3 Shockley Read Hall recombination

Shockley Read Hall (SRH) recombination occurs due to deep levels created by defects and impurities such as iron, chromium and oxygen in silicon wafers. As shown in Figure 21, generated electrons in conduction band (or holes in valence band) can recombine easily with the holes in valence band (or electrons in conduction band) due to the defect trapping levels by a two-step recombination process. Electrons/holes move from conduction/valence band edge to the defect level, and then move to the valence/conduction band edge, respectively. The emitted energy by this recombination process is consumed by lattice vibrations (phonons) or can be emitted as photon.

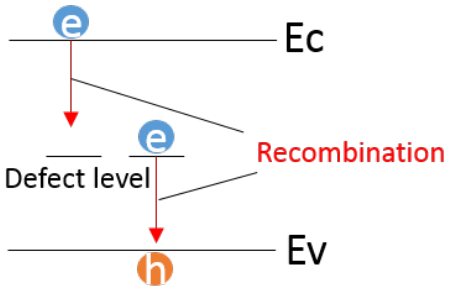

Figure 21: Schematic illustration of Shockely Read Hall recombination in the bandap.

In case of typical Czochralski grown silicon wafer, oxygen and iron are the dominant impurities which can be introduced during crystal growth or cell processing. The highest recombination rate occurs when defect level is near mid-sub since trapped electrons and holes cannot be easily re-emitted to conduction and valence band due to the trap depth. The formula for SRH recombination rate given by,

$$
\begin{aligned}
U_{\mathrm{SRH}} &= \frac{pn - {n_{\mathrm{i}}}^2}{\tau_{\mathrm{p0}}(n + n_1) + \tau_{\mathrm{n0}}(p + p_1)}, \\
\tau_{\mathrm{p0}} &= \frac{1}{\sigma_{\mathrm{p}} N_{\mathrm{t}} V_{\mathrm{th,p}}}, \quad \tau_{\mathrm{n0}} = \frac{1}{\sigma_{\mathrm{n}} N_{\mathrm{t}} V_{\mathrm{th,n}}}, \\
n_1 &= N_{\mathrm{c}} e^{-(\mathrm{E_c}-\mathrm{E_t})/\mathrm{kT}}, \; p_1 = N_{\mathrm{v}} e^{-(\mathrm{E_t}-\mathrm{E_v})/\mathrm{kT}},
\end{aligned}
\tag{10}
$$

where τ_{n0} and τ_{p0} are electron and hole lifetimes, σ_{p} and σ_{n} are hole and electron

capture cross sections, N_t is density of trapping defects, $V_{th,\,n}$ and $V_{th,\,p}$ are thermal velocity for electrons and holes, N_c and N_v are effective density of states for electrons and holes, E_c and E_v are conduction band edge and valence band edge, E_t is trap energy level, k is Boltzmann's constant, and T is temperature.

This bulk SRH recombination from defects in silicon wafer also can extended to descibe surface recombination by applying to the two-dimensional silicon surface as shown in Figure 22.

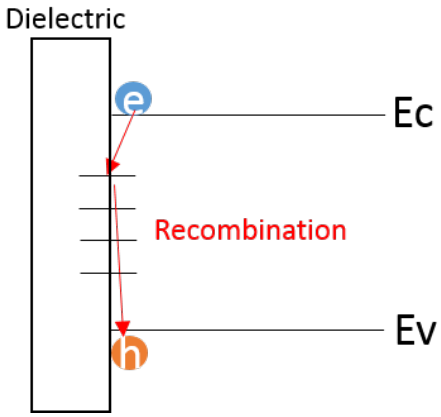

Figure 22: Schematic illustration of surface recombination by surface states in the bandap.

This recombination for each defect level can be described by the following Equation,

$$
\begin{aligned}
U_{s1} &= \frac{p_s n_s - {n_i}^2}{(n_s + n_1)/S_{p0} + (p_s + p_1)/S_{n0}}, \\
S_{p0} &= \sigma_n N_{ST} v_{th}, \\
S_{n0} &= \sigma_p N_{ST} v_{th},
\end{aligned}
\tag{11}
$$

where N_{ST} is the density of surface states, n_s and p_s are surface electron and hole concentrations, respectively and S_{n0} and S_{p0} are the characteristic surface recombination velocities for electrons and holes.

Total surface recombination rate of all the defects is described by integrating over energy E for all interface states within the semiconductor bandgap as described by

the following Equation,

$$U_{\mathrm{s,total}} = \int_{Ev}^{Ec} \frac{p_{\mathrm{s}} n_{\mathrm{s}} - {n_{\mathrm{i}}}^2}{(n_{\mathrm{s}} + n_1(E))/\sigma_{\mathrm{p}}(E) + (p_{\mathrm{s}} + p_1(E))/\sigma_{\mathrm{n}}(E)} v_{\mathrm{th}} D_{\mathrm{it}}(E) dE, \qquad (12)$$

where D_{it} is the surface defect density (cm^{-2}/eV), replacing N_{ST} in the previous single defect level version for U_{s1}.

This surface recombination can be reduced by decreasing the surface defect density or by increasing the concentration of one type of carriers at the surface. SRH recombination rate is maximum when n=p and decreasing when one type of carrier concentration becomes much larger than the other. This can be achieved by creating accumulation or inversion layers at the surface. Dangling Si bonds are a major source of surface defects. Reducing the number of surface state density can be achieved by growing an oxide or by hydrogenation from nitride coating, which passivates the dangling silicon bonds at the surface as shown in Figure 23.

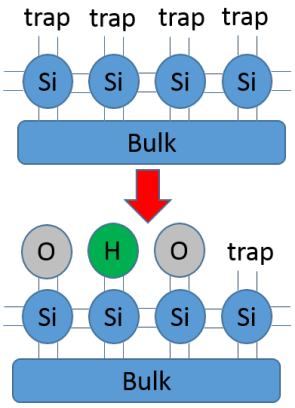

Figure 23: Schematic illustration of surface passivation by oxide (SiO_2) and hydrogenation during SiNx deposition.

Second approach to passivate the surface is to create asymmetric e-h concentrations. This can be achieved by field effect passivation which uses an electric field to repel one type of carrier from the surface and attract the other. The electric field can be induced either by additional doping at the surface or by introducing charge above the Si surface as shown in Figure 24. Often a charged dielectric is used for

this purpose. The field effect passivation will be used and discussed in more detail in Chapter 6 using a novel low-cost plasma charging method.

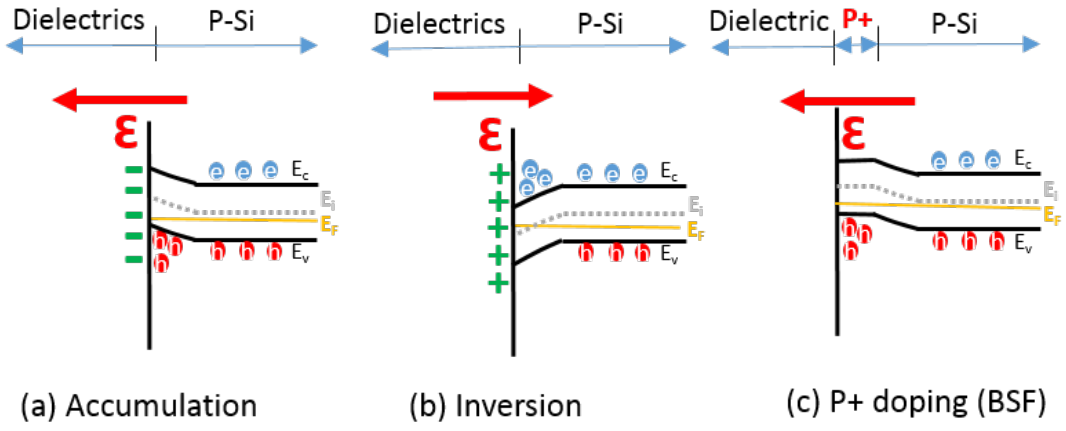

Figure 24: Schematic illustration of field effect passivations: (a) accumulation by negative charge (b) inversion by positive charge in dielectrics and (c) p+ doping for BSF (back surface field).

All these recombination losses (Radiative, Auger and SRH) occur simultaneously, in a solar cell structure including front and back surface, emitter, BSF and bulk. A well established Suns-Voc tool for metallized cell or QSSPC tool (quasi-steady state photoconductance) for un-metallized cell is frequently used in PV to extract effective lifetime (average generated electrons lifetime before recombing), combining all of these mechanisms. Effective lifetime can be written as,

$$
\begin{aligned}
U_{\text{eff}} &= U_{\text{front surface}} + U_{\text{rear surface}} + U_{\text{emitter}} + U_{\text{BSF}} + U_{\text{bulk}} \\
&(where \quad U = \frac{\Delta n}{\tau}) \\
\therefore \frac{1}{\tau_{\text{eff}}} &= \frac{1}{\tau_{\text{front surface}}} + \frac{1}{\tau_{\text{rear surface}}} + \frac{1}{\tau_{\text{emitter}}} + \frac{1}{\tau_{\text{BSF}}} + \frac{1}{\tau_{\text{bulk}}}.
\end{aligned}
\tag{13}
$$

2.3.3 Recombination in emitter, front surface field (FSF) and back surface field (BSF) regions

Emitter, FSF and BSF regions (n^+-p or p^+-n, n^+-n, p^+) are heavily doped to form a p-n junction or provide field effect passivations. These heavily doped regions induce Auger recombination and band-gap narrowing. Recombinations in such regions are

characterized by effective recombination velocity (S_{eff}) at the interface or saturation current density (J_o). J_o associated with emitter or BSF are often referred to J_{oe} and J_{ob}', respectively. Figure 25 shows that J_{oe} and S_{eff} are a function of surface recombination velocity (S_{n+}) and doping profile in n^+ region and are related according to Equation (14).

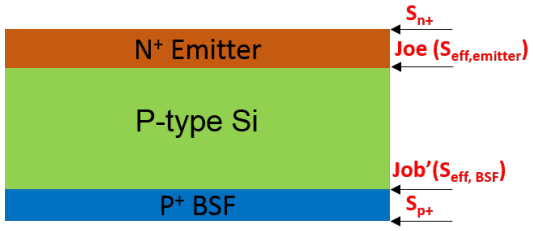

Figure 25: Schematic design featuring the effective recombination of heavily doped surfaces for emitter and BSF.

This is because recombination current in a heavily diffused region (n^+-p) can be expressed in terms of J_{oe} or S_{eff}.

$$\begin{aligned} J_{rec} &\simeq J_{oe} \exp\left(qV/kT\right) = J_{oe}\frac{np}{{n_i}^2} = J_{oe}\frac{(N_A + \Delta n)\Delta n}{{n_i}^2} \\ or \quad J_{rec} &= q\Delta n S_{eff} \\ \therefore S_{eff} &= \frac{J_{oe}(N_A + \Delta n)}{q{n_i}^2}, \end{aligned} \tag{14}$$

where N_A is the doping concentration in p-type base [28].

J_{oe} or J_{ob}'can be determined by QSSPC (quasi-steady state photoconductance) measurements on symmetric test structures [29] as shown in Figure 26.

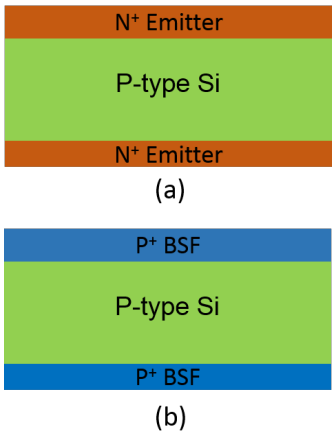

Figure 26: Schematic design featuring symmetric test structures for (a) J_{oe} (emitter) and (b) J_{ob}'(BSF).

The QSSPC tool measures effective lifetimes as a function of injection level by sensing photoconductance changes after shining short (∼20ms) and strong light (3∼20 suns). From this measured effective lifetime, the QSSPC tool extracts the slope of inverse lifetimes vs injection level (Δn) to calculate J_{oe} using the following Equation,

$$\frac{1}{\tau_{\text{eff}}} - \frac{1}{\tau_{\text{Auger}}} = \frac{1}{\tau_{\text{SRH}}} + 2\frac{J_{\text{oe}}(N_{\text{A}} + \Delta n)}{q{n_{\text{i}}}^2 W}, \tag{15}$$

where τ_{eff}, τ_{Auger} and τ_{SRH} are the measured effective lifetime, the intrinsic Auger and the intrinsic SRH lifetime, respectively, N_A is base wafer doping concentration,n_i is the intrinsic carrier concentration, Δn is excess carrier density and W is wafer thickness [28, 30].

Also, front and back metal-Si contact recombinations ($J_{oe,metal}$ and $J_{ob,\ metal}$) can be extracted in the same way after printing metal dots [31]. A linear plot of J_o as a function of metal extrapolated to extract J_o of the metalized region when metal fraction is 100%. With these measurements, solar cell V_{oc} can be determined by the

following Equation,

$$
\begin{aligned}
J_{\text{o,total}} &= J_{\text{oe}} + J_{\text{ob}} \\
J_{\text{oe}} &= J_{\text{oe, field}} * (1 - f_{\text{fm}}) + J_{\text{oe, metal}} * f_{\text{fm}} \\
J_{\text{ob}} &= J_{\text{ob, field}} * (1 - f_{\text{bm}}) + J_{\text{ob, metal}} * f_{\text{bm}} + J_{\text{ob,bulk}} \\
J_{\text{ob,bulk}} &= \frac{q * {n_{\text{i}}}^2 * w}{\tau * (N_{\text{A}} + \Delta n)} \\
V_{\text{oc}} &= \frac{kT}{q} ln(\frac{J_{\text{sc}}}{J_{\text{o,total}}} + 1)
\end{aligned}
\tag{16}
$$

where $J_{o,total}$ is total saturation current density, J_{oe} is emitter saturation current density ($J_{oe,\ field}$ is for non-metallized area and $J_{oe,\ metal}$ is for front metal-silicon contacted area), J_{ob} is saturation current density associated with base and back surface ($J_{ob,\ field}$ is for back surface non-metallized area and $J_{oe,\ metal}$ is for back surface metal-silicon contacted area), f_{fm} and f_{bm} are front and back metal-silicon contact fraction, respectively, q is elementary charge, n_i is intrinsic electron concentration, w is wafer thickness, N_A is base doping concentration, Δn is excess carrier density and k is boltzmann constant.

2.3.4 Resistive loss and series resistance components

Solar cells have also parasitic series and shunt resistance losses. These losses mainly affect FF.

1) Series resistance:

This resistance consists of several components shown in Figure 27. These components include busbar resistance (R_{bf}), metal gridline resistance (R_{finger}), front/back metal-silicon interface resistance (contact resistance, R_c), emitter resistance (R_e) and base substrate resistance (R_b). The analytical expressions for these components are as

follows,

$$
\begin{aligned}
R_{\mathrm{bf}} &= \frac{1}{3} * a * n^2 * b^2 * \frac{2 * r_{\mathrm{busbar}}}{l}, \\
R_{\mathrm{finger}} &= \frac{1}{3} * a * b * n_{\mathrm{gl}} * BBR, \\
R_{\mathrm{c}} &= r_{\mathrm{contact}} * \frac{2 * b}{w}, \\
R_{\mathrm{e}} &= \frac{1}{3} * b^2 * r_{\mathrm{sheet}}, \\
R_{\mathrm{b}} &= \rho * t, \\
R_{\mathrm{total}} &= R_{\mathrm{bf}} + R_{\mathrm{finger}} + R_{\mathrm{c}} + R_{\mathrm{e}} + R_{\mathrm{b}},
\end{aligned}
\tag{17}
$$

where a is the length of gridline in unit cell (Figure 28), b is a half gridline spacing, n is the number of gridlines per unit cell, n_{gl} is the number of gridlines in the whole solar cell, ρ is wafer resistivity, w is line width, and t is line thickness, BBR is busbar to busbar resistance, r_{busbar} is the resistance between one edge to the other edge in one busbar, $r_{contact}$ and r_{sheet} are contact and sheet resistances [32].

Figure 28 shows how BBR and r_{busbar} measured by simple four point prove measurements on a cell. $r_{contact}$ and r_{sheet} are measured by cutting 1cm wide slice of a cell (Figure 28) and performing the TLM measurements [32]. This allows the determination of all five components experimentally using Equation (17).

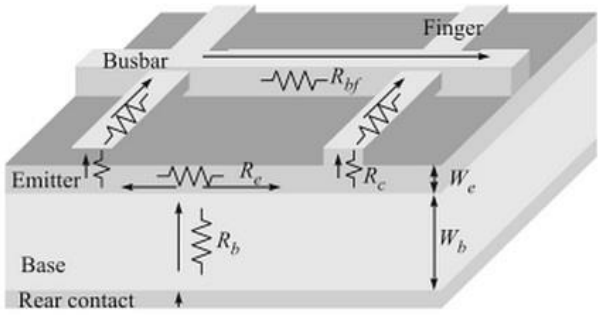

Figure 27: Series resistance components in a silicon solar cell [33].

Equation (17) indicates that R_{bf} and R_{finger} can be decreased by increasing width and height of metal. R_c can be decreased by increasing metal contact area. R_e and R_b can be reduced by increasing doping concentrations in the emitter and base

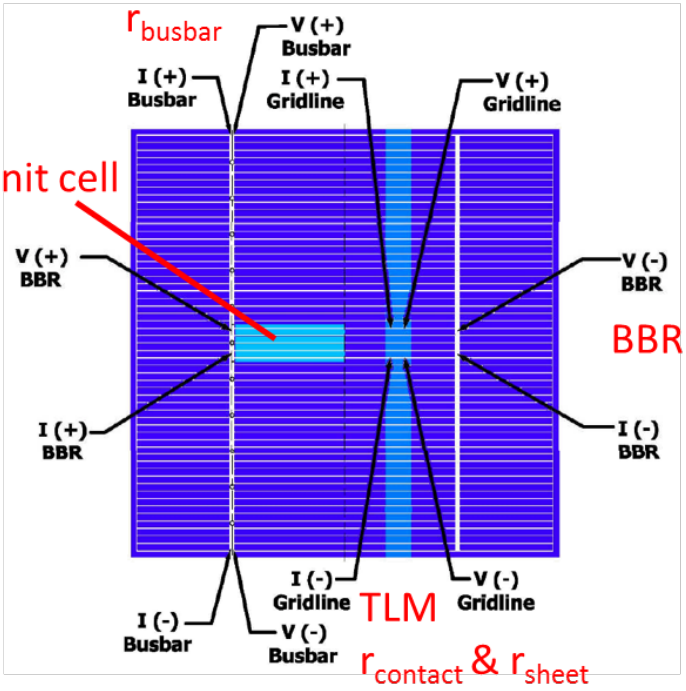

Figure 28: Front grid pattern showing placement of probes in a four-point measurement for determining series resistance components associated with BBR (busbar to busbar), busbar, contact resistance and emitter sheet resistance (gridline) [32].

wafer. However, increased metal area introduces shadowing losses in a solar cell by blocking sunlight while increased doping concentrations in the emitter and base increases Auger recombination. All these trade-offs need to be optimized to increase solar cell efficiency. In Chapter 5, a grid modeling program was used to account for all these losses and optimize the grid design.

2) Shunt resistance:

This resistance is caused by process-induced defects such as leakage across the p-n junction around the edge of the cell and in peripheral regions in the presence of crystal defects and precipitates of impurities in the junction area.

Series (r_s) and shunt resistances (r_{sh}) affect the fill factor (FF) according to the following Equations,

$$
\begin{aligned}
FF &= FF_{\mathrm{s}}[1 - \frac{v_{\mathrm{oc}} + 0.7}{v_{\mathrm{oc}}} * \frac{FF_{\mathrm{s}}}{r_{\mathrm{SH}}}], \\
FF_{\mathrm{s}} &= FF_{\mathrm{o}} * (1 - r_{\mathrm{s}}), \\
r_{\mathrm{s}} = \frac{R_{\mathrm{s}}}{R_{\mathrm{CH}}},\ R_{\mathrm{CH}} &= \frac{V_{\mathrm{oc}}}{I_{\mathrm{sc}}},\ r_{\mathrm{SH}} = \frac{R_{\mathrm{sh}}}{R_{\mathrm{CH}}}, \\
FF_{\mathrm{o}} = \frac{v_{\mathrm{oc}} - ln(v_{\mathrm{oc}} + 0.72)}{v_{\mathrm{oc}} + 1},\ v_{\mathrm{oc}} &= \frac{qV_{\mathrm{oc}}}{nkT},
\end{aligned}
\tag{18}
$$

where $\mathrm{I_{sc}}$ is short-circuit current, $\mathrm{V_{oc}}$ is open-circuit voltage, n is ideality factor, q is electronic charge, k is Boltzmann's constant, and T is temperature.

Since solar cell efficiency is proportional to FF, increasing the FF increases solar cell efficiency by decreasing series resistance and increasing shunt resistance.

CHAPTER III

LITERATURE SURVEY

3.1 History of Silicon Solar Cells

Although photovoltaic effect was observed by Alexandre-Edmond Becquerel in 1839, development of the first silicon solar cell was not until 1941 by Ohl *et al* [35,36]. While solar cell efficiency started at about 1% [34], today it has reached above 25% (Figure 29) with continuous innovations in cell design and technology. Despite efficiency boosts, solar cell industry in 1971 was limited to specific applications such as satellites, because of the high cost of PV modules (US$100/watt) [37]. However, after oil crisis in 1973, oil companies such as Exxon, ARCO, Shell, and Mobil started solar firms, and they were the largest producers of solar cells in the 1970s and 1980s [38]. Along with this, photovoltaics system was recognized as a promising renewable energy source, and many governments encouraged investments in PV by

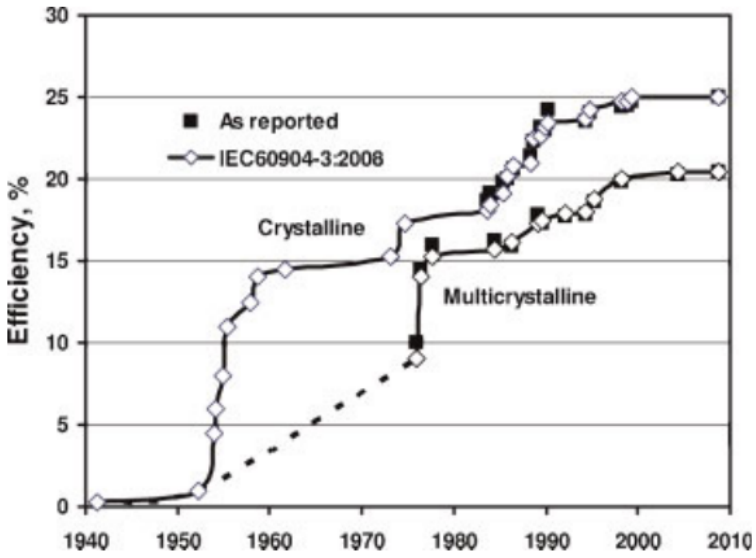

Figure 29: Evolution of crystalline and multi-crystalline silicon solar cell efficiency [34].

providing economic incentives through programs such as feed-in tariffs (National Energy Act in 1978 [39]). As a result, average photovoltaic module price has decreased dramatically from \$100/watt in 1976 to \$0.58/watt in 2015 [8] and cumulative PV installations have increased dramatically from ∼0.4MW in 1975 to ∼227GW in 2015 [8]. Since 2012, passivated emitter rear cells (PERC), which is the focus of this research, have gained commercial interest by several PV manufacturers (JA solar, Trina Solar, NeoSolar, Gintech, Hanwha Q Cells and Suntech). This is due to their higher efficiency potential (22.8% on 4 cm^2 float zone (FZ) silicon [40]) than standard full Al-BSF cells (∼20%), which have dominated the PV market share for more than 30 years. In addition, PERC cells are much cheaper compared to other higher efficiency commercial cell structures being produced today, such as n-type heterojunction solar cell with intrinsic thin layer (HIT) and interdigitated back contact (IBC) solar cells with efficiencies exceeding 25% [41, 42]. Currently, PV manufacturers are investing a large amount of resources to increase PERC cell efficiency to reduce the LCOE or total cost of PV system. Highest efficiency of 22.61% was reported recently for PERC cell on large-area Czochralski-grown wafers by Trina Solar [43]. According to the International Technology Roadmap for Photovoltaic (ITRPV), PERC solar cells accounted for ∼10% of the PV market shares in 2015, and are expected to dominate the PV market share (>40%) by 2026, as shown in Figure 30.

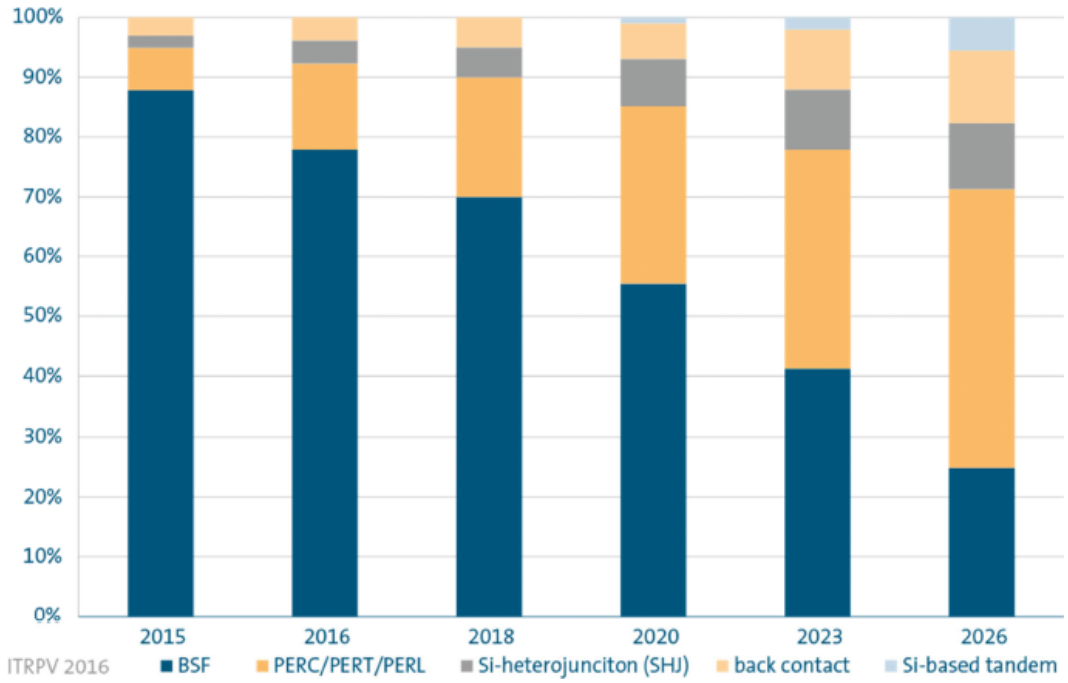

Figure 30: Worldwide market shares for different cell technologies [8].

3.2 Screen Printing Technology

Metal contact is required to transport generated current in the silicon to a load. Advent of screen printing technology for metal contact formation in the 1970′s allowed the PV industry to move away from expensive metal evaporation type processes including photolithography [44]. More than 95% of production of cells is currently using screen printing technology because it is simple, cheap and scalable with high throughput in excess of 2000 wafers/hour [13]. Figure 31 shows basic screen printing process, where screen has desired gridline patterns, formed by emulsion, through which metal paste is transferred or printed on the target wafer by moving squeegee with specific pressure. Conductivity of metal paste, contact resistance and fine line printing are same of the challenges compared to high quality evaporated contacts. This is because glass frit is used in the paste and printing is done through a screen.

To achieve high efficiency solar cells with this technology, it is important to have a low resistive paste, since power loss is a function of I^2R and R is proportional to

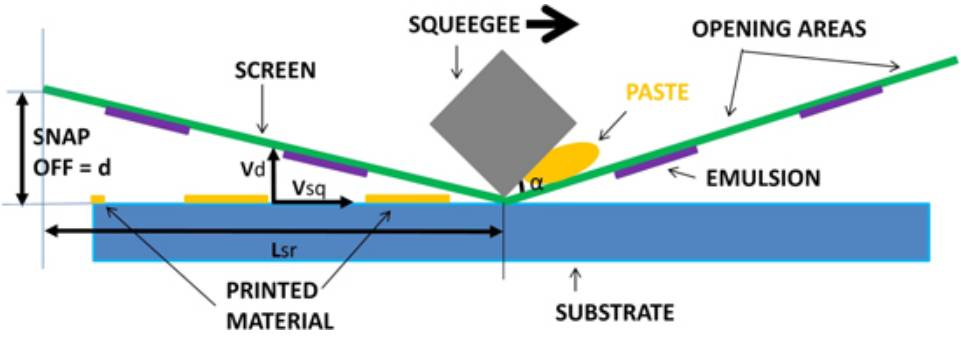

Figure 31: The elements involved in the screen printing mechanism [45].

resistivity ρ according to Equation (19),

$$R = \rho \frac{l}{A} \tag{19}$$

where l is length of a line, A is cross-sectional area of the line.

Since silver is the most conductive metal (Table 1), it is extensively used for screen printing today in spite of relatively high cost.

Table 1: Resistivity of Various Materials.

Material	Resistivity, ρ (Ω-m)at 20 °C
Silver	1.59x10-8
Copper	1.68x10-8
Gold	2.44x10-8
Aluminum	2.82x10-8
Tungsten	5.60x10-8
Zinc	5.90x10-8
Nickel	6.99x10-8

** Reference [46]

Moreover, optimizing screen design is crucial for this technology to minimize shading from sunlight by reducing metal contact area. Figure 32 shows the widely used grid pattern, called H-pattern, with three busbars for the front contact of silicon solar cell. Back side contact is, in general, fully covered by metal such as aluminium with

Figure 32: H-pattern, the most popular front contact design (horizontal lines: gridlines, vertical lines: busbars).

Ag tabs for soldering, since back side is not affected by shading loss. Gridlines collect the carriers or the electric current and feed it to the busbars, which then transport it to the external loads. Reducing the width or the number of the gridlines and busbars increases current collection because of reduced shading. However, this also increases resistance. Therefore, the grid pattern should be optimized using a grid design model which minimizes the power loss due to resistance and shading.

3.3 Light-induced Degradation

More than 95% of the PV industry (Figure 33 [13]) uses p-type boron doped Czochralski (Cz) wafers due low-cost and well-established technology and equipment base compared to n-type cells.

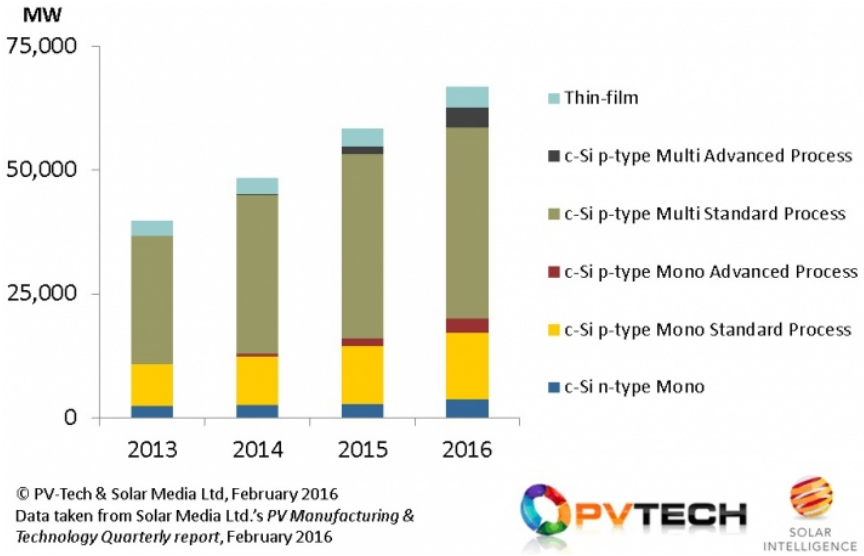

Figure 33: Annual market shares for different wafer types [13].

However, silicon solar cells on p-type Cz wafers are known to lose as much as ∼1% absolute efficiency after ∼24 hours of illumination. This phenamenon is called light-induced degradation (LID). The LID reduces minority carrier lifetime in the p-type silicon wafers which degrades the cell performance. LID is the result of interaction between interstitial oxygen (O) and substitutional boron (B) dopant. According to the current understanding, the oxygen dimmers (O_{2i}) diffuse under illumination and are captured by substitutional borons (B_s) to form B_s-O_{2i} complex as shown in Figure 34.

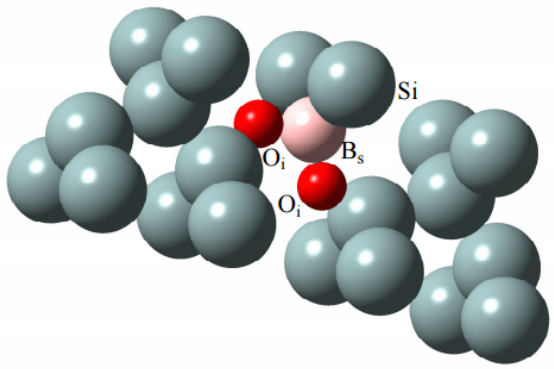

Figure 34: Schematic of possible metastable B_s-O_{2i} complex in the boron-doped silicon [47].

These complexes act as recombination sites [12, 47–51] and degrade bulk minority carrier lifetime according to the following Equation,

$$\tau(us) = 7.675 * 10^{45} * [B_s]^{-0.824} * [O_i]^{-1.748} \tag{20}$$

where τ is bulk lifetime, $[B_s]$ is substitutional boron concentration and $[O_i]$ is interstitial oxygen concentration [51].

Using the above equation, bulk lifetime of a ≥200 us industry standard boron doped 2 ohm-cm Cz wafers containing oxygen concentrations of ∼1e18 cm^{-3} should decrease to ∼30 us after LID. This lifetime reduction degrades absolute cell efficiency by 0.2∼0.7% for full Al-BSF cells. In case of advanced high efficiency cell structures, such as PERC, the detrimental effect of LID on efficiency can approach or exceed

1%, because bulk lifetime degradation can also mitigate the benefit of superior back surface passivation [12].

LID can be reduced or eliminated by choosing n-type material (phosphorus doped wafers), reducing oxygen and boron concentrations, deactivating B-O complexes or replacing boron (B) dopant by gallium (Ga) or indium (In) [15, 52–55]. Therefore, attempts are made in this research to eliminate or reduce LID in p-type solar cells.

CHAPTER IV

TASK 1: COMPARISON OF $POCL_3$ SOURCE TUBE DIFFUSION AND PHOSPHORUS ION IMPLANTATION TECHNOLOGIES FOR EMITTER FORMATION OF P-TYPE SOLAR CELLS

Most commercial cells today are made on p-type silicon wafers. P-type wafers generally have lower bulk lifetime and are more susceptible to metal impurities compared to the n-type wafers [56,57]. It has been reported that the minority carrier lifetime in p-type Si is frequently limited by iron (Fe) related defects [58,59] with larger electron capture cross section [60]. Iron is often present in the feedstock material and can be introduced during processing [61]. Therefore, most cell manufacturers currently use $POCl_3$ diffusion to remove metal impurities including iron [62]- [66] and to form n^+ emitter. Simultaneously some companies have started using ion implantation to form n^+ emitters. Although the formation of the phosphorus emitter is known to getter or remove impurities like iron from the bulk, the impact of these two emitter formation and gettering techniques on cell performance is not well quantified and compared. Therefore, the objective of this task is to compare the emitter quality and gettering efficiency of $POCl_3$ diffusion and phosphorus ion-implantation technologies on cells made on widely used single crystalline Cz Si wafers as well as cast multicrystalline Si wafers with some defects. Commercial grade 200 um thick 1-2 Ω-cm p-type Cz wafers (boron doped, 239 cm^2) and cast quasi-mono Si wafers (boron doped, 243.34 cm^2) were used in this research. Two systematic studies were conducted. The first study involved determination of iron concentration and bulk lifetime (Figure 35) in Si wafers before and after the two diffusion technologies.

Second study involved complete cell fabrication using the two different diffusion technologies and evaluating the difference in key cell parameters and emitter saturation current density (J_{oe}). Both bulk lifetime and J_{oe} have significant impact on the cell efficiency.

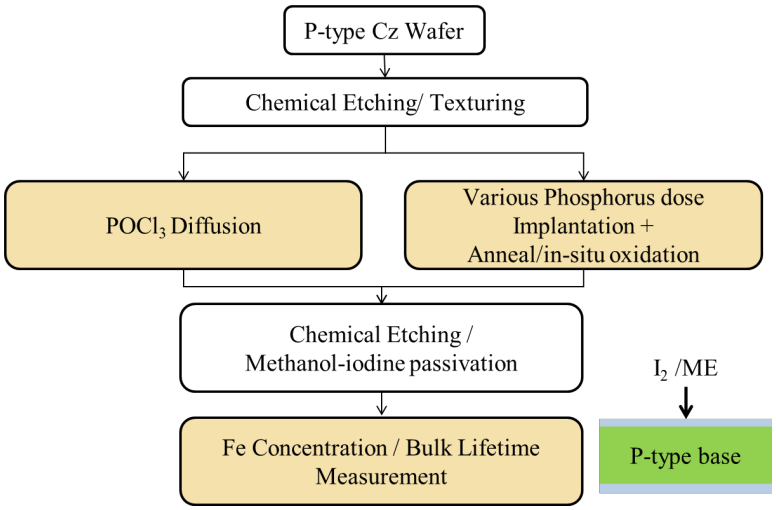

Figure 35: Procedure and structure for iron concentration and bulk lifetime measurements.

In the first experiment, bulk lifetime and iron concentration were measured in as-grown, $POCl_3$ diffused, and implanted p-type Cz wafers (2 ohm-cm). This was accomplished by the well established quasi-steady-state photoconductance (QSSPC) technique using Sinton lifetime tool (WCT-120) [29]. Prior to the measurements, Cz wafers were subjected to saw damage etching in KOH solution followed by alkaline texturing process. Emitters were formed by $POCl_3$ diffusion in a tube which diffuses phosphorus on both sides of the wafers. Phosphorus implantation was performed on the front side only using an Applied Materials Solion tool. The implantation dose was varied in the range of 1-3x10^{15} cm^{-2} followed by a drive-in in a tube furnace. Total diffusion time was kept at 30 minutes for both techniques. $POCl_3$ emitter was formed by 20 minutes $POCl_3$ diffusion followed by 10 minutes in-situ anneal in N_2 at 850°C. The implanted Cz wafers were annealed at 850°C for 20 minutes in oxygen to grow a high quality $250\mathring{A}$ thick oxide followed by 10 minutes in-situ anneal

in N_2. These diffused wafers were etched back 20um from each side in KOH for 15 minutes at 850°C down to bare Si, and then passivated by immersing in iodine-methanol solution(I_2/ME) for bulk lifetime measurements and iron concentration determination by QSSPC technique (Figure 35). Iodine-methanol solution is known to passivate surfaces and reduce surface recombination velocity to 1-3cm/s so the photo-conductance decay is essentially governed by bulk recombination and lifetime.

The second study involved complete cell fabrication (Figures 36) with phosphorus ion implantation and $POCl_3$ diffusion followed by detailed characterization and PC1D device modeling.

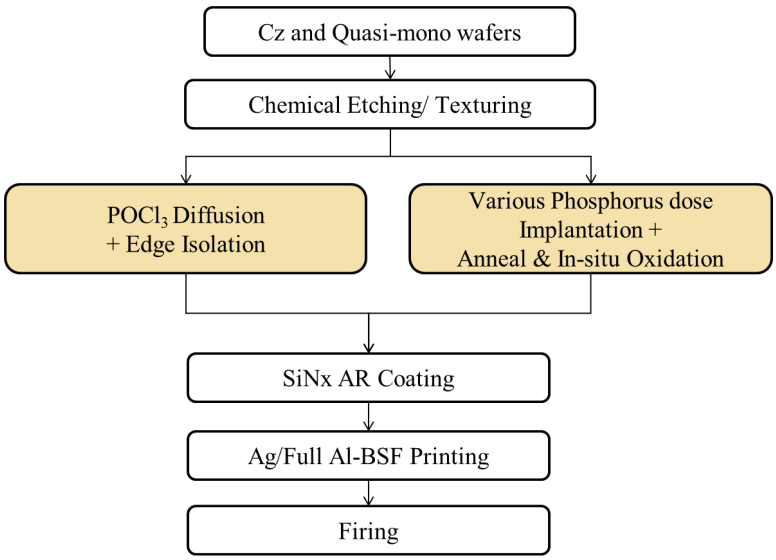

Figure 36: Cell fabrication procedures of phosphorus ion-implanted and $POCl_3$ diffused solar cells.

In the second experiment, large area screen printed p-type industrial cells with full aluminum back surface field (full Al-BSF) were fabricated on both Cz and cast quasi-mono wafers according to a process sequence shown in Figure 36. After the emitter formation ($POCl_3$ diffusion or phosphorus implantation), SiNx anti-reflection coating was deposited on the front side of all wafers. Industrial screen printing technology was used to print Ag gridline and busbars on the front and full Al on the back side. Finally, cells were co-fired in a belt furnace to form the Ag contacts through

the SiNx film on the front and full area Al-BSF on the back. The final cell structure is shown in Figure 37.

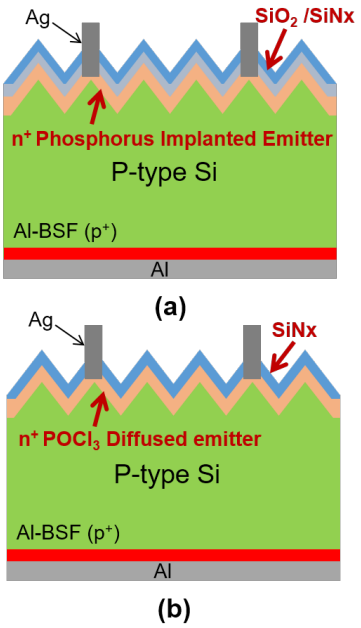

Figure 37: Full Al-BSF cell structures of (a) phosphorus ion-implanted cell with SiO_2/SiNx emitter passivation and (b) $POCl_3$ diffused cell with only SiNx emitter passivation.

Symmetric test structures (Figure 38) were also fabricated on high bulk lifetime n-type wafers to measure saturation current density (Joe) to compare the emitter quality due to the impact of oxide passivation in ion implanted emitter.

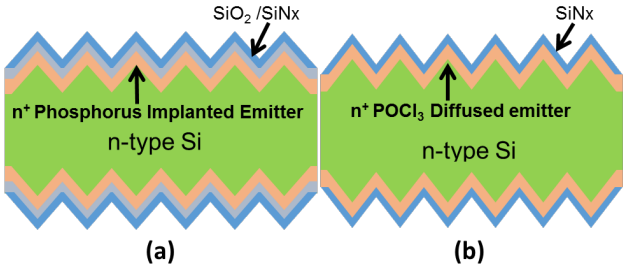

Figure 38: Symmetric test structures for measuring saturation density current (Joe) of (a) phosphorus implanted and (b) $POCl_3$ diffused emitters.

After fabricating the cells, detailed characterization and modeling of these cells

were performed by photoluminescence(PL, 808nm), light and dark I-V tests and internal quantum efficiency (IQE) measurements in conjunction with PC1D device simulation to quantitatively understand the difference in the two emitter technologies.

4.1 Bulk Lifetime Measurements and Analysis to Determine Iron Concentration Before and After Emitter Diffusion

Since Fe (iron) is known to be a dominant source of lifetime degradation in p-type solar grade Si wafers [67], an attempt was made to determine Fe concentration and bulk lifetime to assess the difference in impurity gettering efficiency of $POCl_3$ diffusion and ion implantation technologies. Fe is either present in the starting wafer or introduced in the bulk Si during high temperature processing. The Fe concentration (cm^{-3}) in the wafers was obtained by a method described by Zoth and Bergholz, which measures effective lifetimes before and after light exposure as a function of injection level. The two lifetimes are different because initial lifetime (τ_{eff0})is determined by FeB defect but after light exposure Fe interstitials determine lifetime (τ_{eff1}) because light exposure dissociates FeB into Fe_i. This method uses following Equation (21) to determine Fe concentration,

$$[Fe] = C(\frac{1}{\tau_{\text{eff1}}} - \frac{1}{\tau_{\text{eff0}}}), \tag{21}$$

prefactor value of C of -3.0e-14 cm^{-3} is used for 2 Ω-cm at 1e15 cm^{-3} injection level based on the work of Macdonald which assume that all other recombination processes remain unchanged [56, 68]. This technique has been widely used for estimating Fe concentration in silicon wafers used in microelectronics industry, especially when other defects are not affected or dissociated by the light source [67, 69]. Effective lifetime as a function of injection level was measured by the QSSPC method before and after light exposure using Sinton WCT-120 tool. A strong light source (> 20 suns) in the Sinton tool was used to dissociate the FeB pair to form interstitial iron

(Fe_i) which has higher electron capture cross section ($\sigma_{n,Fei}$=5e-14cm^{-2} vs $\sigma_{n,FeB}$=3e-14cm^{-2}) and much lower hole capture cross section ($\sigma_{p,Fei}$=7e-17cm^{-2} vs $\sigma_{p,FeB}$=2e-15 cm^{-2}). SRH lifetime swings from τ_{no} at low level injection to $\tau_{no}+\tau_{po}$ at high level injection. Since τ_{no} and τ_{po} are inversely related to electron and hole capture cross sections, respectively, τ_{po} is greater than τ_{no} for both the defects therefore bulk lifetime increases first with the injection level from $\tau_{no}+\tau_{po}$ and then decreases due to Auger recombination after injection level of >1e16 cm^{-3} (Figure 39). Macdonald showed that the difference in σ_n and σ_p for the two Fe defects leads to a crossover point at 1.5e14 cm^{-3} injection level for the two lifetime curves shown in Figure 39, before and after light exposure (Figure 39). This crossover point also serves as the fingerprint of Fe in silicon [56].

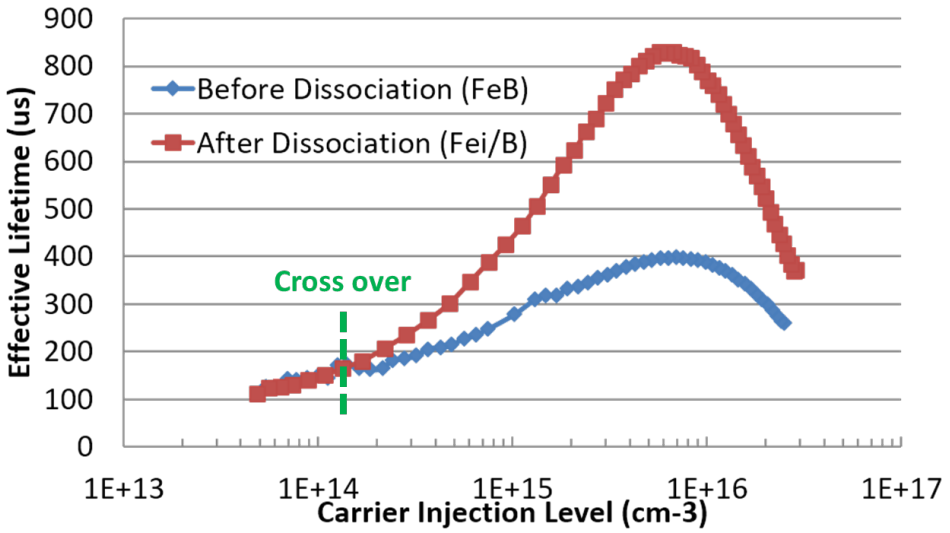

Figure 39: Measured effective lifetime versus carrier injection level for phosphorus implanted wafer with 2e15 cm^{-2} dose.

Figure 40 shows measured effective lifetimes at 1e15cm^{-3} injection level (which is close to the injection level at open circuit voltage of ~660 mV) before and after dissociation of FeB pair for as-grown wafers, after annealing with various phosphorus implantation doses and after the $POCl_3$ diffusion.

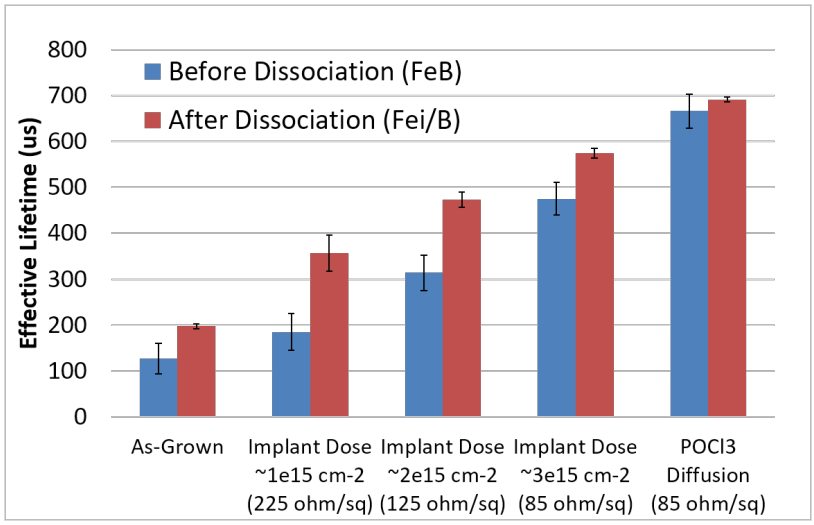

Figure 40: Measured effective lifetime at 1e15cm^{-3} injection level on Cz wafers (2ohm-cm) before and after light dissociation of FeB pair.

Total Fe concentration was calculated using Equation (21) from measured effective lifetimes before and after the light exposure at an injection level of 1e15cm^{-3} in Figure 41. Figure 41 also shows measured bulk lifetimes after each emitter formation process.

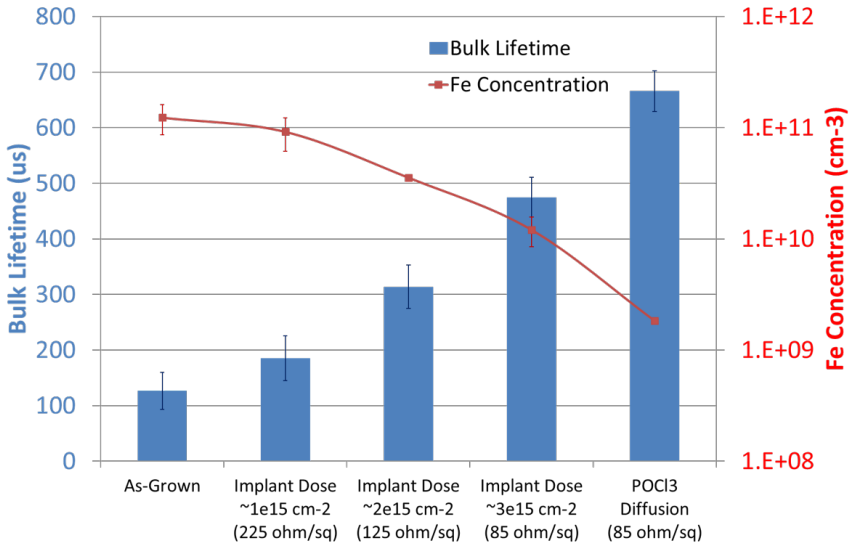

Figure 41: Measured bulk lifetime and iron concentration in the Cz wafers after $POCl_3$ and implanted diffusion.

It shows that higher phosphorus implanted dose results in lower iron concentration and higher bulk lifetime in the single crystal Cz wafer. However, highest bulk lifetime (∼650us) was achieved after the $POCl_3$ diffusion process in this study because it provides a more effective sink for impurity gettering on both surfaces as opposed to single side gettering in ion-implantation (∼450us). Higher phosphorus surface concentration in $POCl_3$ diffused emitter (Figure 42) near the surface creates more lattice strain and misfit dislocations to provide low free energy site or better sink for bulk impurities compared to ion implanted emitter [70].

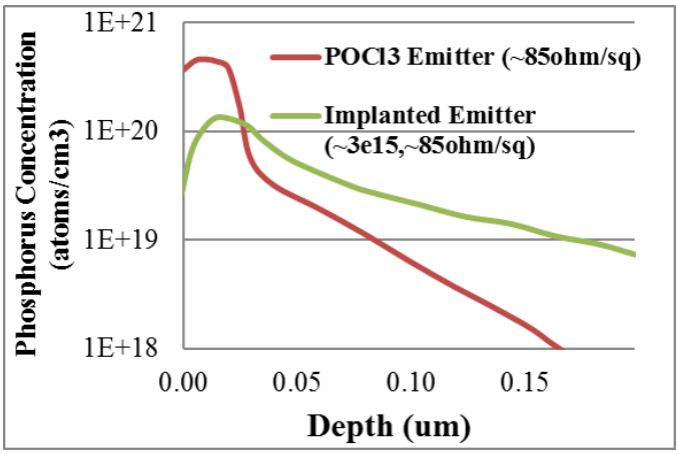

Figure 42: Measured electrochemical capacitance-voltage(ECV) profiles of implanted and $POCl_3$ diffused emitters.

Figure 43 depicts the well known impurity gettered mechanism by phosphorus diffusion [56]. Phosphorus diffusion injects Si interstitials into the bulk which kick out substitutional impurities into the interstitial site which are then free to move to the misfit dislocation sink at the surface during high temperature diffusion. Higher phosphorus concentration on both surfaces lead to higher impurity segregation coefficient during $POCl_3$ diffusion.

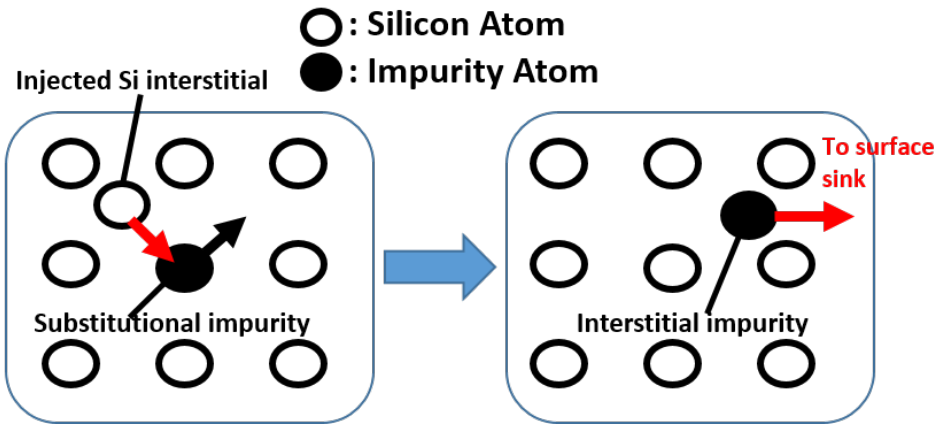

Figure 43: Schematic of interstitialcy diffusion process and impurity gettering mechanism of phosphorus diffusion.

Figure 41 shows that the measured bulk lifetime increases with the decrease in measured iron concentration, confirming that iron contamination is the major sources of bulk lifetime degradation in these p-type samples. Consistent with the literature [66,71,72], these results also indicate that gettering efficiency of phosphorus diffusion increases with the increase in phosphorus surface concentration, which was found to be highest for $POCl_3$ diffusion compared to the ion-implanted samples (Figure 42). Since phosphorus surface concentration is a function of implantation dose, gettering efficiency or bulk lifetime was found to increase with the implantation dose (Figure 41).

4.2 Effect of Phosphorus Gettering on the Performance of Full Al-BSF Solar Cells on Cast Quasi-mono and Czochralski-grown Si Wafers

After quantifying the gettering efficiency of the two diffusion technologies, complete solar cells were fabricated on Cz and cast quasi-mono Si materials with $POCl_3$ diffusion and phosphorus implanted dose of 3e15 cm^{-2}. The measured light I-V data and solar cell efficiencies are summarized in Table 2.

Table 2: Measured IV Data of Quasi-mono and Cz Wafers.

Wafer Type	Emitter	V_{oc} (mV)	J_{sc} (mA/cm^2)	FF(%)	Efficiency (%)
Cast Quasi-mono	$POCl_3$	628	37.4	79.4	18.6 ± 0.10
AVG(6)	Implanted (3e15cm^{-2} dose)	625	37.1	78.5	18.2 ± 0.08
Cz	$POCl_3$	637	37.8	79.2	19.1 ± 0.13
AVG(6)	Implanted (3e15cm^{-2} dose)	643	37.9	79.5	19.4 ± 0.09

For the cast quasi-mono material, $POCl_3$ diffused cells showed 0.4% higher cell efficiency (18.6% vs 18.2% for implanted cell) because this material has a low starting bulk lifetime (< 100us, Figure 44) which benefits from superior and double side $POCl_3$ gettering. Figure 44 shows that $POCl_3$ diffusion increased bulk lifetime of the cast Si used in this study from ∼80us to ∼330us while the phosphorus implanted wafers reached a lifetime of only ∼200us. Because of higher bulk lifetime, cell V_{oc}, J_{sc} and FF were also higher for $POCl_3$ diffused cast Si cells (Table 2). However, Cz solar cells showed a reverse trend in efficiency where implanted cells achieved ∼0.3% higher efficiency compared to the $POCl_3$ diffused cells in spite of lower bulk lifetime (∼450us as opposed to ∼650us for $POCl_3$ diffusion, Figure 44).

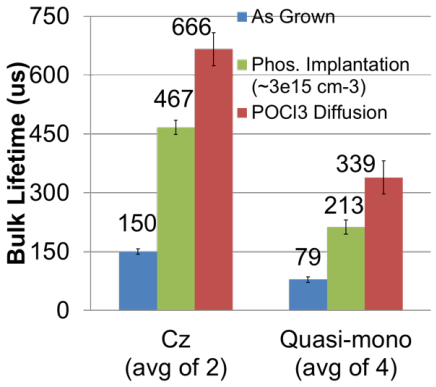

Figure 44: Measured bulk lifetime on Cz and Cast Quasi-mono wafers on three different conditions by the procedure in Figure 35.

In order to explain this controversy, PC1D device modeling was performed to calculate cell efficiency as a function of bulk lifetime (Figure 45) which revealed that cell efficiency saturates after ~250us bulk lifetime for the full Al-BSF cell structures fabricated in this study.

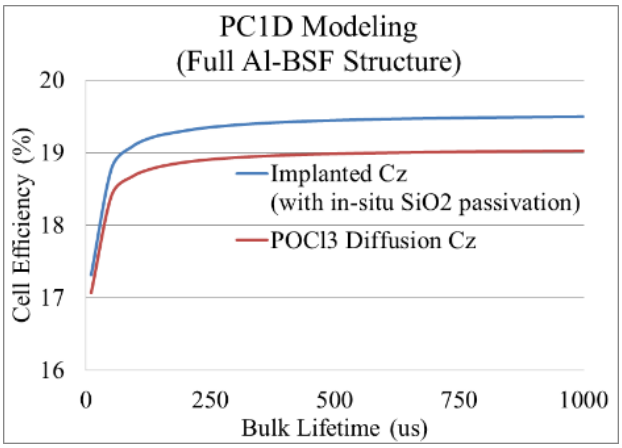

Figure 45: PC1D modeling for full Al-BSF Cz cells.

Therefore, higher bulk lifetime (~650us) in $POCl_3$ diffused cell does not help efficiency appreciably. However, the implanted cells had lower emitter saturation current density (J_{oe}) compared to the $POCl_3$ diffused cells (67 fA/cm^2 vs 215 fA/cm^2) because of in-situ emitter oxide passivation during implantation anneal as shown in Figure 46. J_{oe} values were determined by QSSPC measurements on symmetrically diffused test samples.

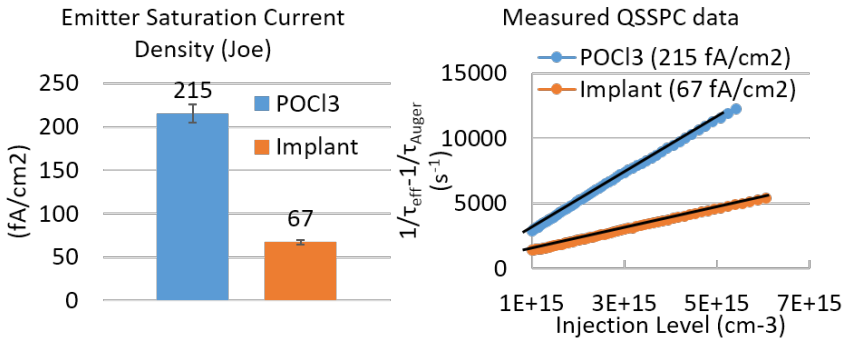

Figure 46: Measured J_{oe} on test structures of implanted and $POCl_3$ diffused emitter in Figure 38.

The lower J_{oe} of the implanted emitter contributed to 6mV higher V_{oc} (Table 2) because $V_{oc} \simeq kT/q * \ln(J_{sc}/(J_{oe}+J_{ob}))$, accounting for the observed ~0.3% increase in efficiency in spite of lower bulk lifetime.

It is also interesting to note that implanted cast quasi-mono cells showed lower V_{oc} and efficiency compared to the $POCl_3$ diffused cells in spite of superior oxide passivation or J_{oe}. This is because the bulk lifetime in the implanted cast quasi-mono cells was much lower (210 us) compared to the $POCl_3$ diffused cells (350 us, Figure 44). Therefore, the loss in V_{oc} or efficiency due to lower bulk lifetime in implanted cast quasi-mono cell was greater than the gain in V_{oc} due to lower J_{oe} (Figure 45). In order to support this conclusion, Photoluminescence (PL) measurements were performed on the entire cell area to look for recombination properties of the cell. PL map provides the total recombination image including the bulk and emitter recombination. Figure 47 confirms that $POCl_3$ diffused cast quasi-mono cell has higher effective lifetime than the implanted cast Si cells due to superior gettering which shows up as reduced net recombination in spite of higher emitter recombination or J_{oe}. Since bulk lifetime values are low in cast Si samples PL responses are dominated by bulk recombination than emitter recombination.

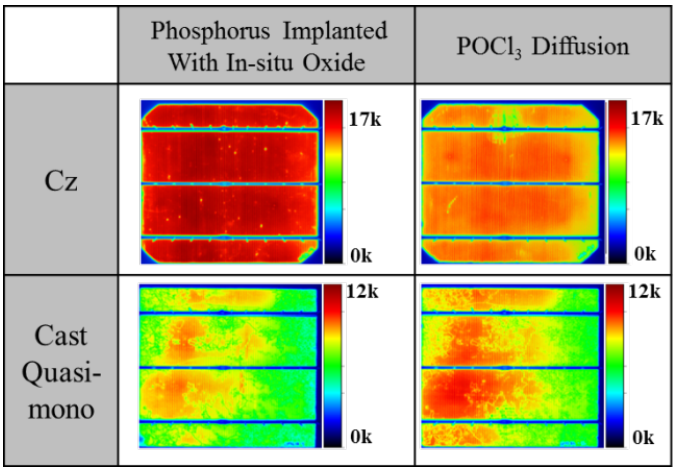

Figure 47: PL images (808 nm) of implanted and $POCl_3$ diffused Cz and cast quasi-mono Si Cells. Red corresponds to high effective lifetime.

Contrary to the cast Si cells, PL measurements on implanted Cz cells showed higher effective lifetime or lower net recombination than $POCl_3$ diffused cells in spite of lower bulk lifetime. This is because bulk lifetime is quite high in both Cz samples so total recombination is dominated by emitter recombination which is much lower for implanted cells due to oxide surface passivation. PC1D device simulation and IQE measurements were also performed on both Cz and cast quasi-mono cells with $POCl_3$ and implanted emitters (Table 3 and Figure 48) to understand and validate the above conclusions. A good match between measured and simulated data was achieved by adjusting the bulk lifetime in modeling. It was found that, compared to the bulk lifetime measured at 1e15cm^{-3} injection level (Figure 44) in wafers after diffusion, a lower bulk lifetime had to be used in PC1D modeling of the finished cells (Figure 48) to obtain the best fit to the experimental IQE and cell data. This is partly because injection level dependence in these cells showed lower bulk lifetime at maximum power point which corresponds to an injection level of ~3e13cm^{-3} [73] instead of ~1E15 cm^2 at open circuit point used for lifetime measurement numbers in Figure 48.

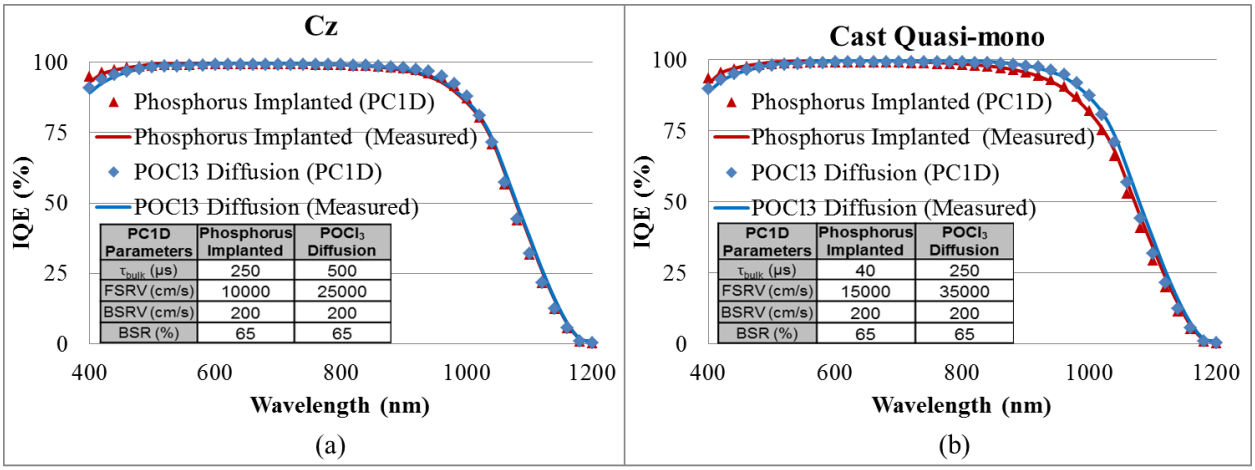

Figure 48: Measured and PC1D fitted IQE data of (a) Cz and (b) cast quasi-mono solar cells with full Al-BSF.

Table 3: PC1D Simulation on Cz and Cast Quasi-mono Solar Cells.

Cell Parameters	Cz		Cast Quasi-mono	
	Implanted (3e15 cm^{-2} dose)	$POCl_3$ diffusion	Implanted (3e15 cm^{-2} dose)	$POCl_3$ diffusion
Wafer thickness (um)	190	190	190	190
Base Resistivity (Ω-cm)	1.5	1.5	1.5	1.5
R_{series} (Ω-cm^2)	0.60	0.71	0.50	0.53
R_{shunt}(Ω-cm^2)	4950	3007	5640	7842
Cell bulk lifetime (us)	250	500	40	250
BSRV (cm/s)	200	200	200	200
FSRV (cm/s)	10000	25000	15000	35000
R_{back}	65	65	65	65
Modeled V_{oc} (mV)	643	637	624	630
Modeled J_{sc} (mA/cm^2)	37.9	37.8	37.4	37.7
Modeled FF (%)	79.6	78.9	78.5	78.5
Modeled Efficiency (%) test	19.4	19.0	18.3	18.6

Note that PC1D device modeling gave a very good match with the measured light I-V data (Tables 2 and 3) and IQE response (Figure 48) for the PC1D input parameters shown in Table 3. As expected, $POCl_3$ diffused cast quasi-mono cells showed higher IQE response in the long wavelength (800nm$\sim$1100nm) due to superior bulk lifetime compared to the implanted cells. This explains the reason for the observed $\sim$0.4% higher efficiency of $POCl_3$ diffused cast Si cells compared to implanted cells (Table 2 and 3). However, in the case of Cz cells, very little difference was observed in the long wavelength response of $POCl_3$ diffused and implanted cells because bulk lifetime is so high that the long wavelength response or effective lifetime is limited by the back surface recombination velocity(BSRV). It is important to note that implanted Cz cells showed higher response in the short wavelength range (350nm$\sim$500nm) due

to lower front surface recombination velocity (FSRV) or J_{oe} because of the in-situ oxide passivation. This explains ~0.3% higher efficiency of implanted Cz cells compared to the $POCl_3$ diffused Cz cells.

4.3 Conclusion

This chapter showed a detailed investigation of the $POCl_3$ diffused and implanted cells on Cz and cast Si materials with some defects. Since high bulk lifetime is cruial for higher efficiency and bulk lifetime is controlled by impurities and defects in Si. Formation of both $POCl_3$ diffused and ion implanted emitters show the promise and ability to getter bulk impurities but the gettering efficiency of $POCl_3$ diffusion is found to be superior. This was the result of higher phosphorus concentration observed near the surface (Figure 42) in $POCl_3$ diffused emitter, which creates more sites and misfit dislocations to provide a better sink for impurities near the surface. In addition, $POCl_3$ diffusion provides double side gettering during the diffusion process while ion implantation is done only on one side. This was confirmed by in-depth measurements and analysis of iron concentration in the bulk and bulk lifetime in the Cz and cast Si wafers before and after $POCl_3$ diffusion and phosphorus implantation. Ion implantation dose was varied in the range of 1-3e15 cm^{-2} to vary the surface phosphorus concentration (N_s) and see the impact of dose on gettering. Large area screen printed commercial ready cells with full Al-BSF were fabricated and analyzed in this task to support the findings of bulk lifetime and J_{oe} studies. In the case of cast quasi-mono solar cells, with more defects, the $POCl_3$ diffused emitter gave ~0.4% higher cell efficiency (18.6%) compared to the implanted emitter (18.2%). This was consistent with higher bulk lifetime (~210 vs ~340 us) measured in the $POCl_3$ diffused wafers compared to ion implanted samples. However, J_{oe} of ion implanted emitter was superior but it was unable to overcome the negative effect of lower bulk lifetime in the cast material. In contrast, ion implanted Cz Si solar cells showed

$\sim$0.3% higher absolute efficiency (19.4% VS 19.1%) due to lower J_{oe} (67fA/cm^2 vs 215fA/cm^2) compared to the $POCl_3$ diffused cells. Lower J_{oe} of the implanted cells is the result of in-situ oxide surface passivation during implant anneal. The $POCl_3$ diffused emitters have only SiNx passivation while implanted emitters have SiO_2/SiNx passivation. It is important to note that in the case of Cz cells, positive effect of lower J_{oe} was able to overcompensate the negative impact of lower bulk lifetime ($\sim$450us vs $\sim$650us). Device modeling showed that this is because lifetime above 250us has no appreciable effect on the efficiency of full Al-BSF cell structure but lower J_{oe} gave higher V_{oc} and efficiency in Cz cells. Thus, ion implantation was found to be superior for higher quality Cz materials but $POCl_3$ diffusion gave better efficiency for lower quality cast silicon materials. Since ion implanted Cz cells gave best efficiency, we selected phosphorus ion implantation and Cz silicon wafers to achieve high efficiency in remaining tasks.

CHAPTER V

TASK 2: ANALYTICAL MODELING, DESIGN AND DEVELOPMENT OF MULTI-BUSBAR AND FINE GRIDLINE PRINTING

In the previous task, baseline cells with full Al-BSF were fabricated. In this task, we switched to a more advanced cell structure, called PERC which involoves dielectric passivation and local Al-BSF on the back. This concept improves back surface passivation and back reflection and is more sensitive to bulk lifetime. Structure and fabrication process of the PERC cells are shown in Figure 49.

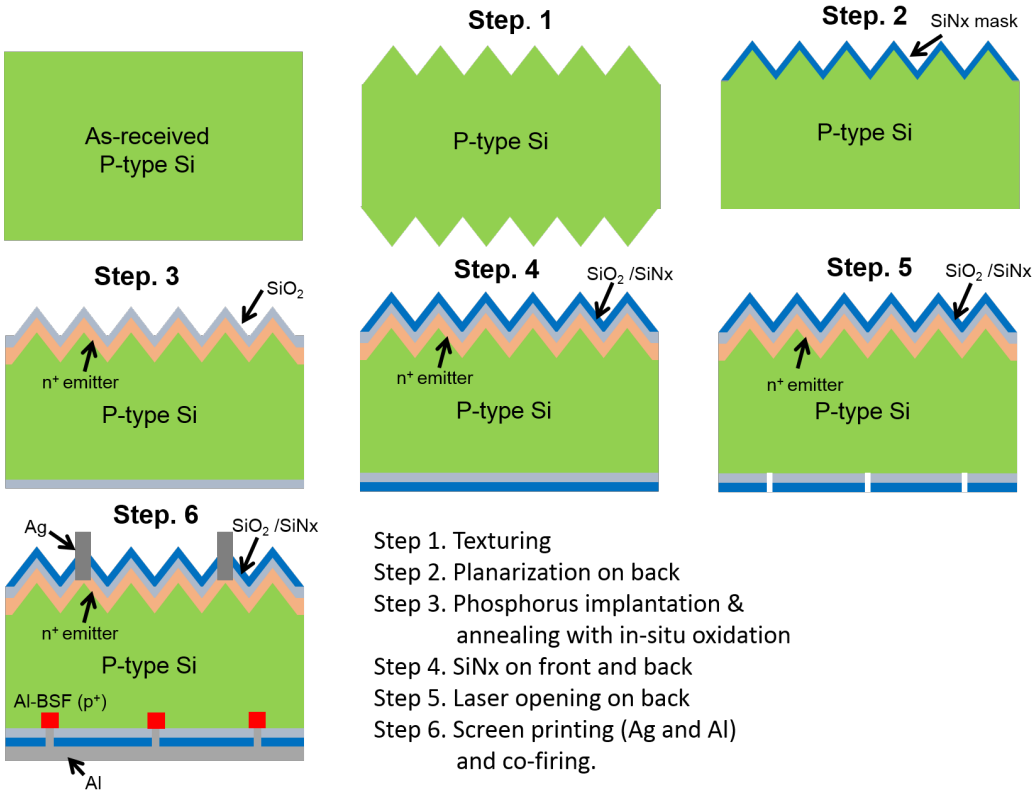

Figure 49: Passivated emitter rear cell (PERC) structure and fabrication procedures.

1) First, as received p-type Cz silicon wafers are dipped in heated (80°C) KOH solution for saw damage removal followed by pyramid-like alkaline texturing of both surfaces. This textured surface increase the sunlight absorbtion by decreasing the average weighted front surface reflectance from 30% on bare silicon to ∼9%.

2) Then, rear side is planarized by capping the front side with SiNx and using heated (65°C) KOH solution for back planarization. Planarized back surface increases back surface reflectance and light trapping in the cell before light can escape as explained in Chapter 2.

3) Phosphorus ion-implantation was performed with 10keV with 2.8e15 cm^{-2} dose followed by annealing which involved 10-minute drive-in in N_2 and 20-minute oxidation at 855°C to grow on in-situ oxide for surface passivation. These conditions resulted in a phosphorus homogeneous emitter with ∼90/sq sheet resistance. In-situ thin oxidation resulted in 25nm oxide on front and 8nm oxide on the rear with very low J_o value of 70 fA/cm^2.

4) Next, 45nm thick PECVD SiNx film (index of 2.1) was deposited on the front 25nm oxide for anti-reflection (AR) coating and 200nm SiNx on the back for protecting the oxide and improving the back surface reflectance. The front SiNx AR coating on the textured surface decreases reflectance to ∼4%. The back SiNx increases back reflectance to ∼97% (without metal contact), which increases the number of photons re-entering the cell.

5) A green laser (Rofin Laser, 532 nm wavelength with nanosecond pulse width) was used to open a line pattern through the rear dielectric stack (65um wide and 1mm pitch). This is to form a local aluminium (Al) back surface field (BSF), decreasing metal-silicon contact area from 100% (full Al-BSF cell) to 6.5% (PERC).

6) Finally, a Ag grid was screen printed on the front SiNx using a Dupont paste and full Al (Ruxing paste) was screen printed on top of the back dielectric, followed by co-firing (peak temperature of ∼740°C) in a Despatch belt furnace, for simultaneous

formation front and back metal contacts including the local Al-BSF (Figure 49). Front Ag metal paste fires through SiO_2/SiNx stack but back Al metal paste does not.

In this task, we incorporated two advanced metallization features (five busbars and fine line printing) to achieve higher efficiency p-type PERC solar cell.

5.1 Design and Implementation of Optimized Five-busbar Technology to Reduce Resistive Losses

In order to optimize front-contact grid pattern, we need to address the trade-off among series resistance loss, grid shadow and metal-silicon contact recombination. In this section, optimization of the grid design or number of gridlines and busbars (Figure 50) is investigated analytically by minimizing total loss associated with the above three mechanisms.

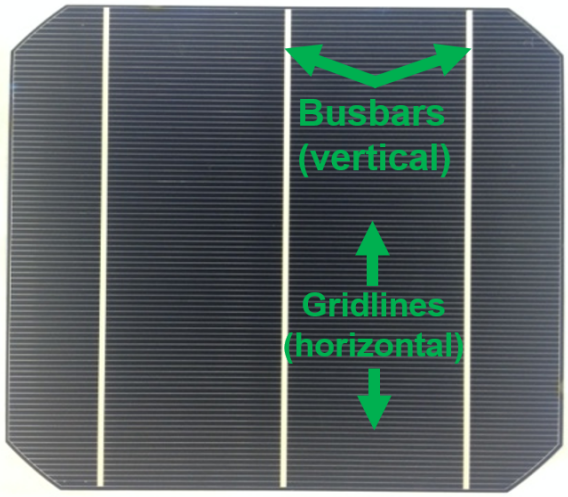

Figure 50: H-pattern: busbars and gridlines [33].

5.1.1 Analytical modeling and design of optimum grid pattern

We used an analytical model to find the optimized grid pattern (H-pattern) for our cells by quantifying the impact of series resistance, grid shadowing and metal-silicon contact recombination.

(1) Series resistance consists of five components: finger (gridline), busbar, contact, sheet and base resistivity as shown in Figure 51.

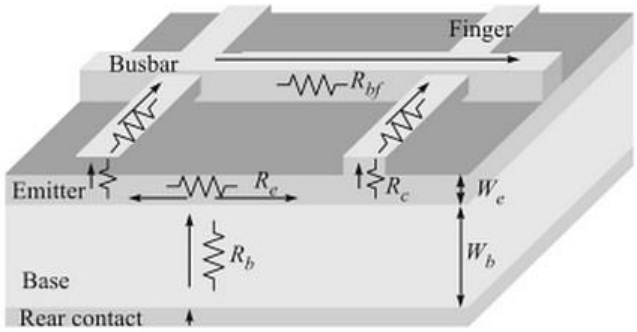

Figure 51: Series resistance components in a silicon solar cell [33].

In order to calculate each parasitic component for a given grid design, few four-point probe measurements are performed first on a finished device to measure BBR and r_{busbar} values as shown in Figure 52. Next the well established TLM measurement [32] is performed on a 1cm slice of the cell by keeping two probes fixed and moving the other two on successive gridlines. This gives a plot of resistance vs grid spacing from which $r_{contact}$ are extracted. Now all the series resistance components in a cell can be determined using following analytical expressions [32],

$$\begin{aligned}
R_{\text{busbar}} &= \frac{1}{3} * a * n^2 * b^2 \frac{2 * r_{\text{busbar}}}{l}, \\
R_{\text{finger}} &= \frac{1}{3} * a * b * n_{\text{gl}} * BBR, \\
R_{\text{contact}} &= r_{\text{contact}} * \frac{2 * b}{w}, \\
R_{\text{emitter}} &= \frac{1}{3} * b^2 * r_{\text{sheet}}, \\
R_{\text{substrate}} &= \rho * t, \\
R_{\text{total}} &= R_{\text{busbar}} + R_{\text{finger}} + R_{\text{contact}} + R_{\text{emitter}} + R_{\text{substrate}}
\end{aligned} \tag{22}$$

where a is the length of gridline in unit cell (Figure 28), b is a half gridline spacing, n is the number of gridlines per unit cell, n_{gl} is the number of gridlines in the whole solar cell, ρ is wafer resistivity, w is line width, and t is line thickness, BBR is busbar

to busbar resistance, r_{busbar} is the resistance between one edge to the other edge in one busbar, $r_{contact}$ and r_{sheet} are contact and sheet resistances [32].

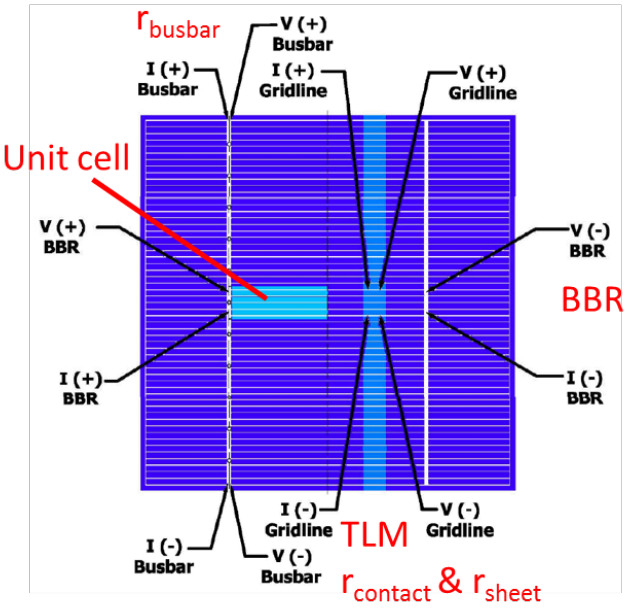

Figure 52: Front grid pattern showing placement of probes in a four-point measurement for determining series resistance components associated with BBR (busbar to busbar), busbar, contact resistance and emitter sheet resistance (gridline) [32].

First, four point probe measurement is to calculate finger resistance (R_{finger}) by measuring busbar to busbar resistance (BBR, measured from left busbar to right busbar). Second four point probe measurement, busbar, is to calculate R_{busbar} by measuring r_{busbar} by probing from one edge to the other edge in one busbar. Third four point probe measurement, gridline, is to calculate $R_{contact}$ and $R_{emitter}$ by measuring metal-Si contact ($r_{contact}$) and emitter sheet ($r_{emitter\ sheet}$) in 1cm wide cut cell (detailed information is described in the reference [32]). $R_{substrate}$ can be calculated by measuring resistivity of as-received wafer. Total series resistance is sum of all the resistances.

As shown in *Section 2.2*, the total series resistance affects the FF ($\propto$ efficiency) according to the following Equations (23),

$$
\begin{aligned}
FFs &= FF1(1 - r_{\mathrm{s}}), \quad r_{\mathrm{s}} = (\textbf{Total } \mathbf{R_s})/(\frac{V_{\mathrm{oc}}}{J_{\mathrm{sc}}}) \\
\textbf{FF} &= FFs[1 - \frac{(V_{\mathrm{oc}} + 0.7)FFs}{V_{\mathrm{oc}} * r_{\mathrm{sh}}}], \quad r_{\mathrm{sh}} = R_{\mathrm{shunt}}/\frac{V_{\mathrm{oc}}}{J_{\mathrm{sc}}}.
\end{aligned}
\tag{23}
$$

In other words, reducing series resistance increases FF and cell efficiency.

(2) Next, shadow loss, which primarily affects the short circuit current, is calculated from the metal coverage of the cell according to the following Equation:

$$
J_{\mathrm{sc}} = J_{\mathrm{sc,no\ metal\ shading}} * (1 - f_{\mathrm{metal\ fraction}}),
\tag{24}
$$

where $\mathrm{J_{sc}}$ is the actual short circuit current density ($\mathrm{mA/cm^2}$) of the cell, $\mathrm{J_{sc,no\ metal\ shading}}$ is short circuit current density ($\mathrm{mA/cm^2}$) without metal shading and $\mathrm{f_{metal\ shading}}$ is the fraction of metal coverage. Thus, $\mathrm{J_{sc}}$ decreases linearly with the increase in front metal coverage but the FF improves due to lower resistance. That is why optimization of the grid pattern is necessary to achieve the highest efficiency solar cell.

(3) In addition to series resistance and shading losses, we need to account for metal-Si contact recombination loss which increases with the metal-Si contact area. Metal-Si recombination increases total saturation current density and lowers open circuit voltage ($\mathrm{V_{oc}}$) according to the following Equations:

$$
\begin{aligned}
J_{\mathrm{o,total}} &= J_{\mathrm{oe}} + J_{\mathrm{ob}} \\
J_{\mathrm{oe}} &= J_{\mathrm{oe,\ field}} * (1 - f_{\mathrm{fm}}) + J_{\mathrm{oe,\ metal}} * f_{\mathrm{fm}} \\
J_{\mathrm{ob}} &= J_{\mathrm{ob,\ field}} * (1 - f_{\mathrm{bm}}) + J_{\mathrm{ob,\ metal}} * f_{\mathrm{bm}} + J_{\mathrm{ob,bulk}} \\
J_{\mathrm{ob,bulk}} &= \frac{q * {n_{\mathrm{i}}}^2 * w}{\tau * (N_{\mathrm{A}} + \Delta n)} \\
V_{\mathrm{oc}} &= \frac{kT}{q} ln(\frac{J_{\mathrm{sc}}}{J_{\mathrm{o,total}}} + 1)
\end{aligned}
\tag{25}
$$

where $\mathrm{J_{o,total}}$ is total saturation current density, $\mathrm{J_{oe}}$ is total emitter saturation current density, $\mathrm{J_{oe,\ field}}$ is for un-metallized area between the grid and $\mathrm{J_{oe,\ metal}}$ is for front metal-silicon contact area, $\mathrm{J_{ob}}$ is saturation current density associated with base,

$J_{ob,\ field}$ is for un-metallized back surface region and $J_{ob,\ metal}$ is for metallized back surface region, f_{fm} and f_{bm} are front and back metal-silicon contact fractions, q is elementary charge, n_i is intrinsic electron concentration, w is wafer thickness, N_A is base doping concentration, Δn is excess carrier density and k is boltzmann constant.

All three losses (series resistance, shading and metal-silicon contact recombination) are considered in grid modeling program, which calculates FF, J_{sc}, V_{oc} and cell efficiency for a given grid design. This allowed us to change the number of busbars to five and optimize the number of gridlines to achieve best cell efficiency. In order to run this program, a bseline PERC solar cell was first fabricated and characterized to extract all the relevant input parameters required for using the modeling program as shown in the next section.

5.1.2 PERC solar cell characterization

A typical baseline PERC solar cell (Figure 49) was fabricated with 89 grid lines and three busbars (Figure 50). We extracted the parameters listed in Table 4 and 5 from this three-busbar PERC solar cell. Table 4 shows series resistance and shading components extracted by four-point probe, 3D confocal microscope, and light IV measurements. Table 5 and Figure 53 show all the reverse saturation current components to account for recombination losses.

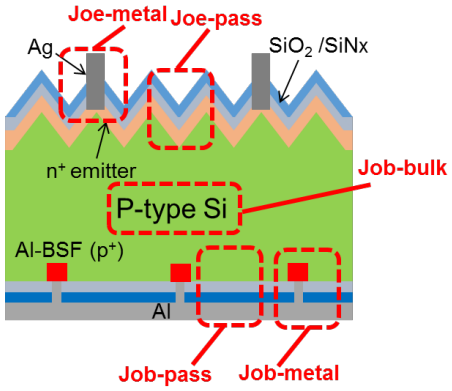

Figure 53: All reverse saturation current components in PERC: $J_{ob\text{-}pass}$, $J_{ob\text{-}met}$, $J_{ob\text{-}bulk}$, $J_{oe\text{-}pass}$ and $J_{oe\text{-}met}$.

Table 4: Metal Series Resistance and Metal Shading Components.

Parameter	Description	Value	Unit
nBB	Number of busbars	3	
n_{gl}	Total number grid lines	89	
l	Total length of grid line	15.6	cm
w	Grid line width	65	um
2w'	Width of front busbar on cell	1.5	mm
a	Length of gridline per unit cell	2.6	cm
b	Half gridline spacing	867	um
n	Gridlines per unit cell	6	
r_{busbar}	Busbar resistance	179	mOhm
r_{sheet}	Emitter sheet resistance	85	Ohm/sq
ρ	Wafer resistivity	1.5	Ohm-cm
tw	Wafer thickness	180	um
BBR	Busbar to busbar resistance	64	mOhm
J_{sc}	J_{sc} measured by IV tester	38.6	mA/cm^2

Table 5: Metal-silicon Contact Recombination Loss Components.

Parameter	Description	Value	Unit
$J_{ob\text{-}pass}$	J_o for passivated back surface	15	fA/cm^2
$J_{ob\text{-}met}$	J_o for back metal-silicon contact recombination	350	fA/cm^2
$J_{ob\text{-}bulk}$	J_o for bulk lifetime	70	fA/cm^2
$J_{oe\text{-}pass}$	J_o for passivated emitter surface	70	fA/cm^2
$J_{oe\text{-}met}$	J_o for front metal-silicon contact recombination	1000	fA/cm^2
f_{bm}	Back metal-silicon contact fraction	7.5	%
f_{fm}	Front metal-silicon contact fraction	6.6	%

$J_{ob\text{-}pass}$, $J_{ob\text{-}bulk}$, $J_{oe\text{-}pass}$ and $J_{oe\text{-}met}$ were measured by the quasi-steady-state photoconductance (QSSPC) technique using Sinton lifetime tool (WCT-120) [29] from symmetric test structures as shown in Figure 54.

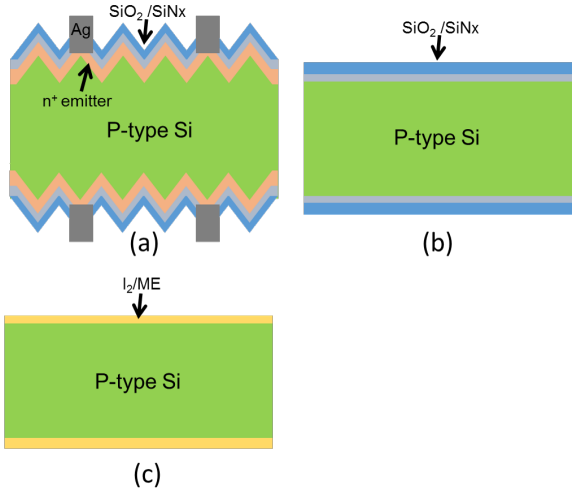

Figure 54: Symmetric test structures for (a) J_{oe} (b) SRV and J_{ob}' and (c) bulk lifetime.

$J_{oe\text{-}pass}$ and $J_{oe\text{-}met}$ were determined by the slope of inverse lifetime vs metal fraction obtained from QSSPC measurements on symmetric samples (Figure 54a) with different metal dot coverage ranging from 0 to 10% extrapolation of the linear plot gives $J_{oe\text{-}met}$ when metal fraction is 100% and $J_{oe\text{-}pass}$ when metal fraction is 0% as explained in Chapter 2. $J_{ob,bulk}$ is calculated by the following Equation after measuring bulk lifetime (τ_b) on a bare Si wafer passivated with I2/Me solution (Figure 54c),

$$J_{ob,bulk} = \frac{q * {n_i}^2 * w}{\tau_b * (N_A + \Delta n)} \tag{26}$$

where τ_b is measured bulk lifetime from the test structure in Figure 54c, q is elementary charge, n_i is intrinsic electron concentration, w is wafer thickness, N_A is base doping concentration, Δn is excess carrier density and k is boltzmann constant.

$J_{ob\text{-}pass}$ is calculated by using the following Equation (27), after measuring effective

bulk lifetime of a symmetric test structure shown in Figure 54b by QSSPC measurements. Surface recombination velocity from τ_{eff} and τ_{b} values. ($1/\tau_{\text{eff}}=1/\tau_{\text{b}}+2\text{S/W}$).

$$J_{\text{ob-pass}} = \frac{q{n_{\text{i}}}^2 Dn}{N_{\text{A}} Ln} * \frac{S\cosh(W/Ln) + (Dn/Ln)\sinh(W/Ln)}{(Dn/Ln)\cosh(W/Ln) + S\sinh(W/Ln)}, \tag{27}$$

where S is measured surface recombination velocity, q is elementary charge, n_{i} is intrinsic electron concentration, W is wafer thickness, N_{A} is base doping concentration, Dn is electron diffusion coefficient and Ln is electron diffusion length. $J_{\text{ob-met}}$ is determined by Sentaurus 2D device modeling, using Al-BSF profile (3um deep and 5e18 cm^{-3} concentration with step function). Sentaurus model gives a plot of J_{o} vs SRV for a given profile from which $J_{\text{ob-met}}$ is read at S value of 1e7 cm/s which corresponds to metal-Si recombination velocity.

5.1.3 Results of gridline optimization

Once all the necessary input parameters are extracted (Table 4 and 5), grid modeling was performed. First we varied the number of gridlines from 40 to 170 for our three-busbar cells. Table 6 shows that this reduces series resistance from 2.24 to 0.35 and raises FF from 71.8 to 81%.

Table 6: Gridline Modeling Results: Impact of Series Resistance on FF.

# of gridlines	Finger spacing (mm)	Busbar (Ω-cm^2)	Fingers (Ω-cm^2)	Contact (Ω-cm^2)	Emitter (Ω-cm^2)	Substrate (Ω-cm^2)	Total Rs (Ω-cm^2)	FF [%]
40	3.9	0.0267	0.95	0.18	1.05	0.03	2.24	71.8
60	2.6	0.0118	0.63	0.12	0.47	0.03	1.26	76.6
70	2.2	0.0087	0.54	0.10	0.34	0.03	1.03	77.8
80	1.9	0.0067	0.48	0.09	0.26	0.03	0.86	78.5
90	1.7	0.0053	0.42	0.08	0.21	0.03	0.74	79.1
100	1.5	0.0043	0.38	0.07	0.17	0.03	0.65	79.6
110	1.4	0.0035	0.35	0.07	0.14	0.03	0.58	79.9
120	1.3	0.0030	0.32	0.06	0.12	0.03	0.52	80.2
130	1.2	0.0025	0.29	0.06	0.10	0.03	0.48	80.4
170	0.9	0.0015	0.22	0.04	0.06	0.03	0.35	81.0

Next, Equation (24) was used as part of the modeling program to calculate the

impact of shading loss on J_{sc}. As expected, Table 7 show that as the number of gridlines increases, from 40 to 170, J_{sc} decreases from 39.4 to 37.3 mA/cm^2 because of the increased shading.

Table 7: Gridline Modeling Results: Shading Impact on J_{sc}.

# of gridlines	$J_{sc,no\ metal\ shading}$ (mA/cm^2)	front metal converage (f_{fm})	J_{sc} (mA/cm^2)
40	41.4	4.6%	39.4
60	41.4	5.4%	39.1
70	41.4	5.8%	38.9
80	41.4	6.2%	38.7
90	41.4	6.6%	38.6
100	41.4	7.1%	38.4
110	41.4	7.5%	38.3
120	41.4	7.9%	38.1
130	41.4	8.3%	37.9
170	41.4	10.0%	37.3

Third, Equation (25) was incorporated in the model to calculate the impact of metal-silicon contact recombination on V_{oc}. Table 8 shows that as the number of gridlines increases, V_{oc} decreases, because increase in front metal-silicon contact area increases metal-silicon recombination loss.

Finally, cell efficiency was calculated in the model from V_{oc}, J_{sc} and FF (Efficiency = V_{oc}*J_{sc}*FF). Table 9 shows that the optimum number of gridlines is ∼100 lines for three busbars on our cells, which can give the highest efficiency of 20.25%.

Next, we varied the number of busbars as well as gridlines to perform similar calculations to see what combination of busbars and gridlines can give the highest efficiency for our cells. In these calculations, we reduced the busbar width when we increased the number of busbars to keep the busbar shading constant. Figure 55 shows the output of this modeling effort, which indicates that for a fixed number of gridlines increasing the number of busbars increases efficiency but efficiency gain tend to saturate beyond five busbars. It also shows that 90 gridlines gave the highest

Table 8: Gridline Modeling Results: Metal-silicon Contact Recombination Loss Impact on V_{oc}.

Job-pass,100% (fA/cm2)	Job-met, 100% (fA/cm2)	Job-bulk, 100% (fA/cm2)	Joe-pass, 100% (fA/cm2)	Joe-metal, 100% (fA/cm2)
15	**350**	**70**	**70**	**1000**
# of gridlines	ffm (%)	fbm (%)	Total Jo (fA/cm2)	V_{oc} (mV)
40	4.6	7.5	224	665
60	5.4	7.5	232	664
70	5.8	7.5	236	664
80	6.2	7.5	240	663
90	6.6	7.5	244	663
100	7.1	7.5	247	662
110	7.5	7.5	251	662
120	7.9	7.5	255	661
130	8.3	7.5	259	661
170	10.0	7.5	275	659

Table 9: Gridline Modeling Results: The Number of Gridline Impact on Solar Cell Efficiency.

# of gridlines	FF [%]	J_{sc} (mA/cm^2)	V_{oc} (mV)	Efficiency (%)
40	71.8	39.4	665	18.82
60	76.6	39.1	664	19.88
70	77.8	38.9	664	20.08
80	78.5	38.7	663	20.19
90	79.1	38.6	663	20.24
100	79.6	38.4	662	20.25
110	79.9	38.3	662	20.23
120	80.2	38.1	661	20.20
130	80.4	37.9	661	20.16
170	81.0	37.3	659	19.89

efficiency of ∼20.5% for five busbars. The reason for choosing five busbars is that at this point busbar width becomes 0.9mm as opposed to 1.5mm for three busbars case, which is reaching the limit of soldering tabs to busbars when interconnecting cells to make modules. Reducing busbar width further can rsult in peeling of busbars during tabbing.

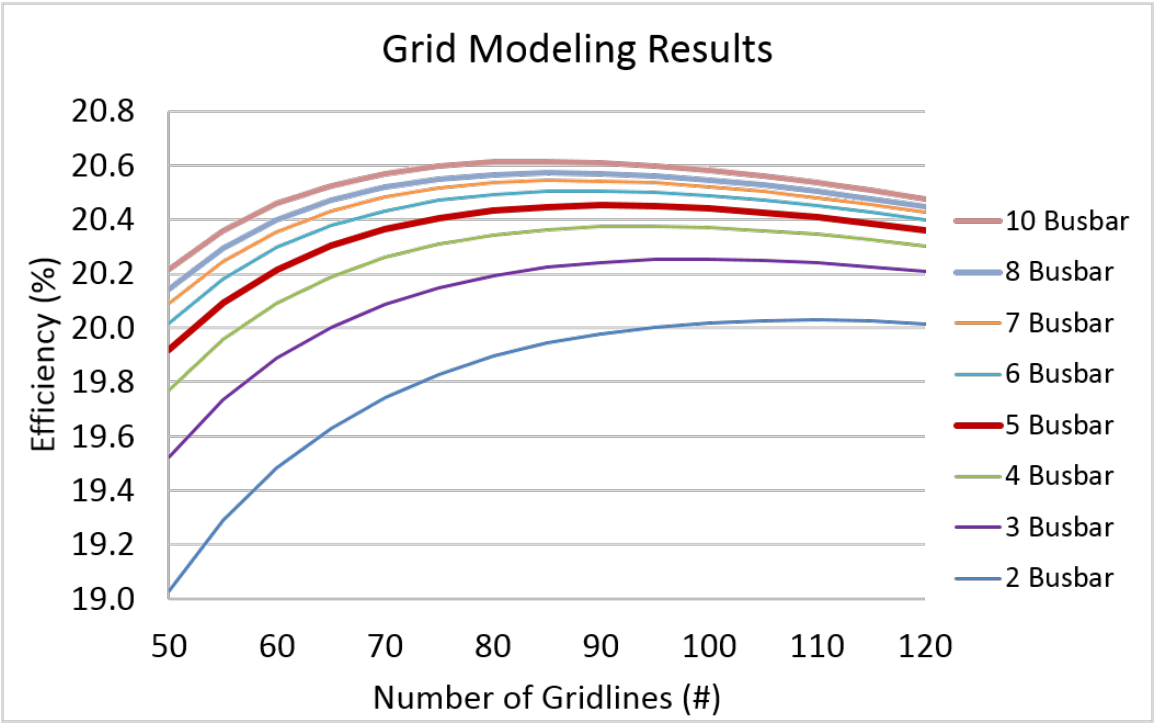

Figure 55: Front gridline modeling results as a function of the number of gridlines and busbars.

5.1.4 Implementation of five-busbar technology on PERC cell

After establishing the grid design for our PERC cell with five busbars, we implemented this design on the cell using screen printing technology (Figure 56).

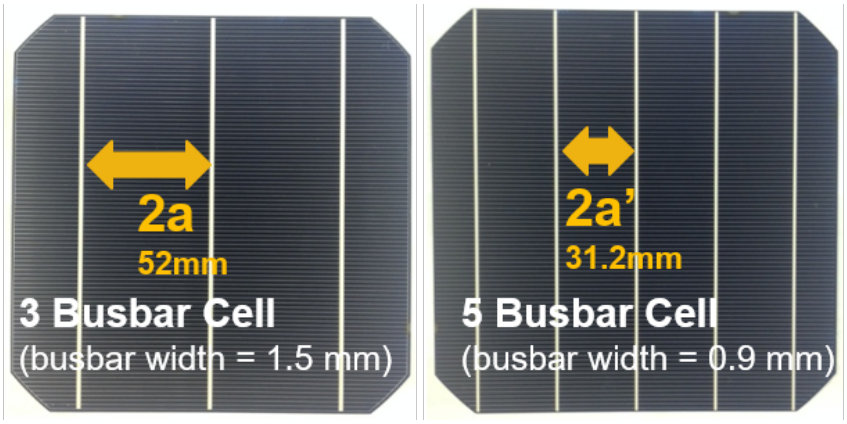

Figure 56: Picture of PERC solar cells with 3 busbars and 5 busbars.

Figure 57 shows the measured and calculated values of all the five resistive components for the three busbars and five busbars with 89 gridlines. Note that, for three

busbars, total series resistance was ~0.7 ohm-cm^2 with grid resistance alone accouting for 0.4 ohm-cm^2. Our grid modeling (Figure 57) showed that implementing the 5 busbar technology can lower the gridline resistance from 0.40 Ω-cm^2 to 0.24 Ω-cm^2, increase FF from 78.9 to 80% and increase solar cell efficiency by 0.3%.

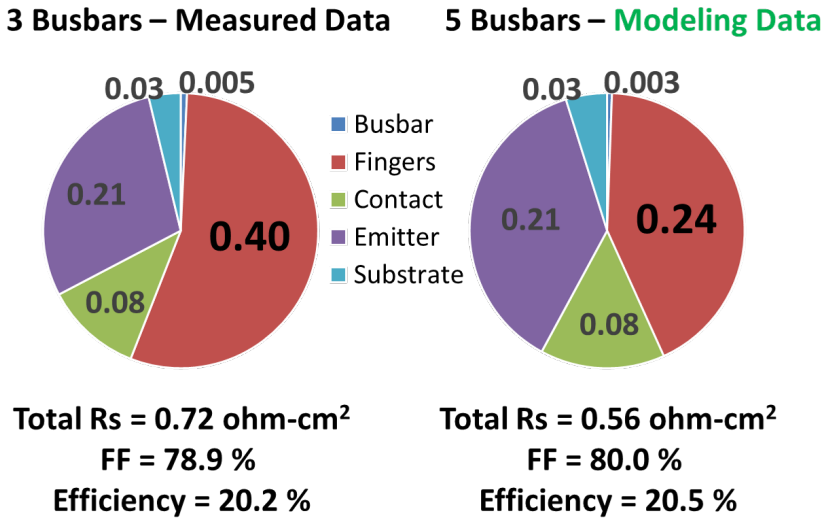

Figure 57: Analysis of the individual series resistance components in the 3-busbar and 5-busbar PERC solar cell.

To validate this model, next we fabricated the screen printed PERC cells with five busbars and 89 gridlines and performed detailed charaterization. We found that total series resistance of five-busbar PERC solar cell decreased to ~0.53 ohm-cm^2 (Table 10) compared to 0.72 ohm-cm^2 for the three-busbar PERC cell. This raised the FF from 78.9% to 79.9%, resulting in enhanced solar cell efficiency from 20.2% to 20.5%. Note that V_{oc} and J_{sc} values were essentially same because we decreased the busbar width from 1.5mm for three busbar cells to 0.9mm for five-busbar cells.

Table 10: Measured LIV Data on a PERC Solar Cell With 3 Busbars and 5 Busbars.

Busbar type (# of AVG)	V_{oc} (mV)	J_{sc} (mA/cm^2)	FF(%)	Efficiency (%)	R_{series}
3 busbars (8)	663	38.6	78.9	20.2±0.06	0.72
5 busbars (5)	664	38.7	79.8	20.5±0.08	0.53

5.2 Development of Fine Gridline Technology

Screen printing narrower or fine gridline has become an active area of investigation because it can reduce shadowing and the amount of Ag paste, increasing efficiency and reducing cost simultaneously. Screen printing technology has come a long way in the last decade. Line widths have decreased from ≥100um in five years ago to 60um today and attempts are being made to lower it below 40um. Therefore, in addition to implementing five-busbar technology, we also attempted to develop fine line printing by altering screen design parameters, paste and printing parameters. Screen design parameters including the number of mesh wires and mesh wire thickness (Figure 58) were altered in this study to achieve finer lines.

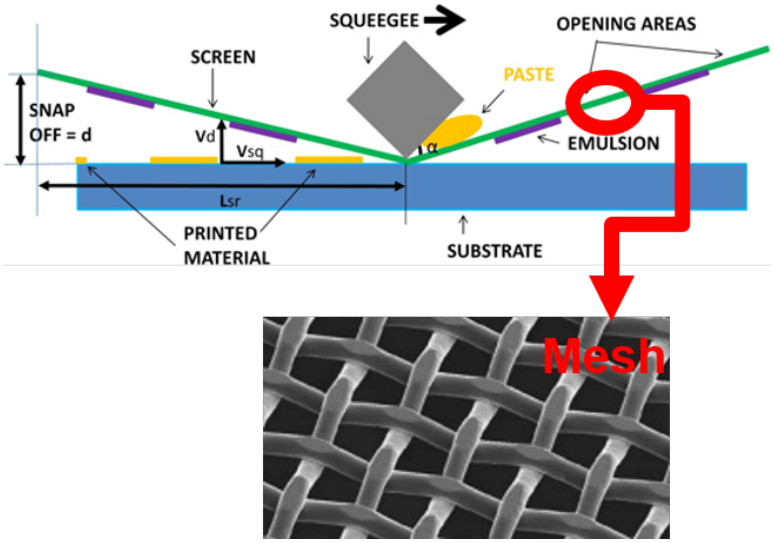

Figure 58: Picture of mesh and elements involved in the screen printing mechanism.

Gridlines of 50um width were achieved as opposed to ≥65um (Figure 59) by increasing the number of mesh wires from 360 to 650 (per inch) with slightly thinner mesh wires (14um vs 15um). This reduced the shading from 6.6% to 5.6% (Table 11).

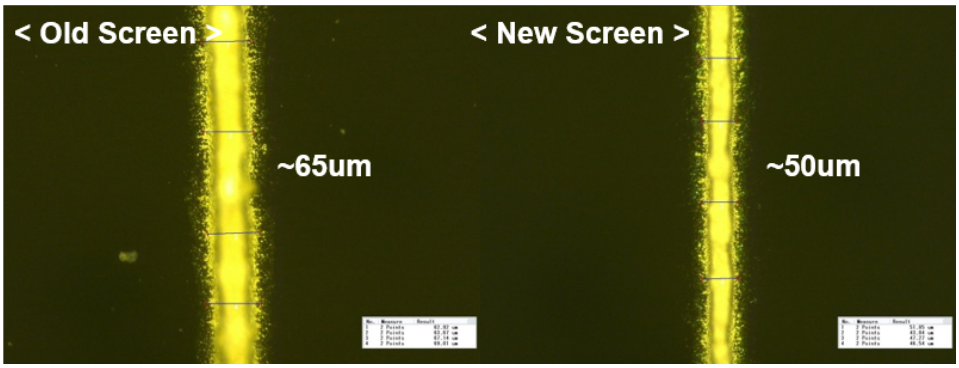

Figure 59: Picture of gridlines after screen printing with old and new screens.

Table 11: Comparison of Old and New Screen Designs.

Screen type	Mesh count (wires/inch)	Mesh wire thickness(um)	Measured gridline width(um)	Total front metal shading (%)
Old design	360	15	65	**6.6**
New design	650	14	50	**5.6**

Next, complete PERC cells were fabricated with five busbars with 50um wide 89 gridlines. Results are summarized in Table 11. The 1% reduction in shading loss from 6.6% to 5.6% increased J_{sc} by 0.2mA/cm^2 and raised the cell efficiency by 0.1% absolute as shown in Table 12. As a result, PERC solar cell efficiency increased by 0.1%.

Table 12: Measured IV Data on a PERC Solar Cell With Old and New Screen Printing.

Screen type (width, # of AVG)	V_{oc} (mV)	J_{sc} (mA/cm^2)	FF(%)	Efficiency (%)	R_{series}
Old screen (65um, 5)	664	38.7	79.8	20.5±0.08	0.53
New screen (50um, 5)	665	38.9	79.8	20.6±0.08	0.55

Thus, these two technology enhancements raised the PERC cell efficiency from 20.2% to 20.6%.

5.3 Conclusion

In this chapter, we developed two advanced screen printing technologies, five busbars and fine grid lines, to increase PERC solar cell efficiency. In order to achieve these technologies, gridline modeling was used to design grid patterns to optimize the trade-off among resistive, shadow and metal-Si recombination losses to predict cell efficiency using an analytical grid design model. Modeling showed that increasing number of busbars increases efficiency if the nusbar shading is kept constant. However, after five busbars improvement slows down. In addition increasing number of busbars beyond five will make busbars too thin to solder the tasks for module assembly. Thus five busbars seems optimum for performance and cost. Five busbars with 89 gridlines, instead of widely used three busbars, increased cell efficiency from 20.2% to 20.5% due to reduced series resistance from 0.72 to 0.53 ohm-cm^2. Secondly, fine gridline printing was developed by changing screen design, silver paste and screen parameters (# of mesh and wire diameter) to reduce gridline width. The optimized fine gridline printing reduced gridline width from ∼65um to ∼50um and increased cell efficiency from 20.5% to 20.6% due to reduced shading loss from 6.6% to 5.6%.

CHAPTER VI

TASK 3: FIELD-EFFECT PASSIVATION BY CHARGE INJECTION INTO SILICON NITRIDE USING A NOVEL LOW-COST PLASMA CHARGING METHOD

Dielectric surface passivation quality is becoming more important in order to reduce loss mechanisms in solar cells. For example, currently full Al-BSF solar cells are being replaced by local Al-BSF contact cells, known as passivated emitter rear contact cells (PERC). PERC cell reduces back metal contact fraction from 100% to ∼6% and increases efficiency by ∼1% over full Al-BSF cell due to better rear passivation and reflection. Also, an n-type passivated emitter rear totally diffused (PERT) solar cells ($p^+/n/n^+$) utilize local contacts to fully diffuse n^+ back surface through a dielectric for higher efficiency. The impact of dielectric passivation quality is becoming more critical, because metal-Si contact recombination is greatly reduced by reduced metal-Si contact fraction.

PECVD (Plasma-Enhanced Chemical Vapor Deposition) SiNx (Slicon-Nitride) film has been widely used in crystalline silicon solar cells for anti-reflective coating on the front as well as for surface passivation on front and back. It is known that PECVD SiNx contains significant positive fixed charge and thus provides a good field-effect passivation on n-type silicon surface (n+ emitter or n-type wafer) [74, 75] by bending the bands that cause accumulation of electrons near the silicon surface. This reduces SRH recombination at the surface and keeps minority carriers away from the surface to prevent any shunting. However, the positive charge in SiNx film is not effective in passivating for p-type silicon surfaces such as boron-doped emitter on n-type PERT cells and back surface of p-type PERC cells. This is because positive charge induced

depletion layer causes more suface recombination because of n≃p while inversion layer brings lots of minority carriers to the surface which may trigger leakage current or flow of minority carriers to to the metal contacts [76]. Therefore, an aluminum oxide (Al_2O_3) film containing negative fixed charge is frequently used below the SiNx film to create accumulation and provide excellent passivation for p-type surfaces [77]. However, there are two main disadvantages of this widely used Al_2O_3 technology that uses TMA precursor: high operation cost and safety. Another known option for field-effect passivation for p-type is corona discharge by ionization of the air, but it requires very high voltage in the range of a few KV or higher and has challenges associated with charge stability, cell damage and electrode corrosion by radical oxygen and water molecules [78]. Therefore, in this task, we implemented a novel high throughput plasma charging technique for field-effect passivation of boron emitter in n-type PERT and p-type back surface of PERC solar cells. Sentaurus device modeling was used to assess the impact of controlled charge injection on emitter saturation current density (J_{oe}) of SiO_2/SiNx passivated boron doped surfaces. Finally, complete large area n and p-type cells were fabricated with oxide nitride passivation, with and without the charge injection, to validate the predicted cell performance enhancement.

6.1 Operation of a Novel Plasma Charging Tool

In this study, a novel low-cost plasma charging method (Patent, US 8,338,211 B2) developed by Amtech was used for controlled charging of SiO_2/SiNx dielectric stacks. A schematic diagram of this method and tool is shown in Figure 60.

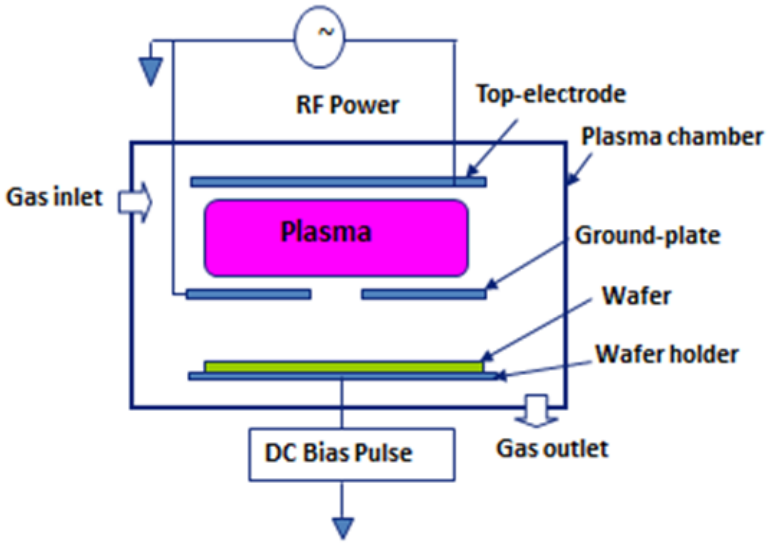

Figure 60: Schematic picture of plasma charging prototype tool.

RF power induces nitrogen plasma by ionizing N_2 gas according to the following Equation (28),

$$N_2 + e^* \longrightarrow {N_2}^+ + 2e^-, \tag{28}$$

where e* refers to accelerated electron which has much higher energy than its ground state. A DC bias pulse (∼100V), applied to the cell carrier plate in a plasma chamber (typically nitrogen plasma), extracts charges from the plasma, consisting of negatively charged electrons and positively charged nitrogen ions in nitrogen plasma, and injects them into a passivating dielectric film (SiNx) exposed to the plasma. Positive or negative charge is selectively introduced depending on the pulse polarity: positive charge with negative bias pulse or negative charge with positive bias pulse. Figure 61 shows band diagrams of PECVD grown SiNx and thermally grown SiO_2 dielectric stacks on silicon and its negative charge injection process. As shown in Figure 61b, electrons from nitrogen plasma are injected into SiNx and are accumulated into SiNx traps in the bulk and SiNx/SiO_2 interface due to band bending from DC bias in the cell carreir plate.

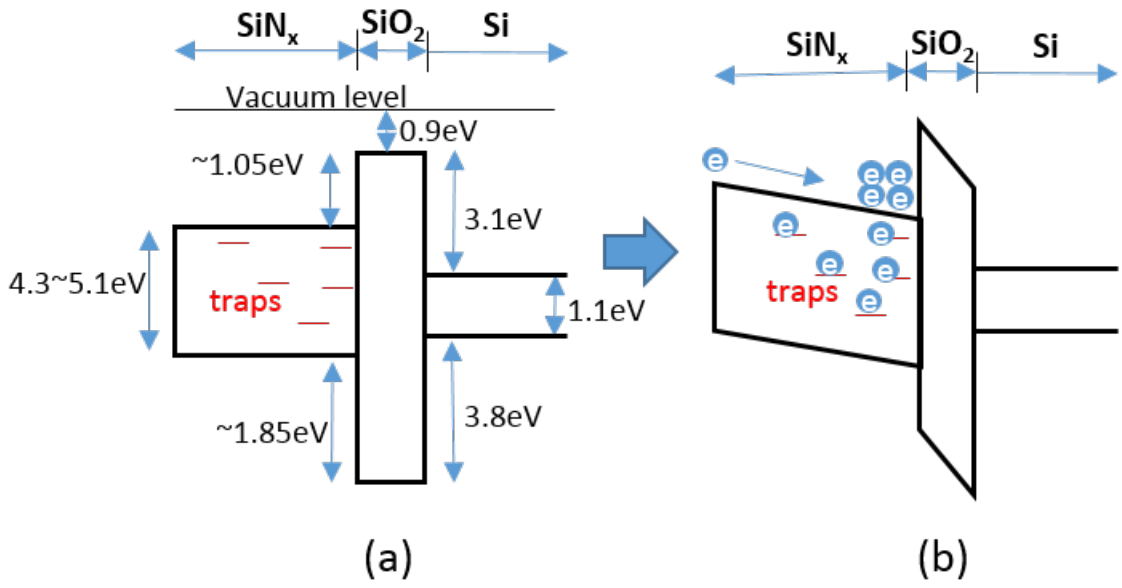

Figure 61: Band diagrams of (a) PECVD grown SiNx and thermally grown SiO_2 dielectric stacks on silicon and (b) negative charge injection.

In this chapter, we will study the positive impact of negative charge injection on field effect passivation of boron emitter surface in n-type PERT cells as well as rear boron-doped surface of the p-type PERC cells.

6.2 CV Measurements to Establish and Quantify the Charge Injection by the Tool

Symmetric test structure shown in Figure 62 were fabricated to measure C-V curve to validate the operation of the charging tool. Mercury probe C-V measurement tool has been used to measure C-V curve in this experiment which avoids the need for making metal contacts to form MOS capacitor. This test structure has thermally grown SiO_2 (8nm) and PECVD grown SiNx (200nm) on front and back surface which is similar to what will be used on the back side of p-type PERC cells fabricated in this research.

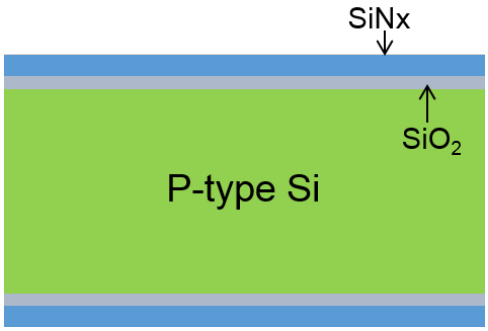

Figure 62: Test structure for C-V and effective lifetime measurements (thermally grown SiO_2(inner):8nm and PECVD grown SiNx(outer): 200nm).

Figure 63 shows the measured C-V curves for five different points (top, center, left, right and bottom of the test structure) before and after charge injection on the symmetric test structure in Figure 62.

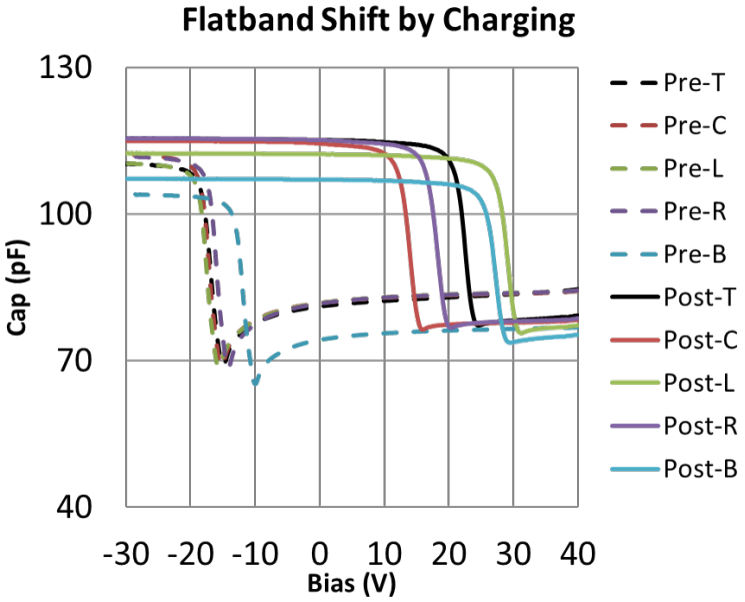

Figure 63: Measured C-V curves by mercury-probe before and after charge injection (Pre-: pre-charging, Post-:post charging, T:top, C:center, L:left, R:right and B:bottom region of the test wafer).

First of all, notice that the CV curves before charging show big negative flat-band voltages (Vfb) around -15V which is caused by initial positive fixed charges in the oxide and the nitride layer. After charging, the CV curves for the five sites show huge flat-band voltage shifts in the positive direction with Vfb of +21V or net shifts by more than +38V. This shift is due to the negative charge injection in the SiNx dielectric (Figure 61b) by the plasma charge injection tool with positive bias on the sample plate. From these C-V curves, initial charge amount, injected charge amount by charge injection and net charge amounts after charge injection were calculated as shown in Table 13. Charge in the flatband voltage and accumulation capacitance (Cox) can be used to calculate the injected charge $\Delta Q = Cox^{*}\Delta V_{FB}$. Figure 63 and Table 13 also show that the test structure switched from depletion/inversion mode to accumulation mode, which should reduce surface recombination velocity and shunt mechanisms. This is because when there is asymmetric carrier concentrations of holes and electrons at the surface (like in accumulation or inversion) SRH recombination at the surface defects is reduced. SRH recombination is maximum when n_s=p_s (assuming σ_n= σ_p) . Inversion can reduce recombination but it attracts minority carriers to the surface and cause leakage path through metal contacts. Table 13 shows that net negative charge of -1E13 cm^{-2} can be achieved, which is high enough for field-effect passivation.

Table 13: Calculated Charge Amount from Measured C-V Data in Figure 63

	Top	Center	Left	Right	Bottom	Avg	Unit
Vfb,init	-17.7	-19.4	-18.2	-16.7	-12.6	-16.9	V
Vfb,post	21.7	13.0	28.2	17.2	26.4	21.3	V
Vfb,shift	39.4	32.4	46.4	33.9	39	38.2	V
Qinit	3.7E+12	4.0E+12	3.8E+12	3.5E+12	2.6E+12	3.5E+12	cm-2
Qinjected	-1.6E+13	-1.3E+13	-1.9E+13	-1.4E+13	-1.6E+13	-1.6E+13	cm-2
Qnet	-1.3E+13	-9.4E+12	-1.5E+13	-1.1E+13	-1.4E+13	-1.2E+13	cm-2

Vfb,init,Vfb,post and Vfb,shift are initial, post charging and shifted flatband voltage, respectively. Qinit, Qinjected and Qnet are initial, injected and net charge amounts, respectively.

A closer look at the C-V curves (Figure 63) reveals that accumulation capacitance value increased slightly after charge injection. A possible explanation is that the exposed SiNx dielectric is slightly etched away by plasma, which increases accumulation capacitance value. Moreover, C-V curves in the transition region after charge injection shows slightly more stretched-out pattern compared to initial C-V curves. This stretch-out in the post-charging CV curves is caused by increased density of insterface state (D_{it}). This damage generation at Si-SiO_2 interface could be from Fowler-Nordheim (FN) tunneling in plasma charging as shown in Figure 64.

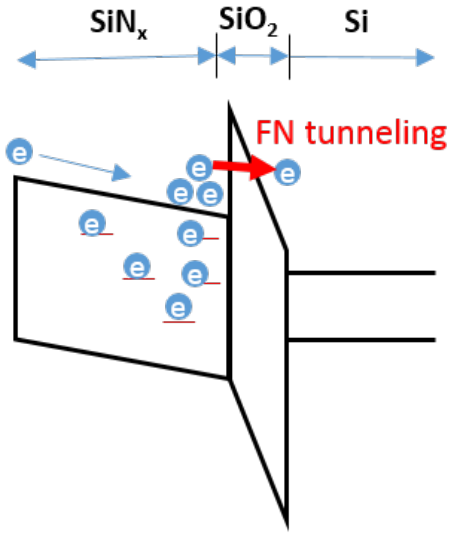

Figure 64: Band diagram of Fowler Nordheim (FN) tunneling effect.

Since most of the injected charges are accumulated at the SiNx/SiO_2 interface, some of them tunnel through the thin oxide by a strong electric field resulting from a high density charge accumulted at the interface. This excessive FN tunneling can cause some damage generation at Si-SiO_2 because tunnel electrons becomes hot electrons with an energy of 3.1eV or higher right at the silicon surface which is high enough to give an bonding damage (distortion or breakage). The derivative plots (dC/dV) of the CV curves (Figure 65) show more clear difference between pre- and post-charging cases. Higher derivative value means a better interface quality. Thus, the peak derivative values for the post-charging CV curves are smaller than those

for the pre-charging, meaning more CV stretch-out and worse interface quality after charge injection.

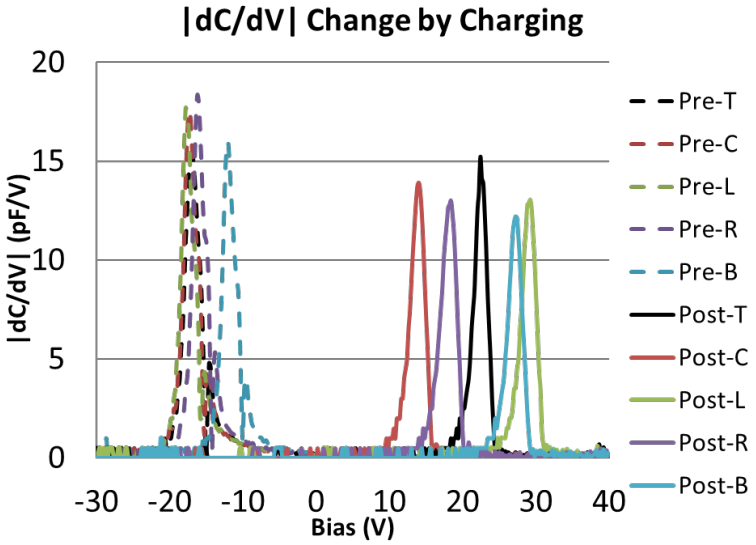

Figure 65: Calculated dC/dV as a function of voltage (Pre-: pre-charging, Post-:post charging, T:top, C:center, L:left, R:right and B:bottom region of the test wafer).

6.3 Fundamental Understanding and Analysis of the Impact of Charge Injection on N-type PERT and P-type PERC Solar Cells.

In this study, large area (239 cm^2) bifacial n-type PERT cells and p-type PERC cells were fabricated as shown in Figure 66 with SiO_2/SiNx stacks on both surfaces for dielectric passivation.

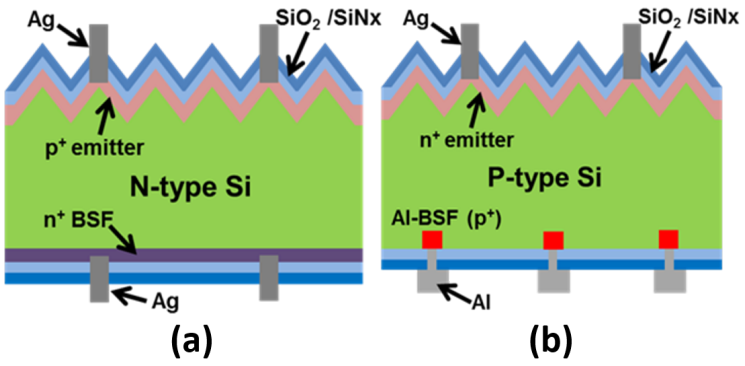

Figure 66: Schematic picture of (a) bifacial n-type PERT and (b) bifacial p-type PERC solar cells.

Then, the novel plasma tool, invented by Amtech, was applied at Amtech to inject negative charge into the SiO_2/SiNx passivated front surface of n-type PERT cells and back surface of p-type PERC to improve surface passivation and increase cell efficiency. In the case of n-type PERT, depletion layer in the p+ emitter, induced by initial positive charge in the SiO_2/SiNx dielectric stack, is transformed into accumulation layer, reducing SRH surface recombination. In the p-type PERC cells, negative charge injection transforms the inversion layer, induced by positive charge in the dielectric stack, to accumulation layer, reducing shunt mechanisms between metal and silicon. Note that in the case of PERC, there may be an inversion layer before charging due to modest base doping ($\sim 10^{16} cm^{-3}$). This helps in passivation but hurts parasitic shunting or leakage of minority carriers in the inversion layer, which generally lowers the FF and cell efficiency.

6.3.1 Comparison of boron emitter passivation by negative charge injection into SiO_2/SiNx stack and Al_2O_3/SiNx stack

First, a symmetric test structure (Figure 67) for emitter saturation current density (J_{oe}) was fabricated to compare performance of field effect passivation between negative charge injected SiO_2/SiNx and Al_2O_3/SiNx, since Al_2O_3/SiNx is a well known passivation method containing a negative fixed charge (-5e12$\sim$-1e13 cm^{-2}).

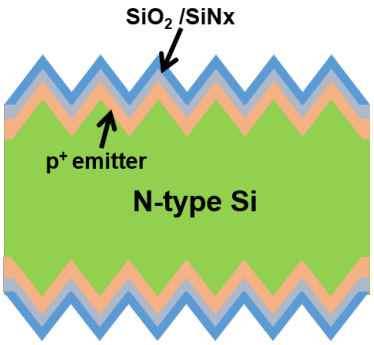

Figure 67: Symmetric test structure for emitter saturation current density(J_{oe}) of n-type PERT cell.

Figure 68 shows the measured J_{oe} values on the symmetric test structure in Figure 67 before and after -7.9e12cm^{-2} negative charge injection. As expected from the modeling, Joe decreased from ~80fA/cm^2 to ~50fA/cm^2 for SiO_2/SiNx passivated boron emitter and became comparable to the Al_2O_3 (Plasma ALD Al_2O_3)/SiNx passivated boron emitter.

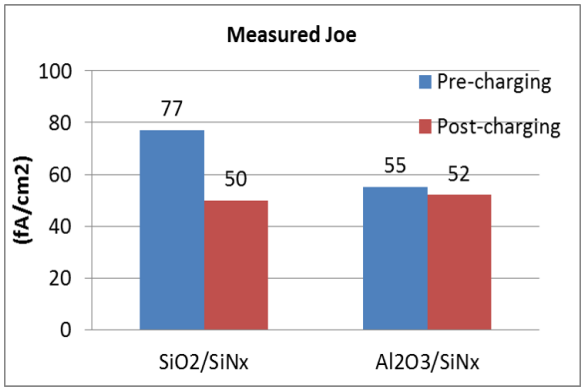

Figure 68: Measured Joe of a 85ohm/sq boron emitter on n-type wafer before and after negative charge injection(-7.9e12cm^{-2}) in the test structure shown in Figure 67.

Since Al_2O_3 is known to have -5e12~-1e13 cm^{-2} negative fixed charge, these results demonstrate that charged SiO_2/SiNx stack using this method is just as effective as Al_2O_3/SiNx stack as far as field induced passivation is concerned. Thus, this tool can substitute for Al_2O_3 deposition system.

6.3.2 Study of field effect passivation by negative charging of n-type PERT solar cells

Complete large area screen printed n-type bifacial PERT solar cells were fabricated (Figure 69) and analyzed before and after charge injection.

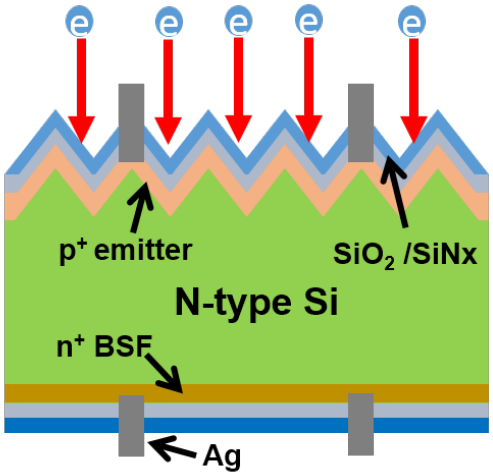

Figure 69: Schematic of negative charging on front surface of n-type bifacial PERT solar cells.

Table 14 shows the average LIV cell data for four of n-type bifacial PERT cells before and after negative charge injection.

Table 14: Measured N-type PERT Cell LIV Data Before and After Negative Charging on Front SiO_2/SiNx Stack (-1E13cm^{-2})

Wafer Type	AVG of 4	V_{oc} (mV)	J_{sc} (mA/cm^2)	FF(%)	Efficiency (%)
N-type PERT Cell	Pre-charging	636	37.9	79.0	19.0 ±0.15
	Post-charging	648	39.5	79.5	20.35 ±0.13

In case of n-type PERT cells, absolute cell efficiency increased by 1.35% after -1E13 cm^{-2} negative charge injection in SiO_2/SiNx stack. Note that the efficiency boost comes from all cell parameters including ΔV_{oc} (12mV), ΔJ_{sc} (1.6mA/cm^2) and ΔFF (0.5%) due to enhanced front surface passivation. This is because boron emitter surface state (heavy boron emitter doping, ~4.8e19cm^{-3}) is changed from depletion

(with net positive charge in SiO_2/SiNx) to accumulation (with net negative charge in SiO_2/SiNx). This is supported by changes of electron and hole concentration at the surface. In order to validate this hypothesis further, detailed device modeling was performed using Sentaurus modeling to extract electron and hole concentrations at the surface as a function of positive and negative charge as the surface (Figure 70). Since the boron surface concentration (p_s) of the emitter is ~4e19cm^{-3}, the pre-charging state is in depletion because at ≥5e12cm^{-3} positive charge hole concentration is ≤1e18cm^{-3} or less than p_s

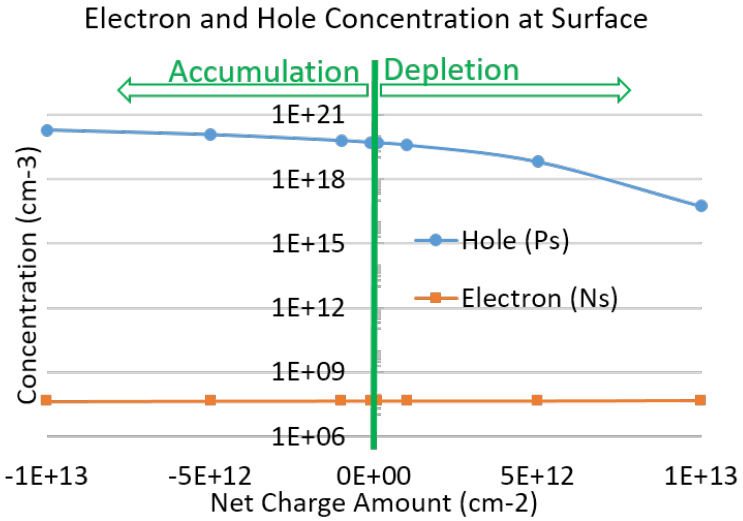

Figure 70: Electron and hole concentration at the surface of a boron-doped emitter with n_s, 4.8e19cm^{-3} as a function of surface charge density extracted by Sentaurus modeling.

However, Figure 70 shows that when net charge amount in the dielectric stack changes from strong positive (1E13cm^{-3}) to strong negative (-1E13cm^{-3}) by charge injection, hole concentration at the surface increases to ≥ 1e20cm^{-3} which is much higher than n_s or heavily boron-doped emitter surface (4.8e19cm^{-3}). This leads to accumulation with reduced recombination at the surface which should increase both V_{oc} and J_{sc}. This was validated by internal quantum efficiency (IQE) measurements in Figure 71 which clearly show that short wavelength responses (400nm~800nm) increased appreciably after negative charge injection in SiO_2/SiNx stack. This also

supports that front surface passivation was improved by field effect passivation.

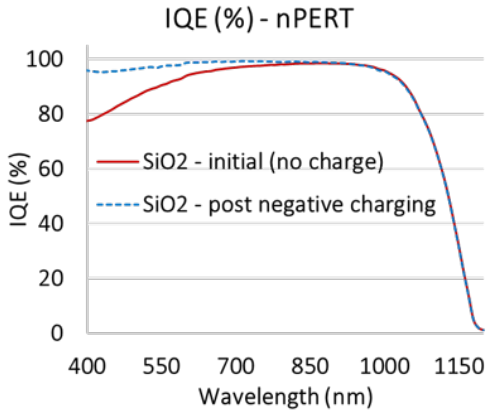

Figure 71: Measured Internal Quantum Efficiency (IQE) on n-type PERT solar cell before and after charge injection.

Suns-Voc is another popular measurement to gauge the overall recombination in finished a solar cell. It gives effective lifetime in a finished cell which is indicative of both bulk and surfaces. Suns-Voc measurements in Figure 72 also showed that effective lifetime increased after charge injection at all the injection levels supporting the merit of using this technique for solar cells.

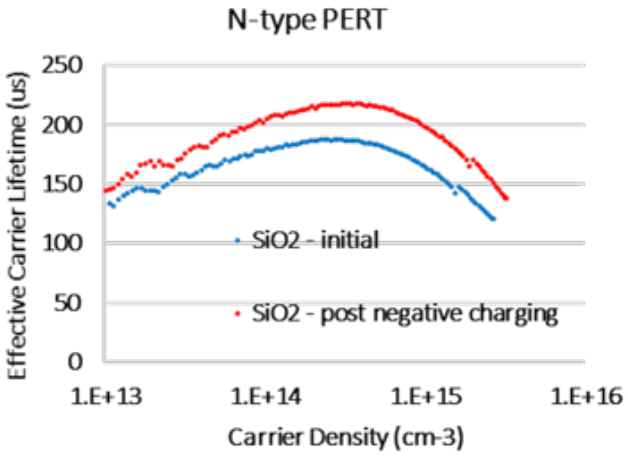

Figure 72: Measured effective lifetimes before and after negative charge injection (net charge: -1e13 cm^{-2}) as a function of injection level on n-type PERT cell by Sinton Suns-Voc tool.

6.3.3 Study of field effect passivation by negative charging on p-type PERC solar cells

Next, the impact of negative charge injection on the rear passivating dielectrics was investigated. Bifacial PERC cells were fabricated (Figure 73) with average efficiency of 19.95% before charging (Table 15).

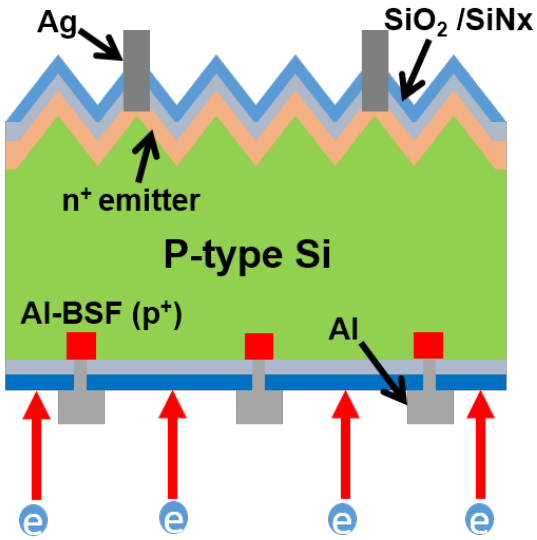

Figure 73: Schematic of negative charging on back surface of p-type bifacial PERC solar cells.

Then negative charge was injected in the SiNx from the rear side. Table 15 shows the average light I-V data of four p-type PERC cells before and after ~1e13cm^{-2} negative charge injection in SiO_2/SiNx stack at the back surface.

Table 15: Measured P-type PERC Cell LIV Data Before and After Negative Charging on Back SiO_2/SiNx Stack (-1E13cm^{-2})

Wafer Type	AVG of 4	V_{oc} (mV)	J_{sc} (mA/cm^2)	FF(%)	Efficiency (%)
p-type PERC Cell	Pre-charging	661	38.5	78.4	19.95 ±0.06
	Post-charging	661	38.6	79.0	20.18 ±0.09

In case of p-type PERC cells, absolute cell efficiency increased by 0.23% mainly

due to higher FF (ΔFF, +0.6%) with small increase in J_{sc} (ΔJ_{sc}, 0.1mA/cm2). This smaller efficiency increase in p-type PERC compared to n-type PERT is because p-PERC back surface is already inverted due to low boron doping (1e16 cm^{-3}) combined with positive charge in the SiO_2/SiNx. Inversion layer significantly reduces surface recombination velocity (SRV) because of asymmetric e-h concentration (a lot more electrons than holes), which reduced SRH recombination at the surface. Therefore formation of accumulation layer after negative charge injection has little impact on passivation, SRV, V_{oc} and J_{sc}. SRV is the measure of passivation quality and is defined by the following Equation,

$$\begin{aligned} S_{\text{eff}}(\frac{cm}{s}) &= \frac{U_{\text{s}}}{\Delta n}, \\ U_{\text{s}}(\frac{1}{cm^2 \cdot s}) &= \frac{n_{\text{s}} p_{\text{s}} - {n_{\text{i}}}^2}{\frac{(n_{\text{s}}+n_1)}{S_{\text{p0}}} + \frac{(p_{\text{s}}+p_1)}{S_{\text{n0}}}}, \end{aligned} \tag{29}$$

where S_{eff} is effective SRV, Δn is electron injection level, n_s and p_s are electron and hole concentrations at the surface, n_1 and p_1 are electron and hole concentrations if the Fermi energy is located at the trap levels, and S_{n0} and S_{p0} are fundamental surface recombination velocities for electrons and holes, respectively. According to Equation (29), SRV becomes lower if one type of carrier concentration significantly exceeds the other type of carrier concentration at the surface. Analitical modeling was used to obtain n_s and p_s values for different amount of charge at the surface. S_{p0} and S_{n0} values were calculated by using D_{it}, σ_n and σ_p from Glunz paper [79] for typical thermal oxide on silicon (Table 16). S_{p0} and S_{n0} are calculated by Sn0 (or Sp0) = σ_n (or σ_p)*V_{th}*D_{it}.

Table 16: Si-SiO_2 Interface Parameters

Thermal velocity for electron and hole	V_{th} (cm/s)	1E+07
Trap energy level	E_t (eV)	0.56
Interface trap density	D_{it} (1/cm2)	6E+10 [79]
Electron capture cross section	σ_n (cm^2)	2.5E-14 [79]
Hole capture cross section	σ_p (cm^2)	7.8E-17 [79]
Electron surface recombination velocity	S_{n0} (cm/s)	14879
Hole surface recombination velocity	S_{p0} (cm/s)	47

Table 17 shows the calculated SRV on the Si-SiO_2 surface from Equation (29) a function of charge density (Si-SiO_2 interface parameters were used from Glunz′s paper [79]). The SRV calculations (Table 17) show that injection of $\sim$1E13cm^{-2} positive or negative charge lowers the SRV well below 1cm/s of 1.8 ohm-cm p-type silicon [23, 80].

Table 17: Calculated SRV as a Function of Net Charge Amount on Si-SiO_2 Surface.

Negative charges						
Injected charge amount (cm^{-2})	No charge	-1.5E11	-2E11	-5E11	-1E12	-1E13
SRV (cm/s) @1e15 cm^{-3} injection level	954	1001	761	171	45	0.5
Positive charges						
Injected charge amount cm^{-2}	No charge	1.5E11	2E11	5E11	1E12	1E13
SRV (cm/s) @1e15 cm^{-3} injection level	954	33	11	1	0.2	1E-03

Next, we performed device simulation using Sentaurus 2D model, which allows us to place desired amount of charge on the back of the p-PERC cell. Figure 74 shows the calculated PERC cell efficiency as a function of a rear surface charge in our PERC cell structure. There is a very sharp drop in efficiency if the charge value approaches zero and then it rises up to a nearly identical value with either positive or negative charge $\geq$ 5e12cm^{-2}

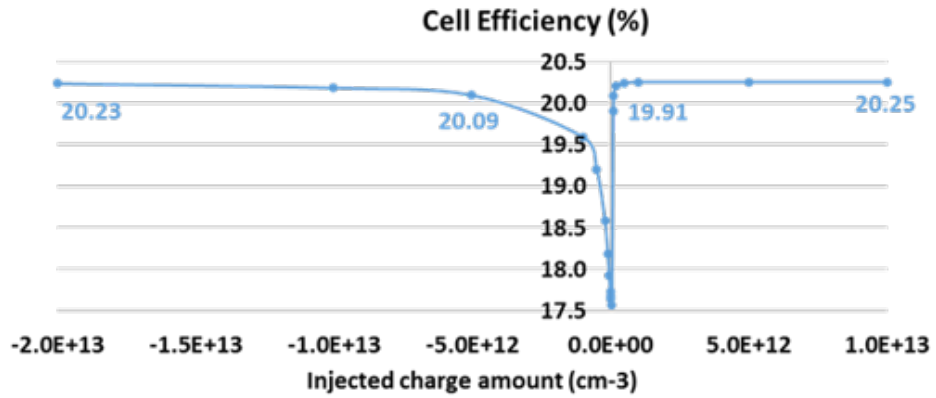

Figure 74: Sentaurus 2D device simulation on p-type bifacial PERC as a function of net charge amount on back SiO_2/SiNx stack.

Device modeling shows the efficiency increases from ~17.5% to ~20% with increase in charge from zero to ±5E12 cm^{-2} on the back of the PERC cell and then the efficiency saturates. Thus, calculated SRV and Sentaurus 2D device modeling both show that field effect passivation by either accumulation with negative (-1E13cm^{-3}) or inversion with positive charge (+1E13^{-3}) provides good surface passivation as also explained by bend diagrams in Figure 75.

Figure 75 shows that both inversion and accumulation can achieve low surface recombination velocity since in both cases only one type of carrier in the surface is dominant at the surface. This is further supported by calculated change in electron and hole concentration at the surface as a function of charge as shown in Figure 76.

Slight asymmetry in Figure 74 is due to different values for S_{n0} and S_{p0} because of different electron and hole capture cross section values (σ_n,σ_p) for Si-SiO_2 interface

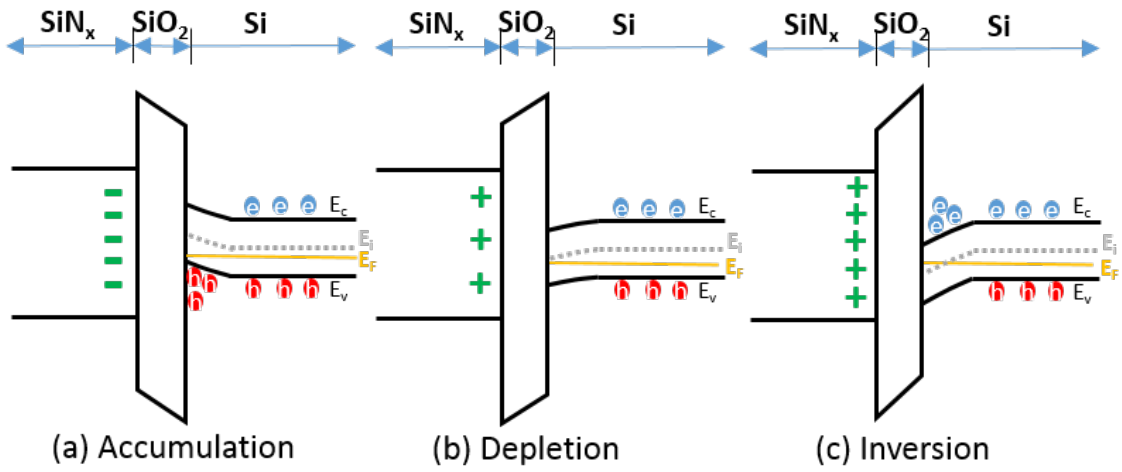

Figure 75: Band diagrams of (a) accumulation layer (b) depletion layer and (c) inversion layer.

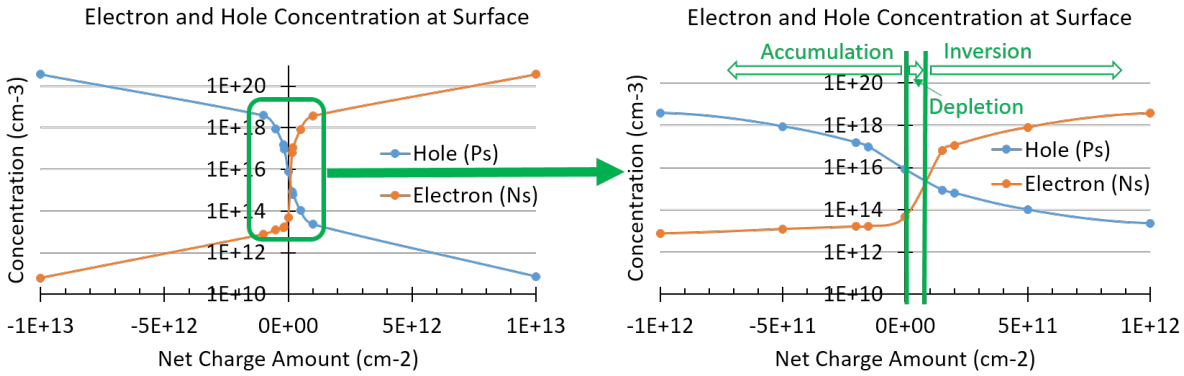

Figure 76: Electron and hole concentration at the surface of boron-doped p-type silicon with 8e15cm^{-3} doping as a function of net charge amount.

defects [81]. This explains why there was no change in V_{oc} (Table 15) before and after negative charging. However, p-type PERC did show an increase in FF by 0.6% and J_{sc} by 0.1mA/cm^2 after the negative charge injection. This is supported by IQE measurements with and without the light bias in Figure 77.

Without light-bias, IQE responses on long wavelengths (650nm∼1200nm) increased after negative charging. This increase is because negative charging of PERC's back surface switches the inversion layer to accumulation layer, removing parasitic shunt mechanisms between inversion layer and metal contact such as pinholes in the

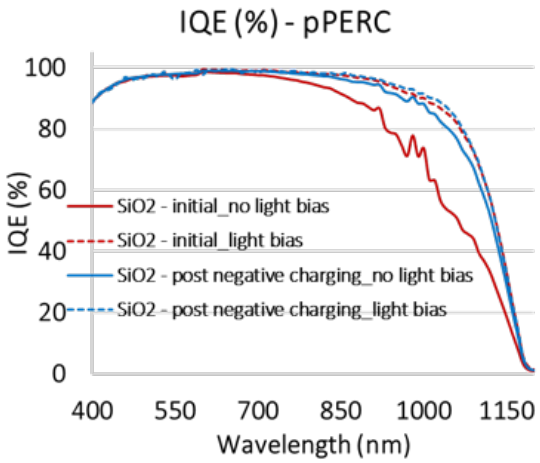

Figure 77: Measured Internal Quantum Efficiency (IQE) on p-type PERC solar cell before and after charge injection.

positive charged SiO_2/SiNx passivation or insufficiently formed back surface field in Al-BSF [82], which was not accounted for ideal 2D device simulation. Also, measured effective lifetimes (Figure 78) at lower injection levels (1e12 cm^{-3} to 5e14 cm^{-3}) showed an increase after negative charge injection. This explains the observed small increase in FF and J_{sc} because at injection levels or voltages below V_{oc}, the current should be higher in cells with negative charge injection which will make the I-V curve more square and increase the FF. Since effective lifetime at V_{oc} or injection level of ~1E15 cm^{-3} is virtually identical for both cells, no improvement in V_{oc} was observed after charge injection [83].

6.4 Conclusion

In this chapter, we demonstrated field effect passivation by negative charge injection in the SiO_2/SiNx stack on boron emitter of the n-type PERT cells and boron-doped rear surface of the p-type PERC cells. Negative charge injection was performed by a novel low cost high throughput plasma charging tool and method developed by Amtech company. C-V measurements on the MOS structures showed that this tool can inject negative charge upto ≥1e13cm^{-2} easily in the SiO_2/SiNx stack.

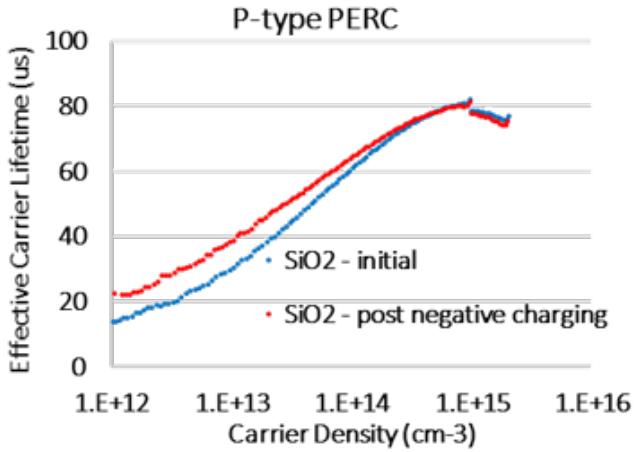

Figure 78: Measured effective lifetimes as a function of injection level on p-type PERC cell by Sinton Suns-Voc tool before and after negative charge injection (net charge: -1e13 cm^{-2}).

The negative charge is mostly trapped in the SiNx layer and at the SiO_2/SiNx interface. Detailed analysis showed that the emitter saturation current density (J_{oe}) of SiO_2/SiNx passivated boron emitter (85ohm/sq) decreased from ~80fA/cm^2 to ~50fA/cm^2 after 7.9e12cm^{-2} negative charge injection. This J_{oe} value is equivalent to the J_{oe} of widely used Al_2O_3/SiNx (negative fixed charge) passivated boron emitter, suggesting that this simple and low-cost technique can be used to replace the more expensive and hazardous PECVD Al_2O_3 deposition tool in industry. Large area (239 cm^2) n-type PERT and p-type PERC cells were fabricated and injected with negative charge. It was shown that cell efficiencies increased by 1.35% and 0.23% absolute for n-PERT and p-PERC cells, respectively, after 1E13 cm^{-2} negative charge injection in SiO_2/SiNx stack. N-type PERT cells showed an increase in all the key cell parameters including V_{oc} (ΔV_{oc}, 12mV), J_{sc} (ΔJ_{sc}, 1.6mA/cm^2) and FF (ΔFF, 0.5%). Detailed characterization and modeling revealed that negative charge injection transformed the boron emitter surface in n-PERT cell from depletion mode to accumulation mode, reducing the recombination at the surface defects. This is because SRH recombination decreases rapidly when one type of carrier concentration is

much greater than the other. In case of p-type PERC cell, efficiency increased only by 0.23% absolute mainly due to increase in FF (ΔFF, 0.6%) and a small increase in J_{sc} (ΔJ_{sc}, 0.1mA/cm^2). This is because C-V measurements on MOS structure showed that p-PERC back surface is inverted before negative charge injection due to large positive charge in the dielectric stack in conjunction with low boron doping in the base. Inversion layer provides excellent surface passivation due to much higher electron concentration than hole concentration. When negative charge injection transforms the back surface from inversion to accumulation, with much higher hole concentration, there is not much change in passivation or V_{oc} was observed. However, since there are very little amount of electrons at the accumulated surface, parasitic shunting or leakage of minority carriers at the back contact is reduced or eliminated because back surface now primarily has majority carriers. In addition, it was found that negative charge injection also improved effective lifetime at lower injection below V_{oc}. These two factors contributed to increase in J_{sc} and FF.

CHAPTER VII

TASK 4: IMPLEMENTATION OF PERC SOLAR CELLS WITH SELECTIVE EMITTER FORMED BY ETCH-BACK PROCESS

High recombination in the phosphorus doped homogeneous emitters in PERC cells is partly responsible in limiting the efficiency of current industrial PERC cells. This is because these emitters have too much doping in the field region to reduce emitter bulk recombination and surface recombination and there is not enough doping underneath the metal contacts to reduce metal recombination. This results in high J_{oe}, Lower V_{oc} and cell efficiency. Selective emitter can solve this problem because it uses heavy doping underneath the metal grid and lower doping between the metal grid or the field region. Metal contact area is more heavily-doped compared to homogeneous emitter to decrease Shockley-Read-Hall (SRH) recombination by band-bending effect, but un-metallized field area is lightly-doped to decrease Auger recombination and band gap narrowing effects. In addition, dielectrics can provide better passivation to a lightly doped surface. Thus selective emitter reduces emitter saturation current density for both metallized and non-metallized areas compared to the homogeneous emitter. There are many techniques to form selective emitter including laser doping [84], selective ion implantation [85], and etch-back. In this chapter, we developed a wet chemical etch-back process using a resist mask for phosphorous emitter since etch-back process is known for its cost-effectiveness [86].

Structure and fabrication process used in this research for making PERC cells with selective emitter are shown in Figure 79. First, as received p-type Cz silicon ($\sim$2ohm-cm resistivity) wafers were immersed in heated KOH solution for saw damage

removal followed by pyramid-like alkaline texturing of both surfaces. Then, rear side was planarized by capping the front side with SiNx and using a KOH solution for back planarization. Phosphorus ion-implantation was used to form a ∼60 ohm/sq heavily doped homogeneous emitter. This was achieved by 10keV phosphorus implant with dose of 5e15cm^{-2} followed by 850°C, 20 minutes anneal in N_2 and O_2 ambients. In-situ thin oxide was grown on front (25nm) and back (8nm) surfaces during this implant anneal. PECVD SiNx film was deposited on back (200nm) surface to protect the oxide and enhance back surface reflectance. Then, a resist was scree-printed on the front to define n^{++} grid pattern and mask chemical etching. Wet chemical etching by a mixed solution (DI water/HF/$NaNO_2$) was used to consume or form porous silicon layer on unmasked portion of the heavily doped emitter surface. Resist mask was then removed by dipping in dielthilene glycol monobutyl ether in an ultrasonic bath for two minutes. Finally, porous silicon layer was removed by 1% KOH solution at room temperature to form a lightly-doped emitter (100-200 ohm/sq) in the field regions between the grid. Then a UV laser (Alabama Laser, 355 nm wavelength with nanosecond pulse width) was used to open a line pattern through the rear dielectric stack (65um wide and 1mm pitch) to form local BSF and contacts. Finally, Ag grid was screen printed on the front and full Al on the entire back, followed by co-firing at ∼800°C for 3 seconds to form front and back contacts including the local Al-BSF (Figure 79).

7.1 Details of Selective Emitter Formation by Wet Chemical Etch-back Process

Selective emitter formation consists of four steps as discussed above and shown in Figure 79: printing resist for masking, formation of porous silicon layer, removal of resist masking, and porous silicon removal. These four steps can be separated into two different processes. One process is to print and remove resist mask to prevent etching of heavily-doped portion of the selective emitter. The other process is to etch

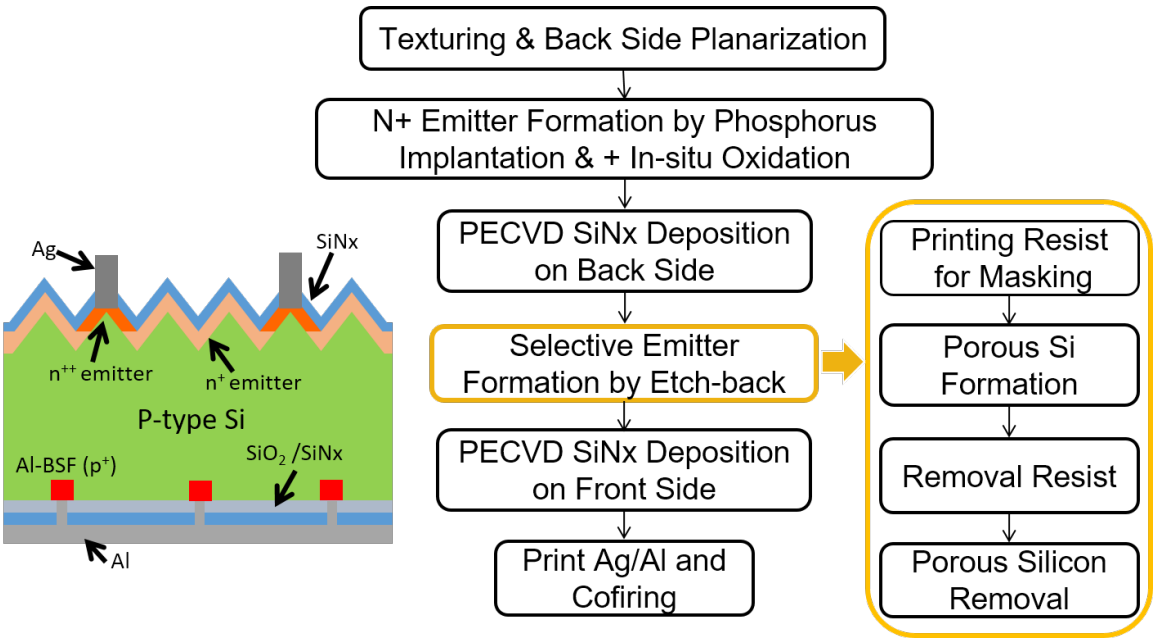

Figure 79: Selective emitter PERC solar cell structure and its fabrication procedures.

the heavily-doped emitter (n^{++}) between the grid pattern (field region) to achieve lightly-doped portion of the selective emitter (n^{+}) by first forming and then etching porous silicon layer by appropriate wet chemical solutions.

7.1.1 Printing and removing resist mask

First, a resist paste mask was screen-printed with a gridline pattern on top of heavily-doped phosphorus emitter (n^{++}). Figure 80 shows that the width of resist mask was designed to be ~220 um (pitch of 1.54mm) to facilitate alignment of ~60um wide screen-printed Ag gridlines within the n^{++} regions. Resist paste (SD-2052 AL from Peters company) and screen printing parameters (snap-off = 1.5mm, pressure = 70N, end squeeze speed = 60~130mm/s) were carefully selected to avoid paste clogging on screen. After printing, the resist mask was dried on a belt furnace at 250°C for one minute.

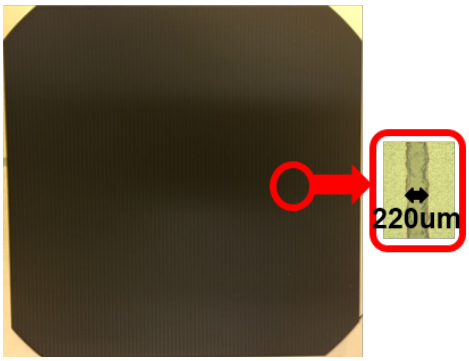

Figure 80: Screen Printed Resist Mask for Fingers.

After porous silicon formation and etching, the printed resist mask was removed by immersing the wafer in a heated solution (40°C, 25% diethylene glycol butyl ether (BDG) in DI water) in an ultrasonic bath for two minutes. Figure 81 shows microscope images of screen printed resist mask and wafer after removing the resist.

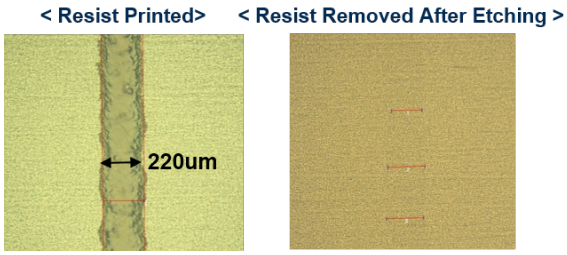

Figure 81: Microscope images of screen printed resist mask and wafer post removing the resist after chemical etching.

7.1.2 Formation and etching of porous silicon layer by wet chemistry

In order to form lightly-doped field emitter region between n^{++} grid lines, wet chemical etch-back process was performed by first growing a porous silicon layer on the unmasked heavily-doped regions (n^{++}) and then etching that layer to form lightly-doped field regions (n^{+}). An acidic solution composed of hydrofluoric acid (HF), aqueous sodium nitrite ($NaNO_2$) and deionized (DI) water was used to form a porous silicon layer. In order to achieve uniform porous silicon layer of controllable depth, proper wet chemical solution is important. This was achieved with 0.25% $NaNO_2$ and

0.25% HF in DI water. This reaction is similar to stain etching, proposed by Turner in 1960s [87], in which porous silicon layer is formed by electrochemical reaction by flowing local cell current between anodic and cathodic sites on the silicon surface. Figure 82 shows a uniform porous silicon layer achieved on the textured surface.

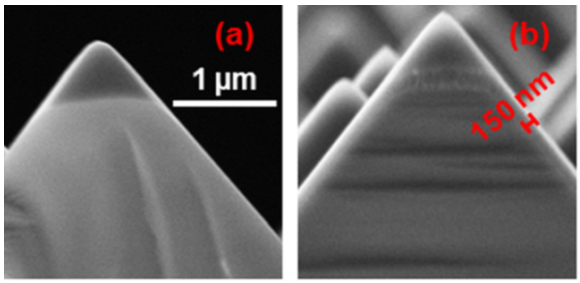

Figure 82: Scanning Electron Microscopy (SEM) images of pyramids (a) before forming porous silicon (b) after forming porous silicon layer (150nm) [88].

Next, the porous silicon layer was etched to form lightly-doped emitter region (n^+) by dipping the wafer in a mixed solution (0.5% KOH with 10% IPA in DI water) for two minutes at room temperature. This only removes porous silicon which is unstable in OH^{-1} solution [89], while the phosphorus emitter underneath the porous silicon layer is protected from over-etching. This etch-back process was first developed at the university of Konstanz and recently commercialized by Schmidt.

By varying the porous silicon formation time, we achieved various lightly doped field regions ranging from ~60 ohm/sq to ~200 ohm/sq as shown in Figure 83. Sheet resistance increased with increasing time in the porous silicon formation solution. Note that the porous silicon removal solution and time (two minutes) remained the same.

In addition to the sheet resistance, doping profiles were measured by electrochemical capacitance-voltage (ECV) measurements where emitter surface is gradually etched electrochemically followed by C-V measurement to determine active carrier concentration on the surface. Profiles in Figure 84 show that peak phosphorus concentrations in the starting 60 ohm/sq emitter was 3.1e20 cm^{-3} which decreased to 2.5e20

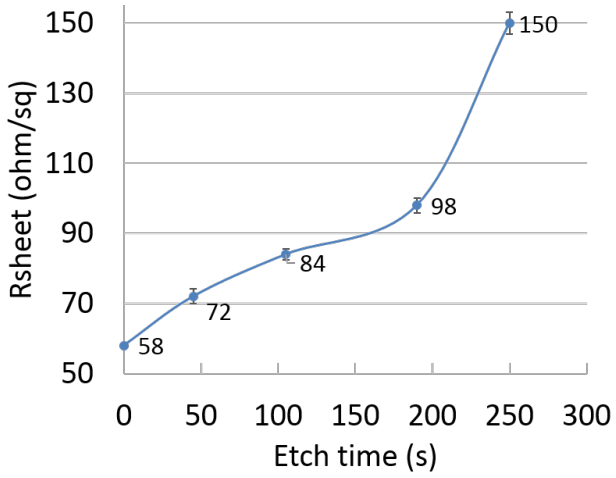

Figure 83: Measured emitter sheet resistance as a function of porous silicon formation time starting with initial ∼60 ohm/sq heavily-doped emitter.

cm^{-3} after etch back to 100 ohm/sq emitter and to 7.9e19 cm^{-3} in the 130 ohm/sq emitter. Higher sheet resistance emitters show lower emitter saturation current density (J_{oe}), as discussed in the next section. Note that the 100 and 130 ohm/sq etch-back ECV profiles were shifted by 28nm and 50nm compared to the initial heavily-doped (∼60 ohm/sq) emitter, indicating etching depth from the surface.

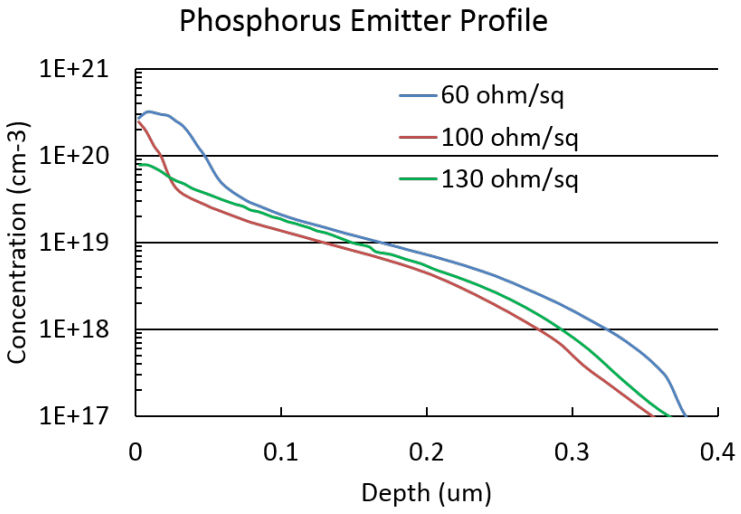

Figure 84: Measured electrochemical capacitance-voltage (ECV) profiles of initial ∼60 ohm/sq emitter and etch-backed emitters (100 and 130 ohm/sq).

7.2 Application of Selective Emitter to PERC Solar Cells

7.2.1 Measurements of emitter saturation current density for various etched-back emitters

Before applying selective to PERC solar cells, emitter bulk recombination and surface passivation quality was quantified by measuring emitter saturation current density (J_{oe}). First, symmetric test structures were fabricated (Figure 85) on high bulk lifetime n-type (≥1ms) Cz wafers. And QSSPC measurement was used to extract J_{oe} [90]. Heavily-doped phosphorus emitter (∼60 ohm/sq, n^{++}) was formed on both sides of the wafer by phosphorus ion-implantation (5e15 cm^{-2} dose and 10keV energy) followed by annealing (855°C for 30 minutes). Then, wet chemical etch-back process was performed to form lightly-doped phosphorus emitters. SiNx dielectric was deposited on both surfaces to improve surface passivation and provide anti-reflection coating on the front as will be done on the front side of the regular PERC cell.

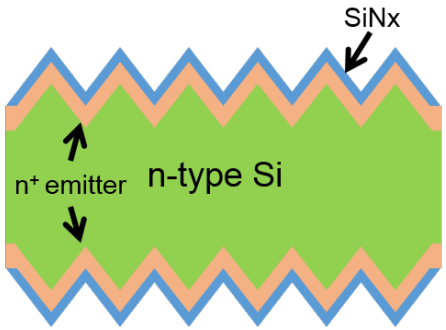

Figure 85: Symmetric test structure for J_{oe} measurements of etch-backed emitter.

J_{oe} was determined for all the etched-back emitters in the range of ∼60∼200 ohm/sq. This technique gives a plot of effective lifetime as a function of injection level as shown in Figure 86 which is described by the following Equation,

$$\frac{1}{\tau_{\text{eff}}} - \frac{1}{\tau_{\text{Auger}}} = \frac{1}{\tau_{\text{SRH}}} + 2\frac{J_{\text{oe}}(N_{\text{d}} + \Delta n)}{q{n_{\text{i}}}^2 W}, \tag{30}$$

where τ_{eff}, τ_{Auger} and τ_{SRH} are the measured effective lifetime, the intrinsic Auger and the intrinsic SRH lifetime, N_d is base wafer doping concentration,n_i is the intrinsic

carrier concentration, Δn is excess carrier density and W is wafer thickness [28, 30]. Slope of the linear plot in Figure 86 gives $2J_{oe}/qn_i^2W$ from which J_{oe} is extracted.

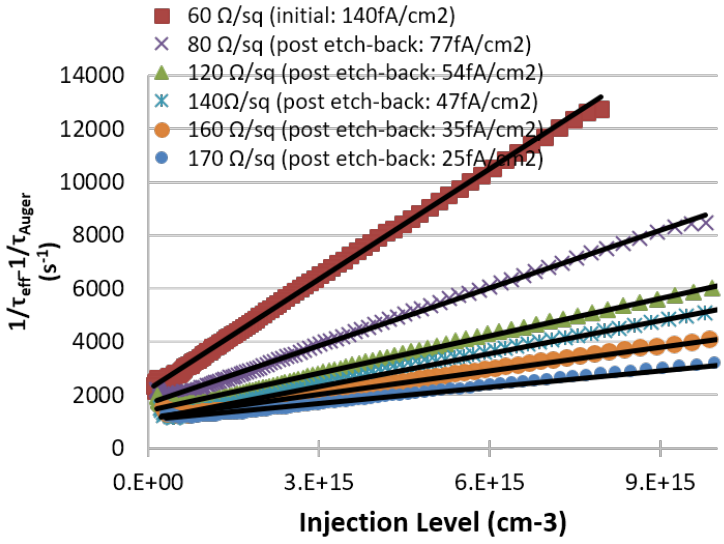

Figure 86: Measured Auger-corrected inverse effective lifetime as a function of injection level for initial (∼60ohm/sq) and etch-backed emitters.

As expected, Figure 86 shows that higher sheet resistance gave smaller J_{oe} due to reduced emitter bulk and surface recombination.

Figure 87 shows extracted J_{oe} as a function of sheet resistance for 23 different etched-back emitters including the un-etched 60 ohm/sq heavily-doped emitter which gave a J_{oe} of 140 fA/cm^2 which decreased to 14 fA/cm^2 when it was etched back to 200 ohm/sq.

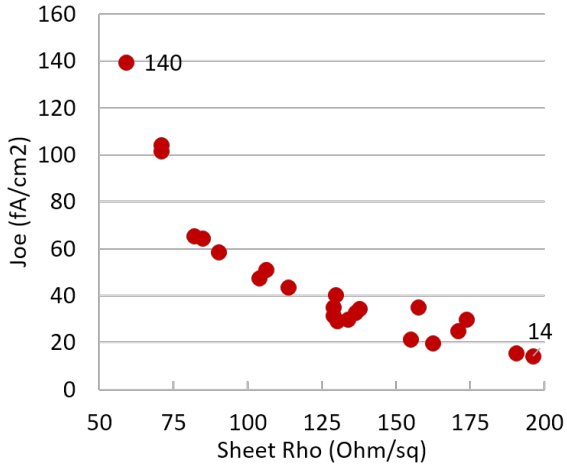

Figure 87: Measured J_{oe} as a function of sheet resistance for initial and etch-backed emitters.

7.2.2 Enhanced performance of PERC solar cells with selective emitters

In this section, the etch-back process was applied to fabricate large area screen printed selective emitter PERC solar cells with 60 ohm/sq n^{++} region and 130 ohm/sq n^{+} field region with cooperation from University of Konstanz. For comparison, we also fabricated 60 and 90 ohm/sq homogeneous emitter PERC cells. Fabrication steps were described in the introduction of this chapter (Figure 79). Table 18 shows the measured average and the best cell data from each group. The I-V tester (PV measurement) was calibrated using the Fraunhofer ISE certificated reference cell before measuring the actual cells.

Table 18: Measured Light I-V Results of p-type PERC Solar Cells with Homogeneous or Selective Emitters.

Emitter Type		V_{oc} [mV]	J_{sc} [mA/cm2]	FF [%]	Efficiency [%]	n-factor	RSERIES [ohm-cm^2]
Homogeneous (60 ohm/sq)	Best	648	38.3	80.2	19.89	1.10	0.34
	AVG (5)	648	37.9	80.3	19.70 ±0.16	1.11	0.31
Homogeneous (90 ohm/sq)	Best	658	38.5	79.8	20.23	1.16	0.31
	AVG (5)	657	38.5	79.6	20.12 ±0.10	1.15	0.38
Selective (60/130 ohm/sq)	Best	664	39.1	78.8	20.49	1.23	0.43
	AVG (3)	662	39.0	78.8	20.34 ±0.15	1.23	0.43

Selective emitter cell achieved the highest efficiency of ∼20.49% representing an increase of 0.60% in absolute efficiency over the 60 ohm/sq and 0.26% increase over the 90 ohm/sq homogeneous emitter. In this experiment, baseline homogeneous (90ohm/s) emitter PERC cell showed only average efficiency of 20.1% compared to 20.6% in the Chapter 5, possibly due to some bulk contamination during fabrication of these cells. Removal of this contamination could drive PERC cell efficiency to ∼21% with selective emitter. The impact of bulk lifetime on selective emitter PERC cells will be discussed in Chapter 8. Note that selective emitter cells showed highest V_{oc} of 662 mV compared to 648 mV and 657 mV for the two homogeneous emitter cells. This is mainly due to lower J_{oe} of 35 fA/cm^2 130 ohm/sq emitter (Figure 87). Note that this selective emitter improvement also includes the use of floating busbar technology, which reduces metal-silicon contact recombination because busbar does not contact silicon as described in Chapter 8. Reduced emitter or total recombination in the selective emitter cell is further supported by the PL images of these cells in Figure 88. Clearly selective emitter cell gave the highest PL response due to reduced emitter recombination.

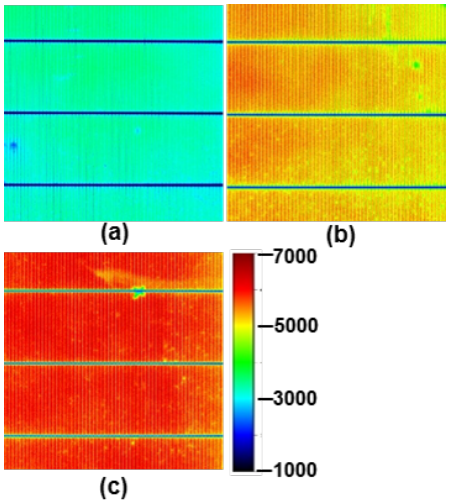

Figure 88: Measured photoluminescence (808nm) images of (a) heavily-doped homogeneous emitter (∼60 ohm/sq), (b) baseline homogeneous emitter (90 ohm/sq) and (c) selective emitter (∼60/130 ohm/sq).

We also measured internal quantum efficiency (IQE) responses of these three PERC cells as a function of wavelength. Figure 89 shows that selective emitter cell has the highest blue responses (380nm∼500nm) which is consistent with the highest V_{oc} and J_{sc} (Table 18) and lowest surface concentration in the field region (Figure 87).

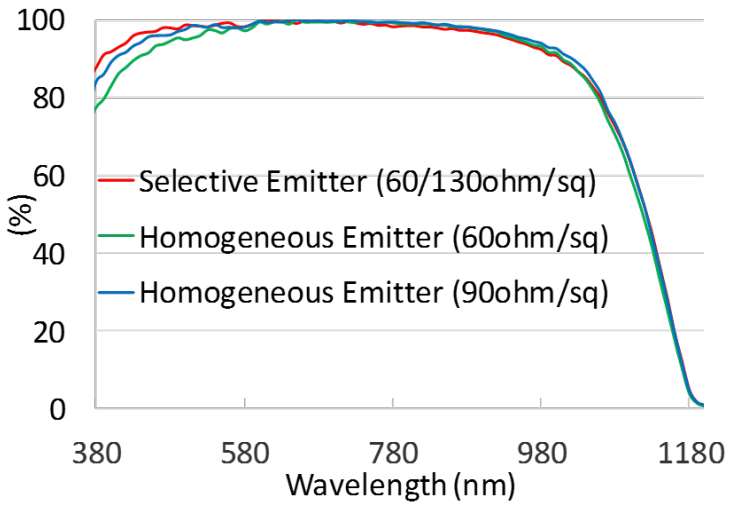

Figure 89: Measured internal quantum efficiency (IQE) from 380nm to 1200nm for selective emitter (∼60/130 ohm/sq) and two homogeneous emitters (∼60ohm/sq and 90ohm/sq) PERC cells.

However, selective emitter cells showed lower FF compared to the homogeneous emitter cells (Table 18). This is due to higher series resistance from lightly-doped field region (130 ohm/sq). In addition, higher n-factor in the selective emitter cell also decreased FF. In order to understand this effect, we performed effective lifetime VS injection level measurements using the Suns-Voc measurement on the finished cells (Figure 90) [91].

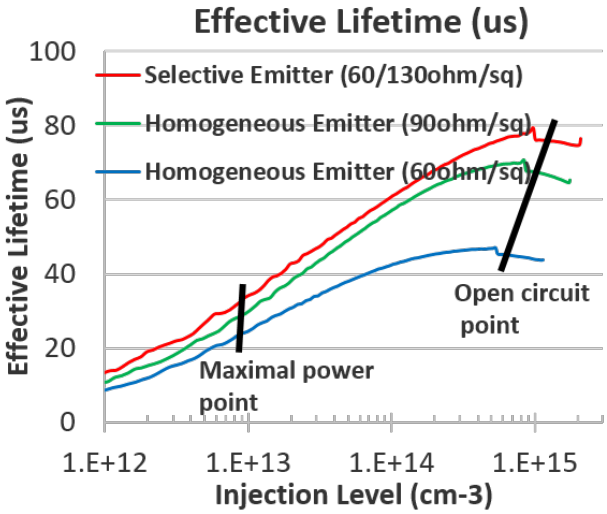

Figure 90: Measured effective lifetime by Sinton Suns-Voc tool for selective emitter (∼60/130 ohm/sq) and two homogeneous emitters (∼60ohm/sq and 90ohm/sq) PERC cells.

Figure 90 shows the injection levels at V_{oc} (1e15 cm^{-3}) and V_{max} (1e13 cm^{-3}). Selective emitter cell showed the largest drop in lifetime from V_{oc} to V_{max} which implies decrease in the squareness of I-V curve, resulting in higher n or lower FF. Higher injection level dependence in selective emitter cell could result from some contamination associated with the etch-back process. If the bulk lifetime, sheet resistance and injection level dependence problems can be solved, then selective emitter PERC cell efficiency could be ∼21%.

7.3 Conclusion

In this chapter, selective emitter technology was implemented by developing an chemical etch-back process to replace homogeneous phosphorous emitter in the PERC cells. Since selective emitter design uses a heavily doped n^{++} region underneath the metal contact area and a much lighter n^{+} doped region in the field region (non-metal contact area), this reduces both metal-induced recombination as well as field emitter recombination. In order to achieve selective emitter, we developed wet chemical etchback process, consisting of four steps: printing resist for masking heavily diffused

regions, formation of porous silicon layer in between the resist by chemical etching, removal of resist masking, and removal of porous silicon by chemical etching. Using this etchback process, large area screen printed selective emitter PERC solar cells were fabricated with 60 ohm/sq n^{++} grid region and 130 ohm/sq n^{+} field region in between, replacing the standard 60 or 90 ohm/sq homogeneous emitters PERC cells. Selective emitter cell achieved the best efficiency of 20.49% representing an absolute efficiency increase of 0.60% over the 60 ohm/sq homogeneous emitter (19.89%) and 0.26% increase over the 90 ohm/sq homogeneous emitter (20.23%). Note that selective emitter cells showed highest V_{oc} of 662 mV compared to 648 mV and 657 mV for the two homogeneous emitter cells. This is mainly due to the lower J_{oe} of 35 fA/cm^2 130 ohm/sq emitter (Figure 87). This demonstrates the merit of using selective emitter in PERC cells.

CHAPTER VIII

TASK 5: SENTAURUS 2D DEVICE SIMULATIONS TO DEVELOP A ROADMAP FOR HIGH EFFICIENCY PERC SOLAR CELLS

8.1 Basics of Sentaurus 2D Device Modeling and Its Application to Match PERC Cells

A TCAD (Technology Computer Aided Design) software program, Sentaurus (Synopsis) is widely used in PV industry for modeling solar cell [92, 93] because numerical solutions of semiconductor equations are necessary to quantitatively and rigorously analyze solar cells. Figure 91 shows a flowchart describing how Sentaurus modeling was used in this research to model and match PERC solar cells in this research.

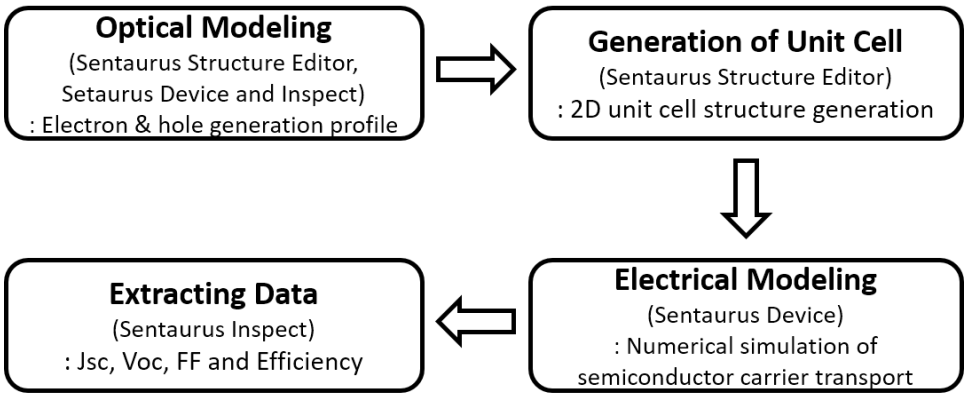

Figure 91: Flowchart describing Sentaurus modeling for a silicon solar cell.

First step involves extraction of generation profile by optical modeling using Sentaurus Structure Editor, Sentaurus Device, and Inspect programs. Using Sentaurus Structure Editor, we create a unit cell for ray-tracing to extract light generated profile as shown in Figure 92. Ray-tracing is run by a built in Sentarus Device program.

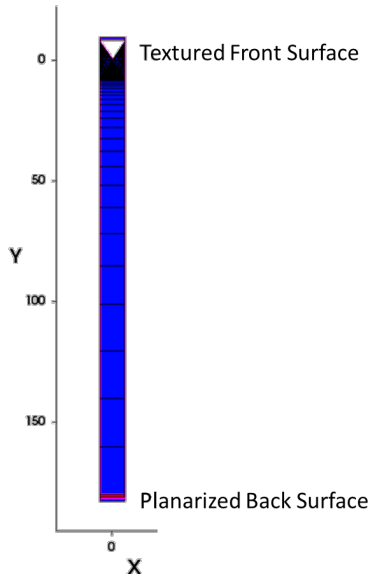

Figure 92: Unit cell for ray-tracing (wafer thickness: 180um, textured front surface capped with dielectrics SiNx/SiO_2 and planarized back surface).

Figure 93 shows concentration of light generated electron-hole pairs as a function of wavelength and depth from surface optimized from Ray-tracing results.

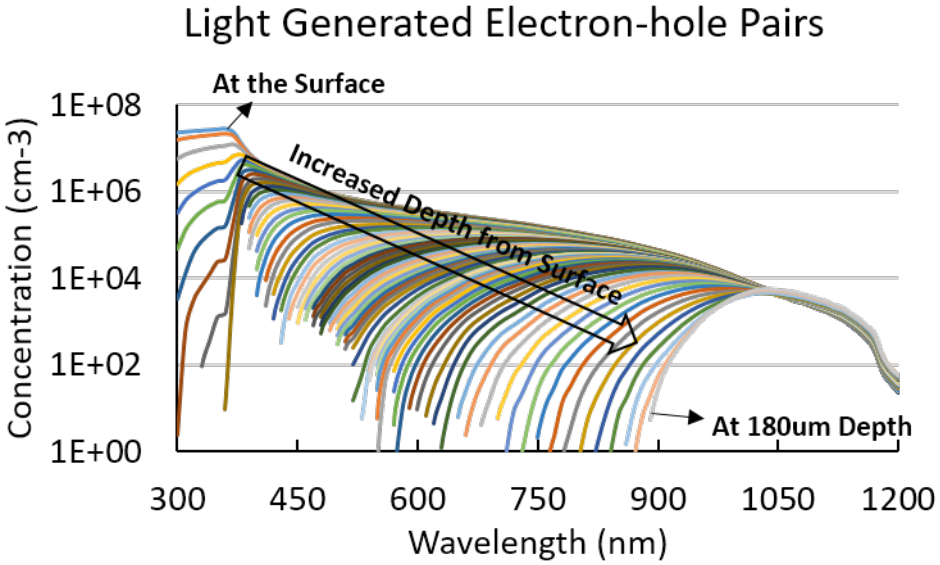

Figure 93: Light generated electron-hole pairs as function of wavelength and depth from surface.

Figure 94 shows that concentration of generated electron-hole pairs (integrated for all wavelength) is highest (2.6e21 cm^{-3}) on the front surface and lowest (1.7e18 cm^{-3}) at the back surface (180um).

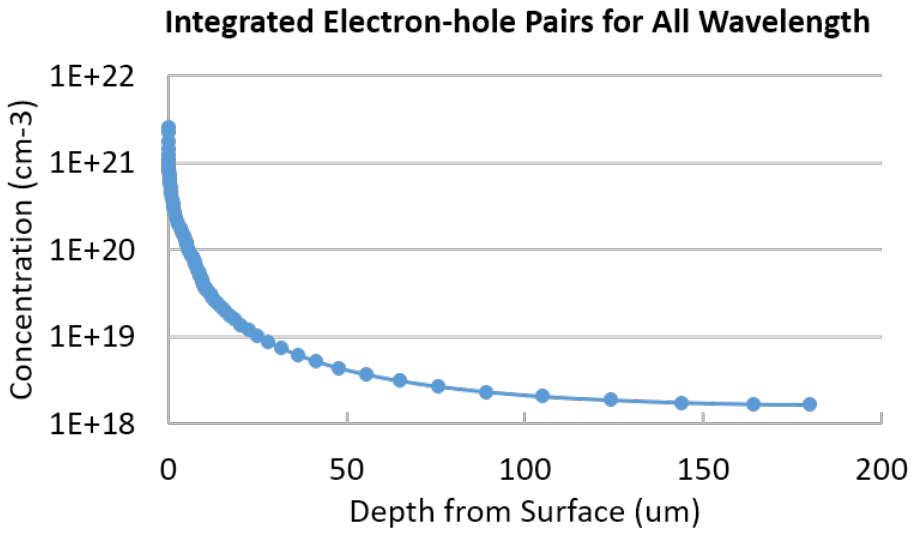

Figure 94: Light generated electrons and holes as function of depth from surface (integrated for all wavelength).

Next, 2D unit cell of a p-type PERC solar cell structure was designed using Sentaurus Structure Editor (Figure 95). This unit cell is only 3.5mm wide and 180um thick, which represents large area 3D solar cell (156mm x 156mm x 180um). This is done to speed up the numerical modeling. Front contact width for this unit cell was chosen to be 100.75 um, which includes the finger width (50um) and 2.9% busbar contribution to metal coverage (3.5mm*2.90%/2=50.75um).

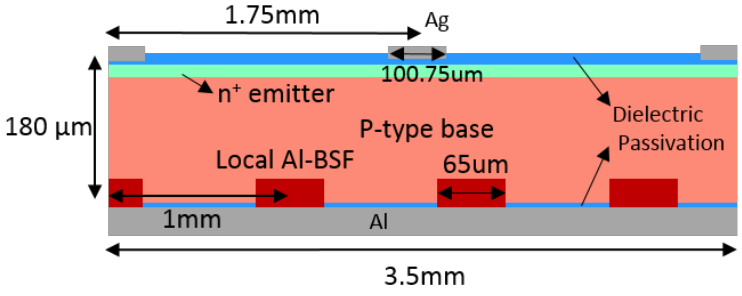

Figure 95: Generated 2D unit cell of p-type PERC solar cell.

After creating the unit cell, electrical modeling was performed by Sentaurus Device program using required input parameters shown in Table 19. Several pysical

models were selected for simulation, Schenk model for bandgap narrowing, Fermi-Dirac Statistics for heavily doped region, Klaassens model for unified mobility, and Dziewior and Schmid's Auger recombination coefficient recommended by Pietro P. Altermatt [93]. To test this model, first a 20.6% PERC solar cell with homogeneous emitter was characterized to extract required input parameters for Sentaurus modeling (Table 19).

Table 19: Key Parameters for Sentaurus 2D Modeling of Baseline PERC Cell.

		Parameters	P-PERC
Sentaurus Input Parameters & ***Extracted Values***	Emitter Profile & Front Passivation	Emitter Sheet Resistance (ohm/sq)	90
		Selective Sheet Resistance (ohm/sq)	N/A
		$J_{oe,\ n+,\ field}$ ***(fA/cm²)***	66
		$J_{oe,\ n++,\ selective}$, ***(fA/cm²)***	N/A
		$J_{oe,metal}$ ***(fA/cm²)***	61.2
	BSF Profile & Back Passivation	Al-BSF depth (um)/ doping (cm^{-3})	2/5e18
		Back Passivation Stack (cm^{-2})- SiO_2/SiNx	65 (Sn), 5 (Sp)
		$J'_{ob,\ field}$ ***(fA/cm²)***	28
		$J'_{ob,\ metal}$ ***(fA/cm²)***	35
	Material (Wafer)	Wafer Resistivity (ohm-cm)	1.6
		Bulk lifetime (ms)	500
		$J_{o\text{-}bulk}$ ***(fA/cm²)***	48
	Contact Formation	Front contact width (m)/ busbar width (mm)	50/0.9
		Total shading (%)	5.77
		Back contact width	65 um

Phosphorus emitter profile was measured by ECV tool and inserted in the modeling. In order to extract $J_{oe,\ n+,\ field}$, we fabricated symmetric test structures (Figure 96a) and measured J_{oe} by QSSPC tool as explained in Chapter II. $J'_{ob,\ field}$ was extracted by first fabricating symmetric test structures (Figure 96b), measuring and calculating $J'_{ob,\ field}$ by QSSPC tool. $J_{oe,metal}$ and $J'_{ob,\ metal}$ were measured and calculated by printing various metal fraction on PERC solar cells. $J_{ob,bulk}$ is extracted from bulk lifetime measured by QSSPC on a wafer passivated by I_2/Me solution (Figure 96c).

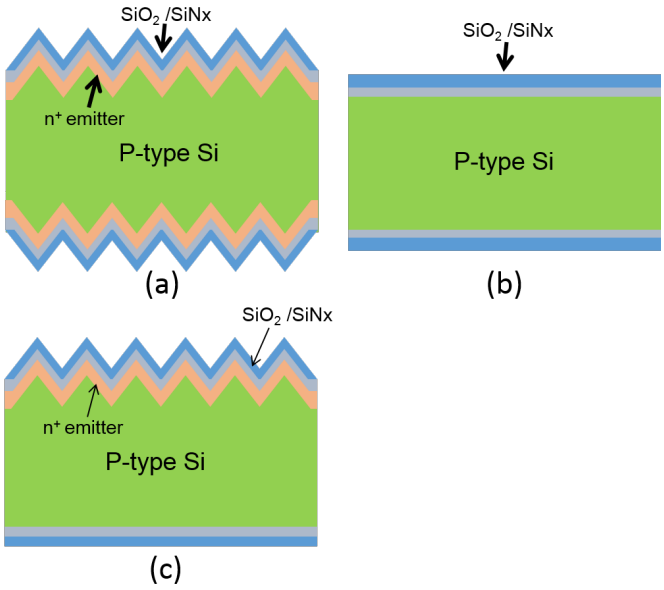

Figure 96: Test structures for (a) J_{oe} (b) SRV and J_{ob}' and (c) bulk lifetime.

Sentaurus 2D modeling using this approach gave an excellent match between the measured and modelled cell parameters as shown in Table 20.

Table 20: Comparison of Measured and Modeled Cell Parameters of 20.6% PERC Cell.

LIV Parameters	Simulated Output	Measured Data
V_{oc} (mV)	663	665
J_{sc} (mA/cm^2)	38.9	38.9
FF (%)	80.0	80.0
Efficiency (%)	20.6	20.6
Rs (ohm-cm^2)	0.60	0.60
n-factor	1.08	1.08

8.2 Technology Roadmap for 23% Efficient PERC Cells

After developing the methodology and matching the baseline 20.6% efficient PERC solar cell, an efficiency roadmap was developed by extending Sentaurus 2D modeling to raise its efficiency to ~23% by practical and manufacturable technology developments. Key material and device parameters were varied along with cell design features

in the model to drive the PERC cell efficiency from 20.6% to ∼23%. Figure 97 shows the technology roadmap to 23% efficiency.

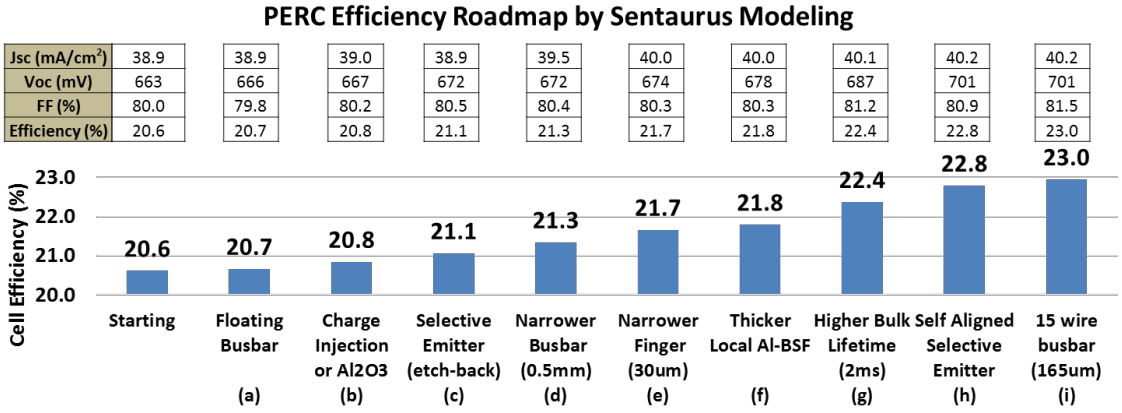

Figure 97: A roadmap to 23% PERC cell efficiency by Sentaurus 2D modeling.

First step (a) is to implement a floating busbar technology where busbars stay on top of dielectric and do not make direct contact to silicon (Figure 98). This reduces high recombination at the metal-silicon contact interface and decreases J_{oe}, and increases V_{oc} and efficiency. Notice that floating busbars do not punch through the AR coating (Figure 98) but make contact to gridlines to carry current. This reduces the metal-Si contact area from ∼5.8% to ∼2.9% because busbar coverage alone is ∼2.9%. This can be accomplished by using special low glass frit or fritless silver paste for printing busbar, which does not fire through the SiO_2/SiNx stack. Change in J_{oe} can be calculated from metal fraction and the measured J_{oe} field and $J_{oe,metal}$. According to the following Equation (31), 2.90% reduction in metal-silicon contact area should lower J_{oe} by ∼30fA/cm^2 and raise V_{oc} from 663 mV to 666 mV.

$$\begin{aligned} J_{o,total} &= J_{oe} + J_{ob} \\ J_{oe} &= J_{oe,\ field} * (1 - f_{fm}) + J_{oe,\ metal} * f_{fm} \\ V_{oc} &= \frac{kT}{q} ln(\frac{J_{sc}}{J_{o,total}} + 1) \end{aligned} \tag{31}$$

where $J_{o,total}$ is total saturation current density, J_{oe} is emitter saturation current density ($J_{oe,\ field}$=70 fA/cm^2 is for non-metallized area, $J_{oe,\ metal}$=1000fA/cm^2 (Table 5 in

Chapter 5) is for front metal-silicon contacted area), J_{ob} is saturation current density associated with base plus metallized and un-metallized back surface (35+28+48=111 fA/cm^2, Table 19), f_{fm} is front metal-silicon contact fraction, q is elementary charge and k is boltzmann constant. Sentaurus 2D device modelling also showed an increase cell efficiency by 0.1% due to increase in V_{oc} from 663mV to 666mV in conjunction with 30 fA/cm^2 reduction in J_{oe} (Figure 97).

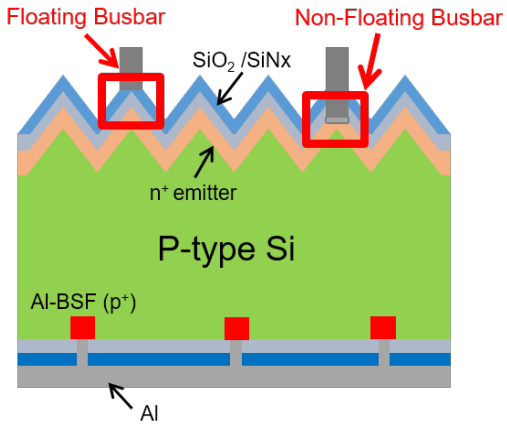

Figure 98: Schematic of PERC cell featuring floating Busbar and non-floating busbar.

Enhancement (b) in Figure 97 involves injecting negative charge into back passivation dielectric stack. Modeling showed that 1e13 cm^{-2} negative charge increases cell efficiency by additional ~0.1% by forming an accumulation layer at the back surface which enhances field-effect passivation and eliminates shunt mechanisms. The reason for this enhancement was discussed in Chapter 6.

Step (c) in the roadmap calls for replacing the homogeneous emitter by selective emitter which can reduce total J_{oe} because, compared to the homogeneous emitter, it uses heavy doping underneath the metal grid and lower doping between the metal grid or the field region (Figure 99). Metal contact area is heavily-doped to decrease Shockley-Read-Hall (SRH) recombination by band-bending effect, and un-metallized field area is lightly-doped to decrease Auger recombination and band gap narrowing effects. Thus selective emitter technology reduces emitter saturation current density

for both metallized and non-metallized areas compared to a homogeneous emitter. However, selective emitter needs to be designed properly to have maximum impact on J_{oe}. In order to study this, Sentaurus 2D device modeling was performed to assess the impact of doping and width of n^{++} region on J_{oe} and cell efficiency. Doping or sheet resistance of n^{++} region was varied in the range 13-60 ohm/sq and n^{++} width was varied from 50 to 400um. The sheet resistance between the metal contact or the field region was increased to 130 ohm/sq for modeling.

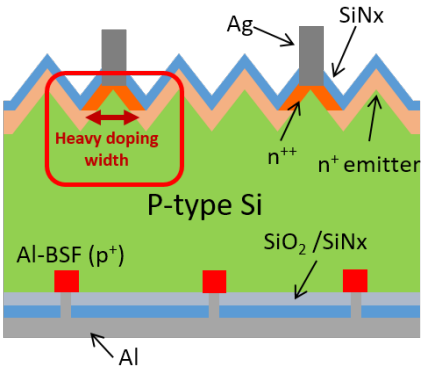

Figure 99: Schematic design of selective emitter on a PERC cell

The results of this modeling are summarized in Figure 100 which showed that highest efficiency is achieved when selective emitter width equals to the metal contact width (50um), or when emitter is self-aligned to metal contact.

This increases the efficiency of 20.8% homogeneous cell in Figure 97 to ~21.0%. However, since it is difficult to make self-aligned contacts using low cost screen printing technology, we explored different options where n^{++} or selective region width is greater than 50um. Figure 100 shows that 220um wide 60ohm/sq heavily-doped region in combination with 50um wide metal gridlines can also give an efficiency of ~21.0%. Such a selective emitter can be achieved by an etch-back process involving the formation of a 60 ohm/sq heavily-doped uniform emitter first, screen printing 220um wide resist mask, followed by etching the unmasked field region to raises the

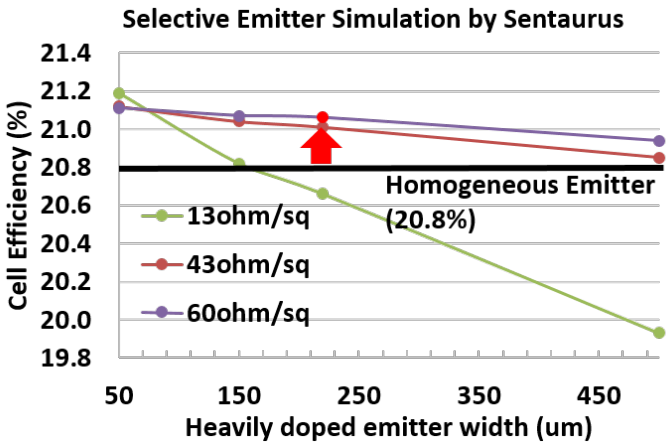

Figure 100: Impact of selective emitter technology on cell efficiency by Sentaurus 2D modeling (emitter for non-metal contact area fixed as a 130 ohm/sq for selective emitters).

sheet resistance to 130 ohm/sq. Modeling in Figure 97 shows that this selective emitter can provide 0.3% increase in cell efficiency in conjunction with 5mV increase in V_{oc} and reduction in J_{oe} from 95fA/cm^2 to 65fA/cm^2.

Steps (d) and (e) in our technology roadmap calls for advancing screen printing technology by further narrowing the busbar width from 0.9 mm to 0.5 mm and reducing gridline width from 50 um to 30 um (Figure 97 and Table 21). These improvements reduce shading and metal coverage which increase J_{sc}, V_{oc} and raise the efficiency to 21.7% efficiency (Figure 97 and Table 21).

Table 21: Front Metal Shading Impact on J_{sc} by Sentaurus Modeling.

Roadmap Step	Busbar Width (mm)	Gridline Width (um)	Total Front Metal Shading (%)	Modeled J_{sc} (mA/cm^2)	ΔEfficiency by Increased J_{sc} (%)
Initial	0.9	50	5.77	38.9	N/A
N/A	0.7	50	5.12	39.20	~0.16%
(d)	0.5	50	4.48	39.46	~0.15%
N/A	0.5	40	3.90	39.70	~0.13%
(e)	0.5	30	3.33	39.94	~0.14%

Enhancement in step (f) involves in increasing thickness of aluminium back surface field (BSF). This is dependent on aluminium paste material and firing conditions to form Al-Si alloy (Al-doped BSF). Currently, our Al-BSF is ~2um deep which results in $J_{ob,metal}$ of 35fA/cm^{-2} (Table 19). Modeling showed that increasing Al-BSF thickness to 7um can reduce $J_{ob,metal}$ to 11fA/cm^{-2} and increase cell efficiency by 0.1% due to increase in V_{oc} from 674mV to 678mV (Figure 97).

Enhancement (g) calls for improving bulk lifetime of wafers. This is mainly dependent on quality of wafers from vendors and cleanliness of cell processing. Modeling in Figure 97 shows that bulk lifetime enhancement from 500us to 2ms can significantly increase cell efficiency by 0.6% due to increase in V_{oc} (~9mV), J_{sc} (~0.1 mA/cm^2) and FF (~0.9%). This is because higher bulk lifetime reduces bulk recombination and base saturation current density (J_{ob}). Figure 101 shows that the impact of bulk lifetime improvement (from 150 us to 2ms) on V_{oc} is much greater for selective emitter cells with lower J_o compared to homogeneous emitter cell. 60/130 ohm/sq selective emitter increased V_{oc} by 9mV for 2ms bulk lifetime but gave only 4mV in V_{oc} for 150us bulk lifetime.

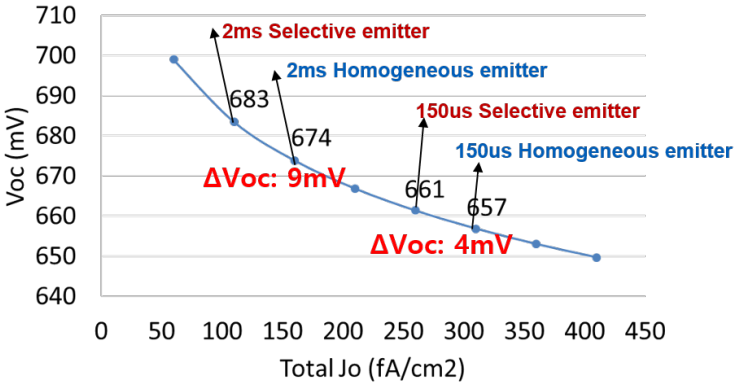

Figure 101: Impact of total emitter saturation current (J_o) on V_{oc} for bulk lifetime of 2ms compared to 150us using Equation (31).

Sentaurus modeling in Figure 102 shows that bulk lifetime is one of the most important factor for efficiency enhancement of advanced PERC cell and can raise the cell efficiency above 22% for lifetime in excess of 1ms.

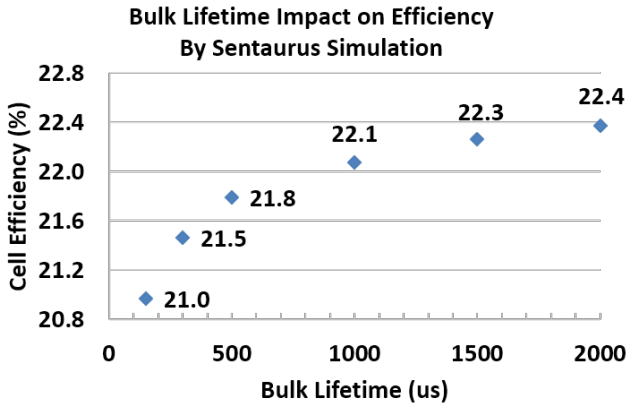

Figure 102: Impact of bulk lifetime on PERC cell by Sentaurus 2D modeling.

Enhancement (h) is to achieve self-aligned selective emitter with narrower (30um) fingers. This can be accomplished by laser doping of heavily doped region combined with electroplating the self-aligned metal contacts. Modeling in Figure 97 shows that applying this emitter can increase efficiency by 0.4% to a value of 22.8% (Figure 97) due to 14mV increase in V_{oc}, ~35 fA/cm^2 decrease in J_{oe}, and 0.1 mA/cm^2 increase in J_{sc} in spite of slight loss in FF due to 0.07 ohm-cm^2 increase in series resistance.

Last step (i) calls for the 15 wire busbar technology instead of 5 busbars which is now commercially available . This is a similar to the approach as discussed in Chapter 5, which showed increase in efficiency with the number of busbars. This 15 wire busbar can be achieved by soldering the 15 thin copper wires onto the cells before the module lamination process [94] instead of printing silver busbars. Use of copper wires also decrease the cost of PV modules, reducing the amount of silver for metallization. This technique uses infrared heating for soldering, offering fast and effective temperature change. Sentaurus modeling in Figure 97 showed ~0.2% increase in cell efficiency due to 0.6% higher FF resulting from 0.12 ohm-cm^2 decrease in series resistance.

8.3 Conclusion

In this chapter, first a 20.6% commercial size ion implanted PERC cell with 90 ohm/sq homogeneous emitter and 50um wide screen printed gridlines was fabricated and characterized to extract parameters for modeling. Then, Sentaurus 2D device modeling was performed to develop PERC efficiency roadmap by the best way to raise cell efficiency. This modeling was then extended to develop a technology roadmap to raise the baseline 20.6% PERC solar cell efficiency to 23% using practical and manufacturable technology innovations. It was toward that this can be accomplished by advanced technologies including floating busbars, selective emitter by etch-back process, advanced screen printing (narrower busbar and gridlines), charge injection for field effect passivation, higher bulk lifetime, and plated contacts with self-aligned selective emitter. Target values and design of selective emitter, bulk lifetime, contacts and passivation quality were established target values for achieving 23% efficiency. According to the Sentaurus 2D device modeling, floating busbar, charge injection and selective emitter by etch-back process can increase absolute efficiency by 0.1%, 0.1% and 0.3%, respectively, mainly due to decrease in saturation current density (J_o) and removal of shunt mechanisms. Implementation of narrower gridlines (30um) and busbars (0.5mm) by enhanced screen printing technology can increase absolute efficiency by another 0.4% and 0.2%, respectively, due to reduced shading and contact recombination losses. Formation of void free and thicker local Al-BSF (7um), higher bulk lifetime (2ms), self-aligned selective emitter (13/130 ohm/sq) with plated contacts and 15 wire busbar technology (165um width) can increase absolute efficiency by 0.1%, 0.6%, 0.4% and 0.2%, respectively, due to decrease in saturation current density (J_o) and series resistance. These innovations can lead to commercial ready PERC cell efficiency of 23%.

CHAPTER IX

TASK 6: FABRICATION AND ANALYSIS OF HIGH EFFICIENCY LID-FREE IN-DOPED PERC SOLAR CELLS

Silicon solar cells on boron-doped Czochralski (Cz) wafers are known to lose some efficiency by light-induced degradation (LID) during the operation due to the formation of boron-oxygen (B-O) complexes in the bulk [47–51]. These defects can degrade absolute cell efficiency by 0.2∼0.7% for baseline type cells with full Al-BSF. In the case of advanced high efficiency cell structures, such as PERC, the effect of LID on efficiency can approach or exceed 1% because bulk lifetime degradation due to B-O complexes can also mitigate the benefit of superior back surface passivation in these devices [12]. Since B-O complexes are the source of LID, it can be reduced or eliminated by choosing n-type material, reducing oxygen and boron concentrations in the starting wafers, deactivating B-O complexes once they are formed or replacing boron (B) dopant by gallium (Ga) or indium (In) to prevent the formation of B-O defects. Considerable research has been performed on n-type solar cells, reduction of oxygen [52], deactivation of B-O complexes with hydrogen by high intensity illumination at high temperature [53,95,96] and introduction of Ga as dopant [48,54,97–99]. However, very little is known about the performance potential of commercial size In-doped Si solar cells and their LID response [55,98,100,101]. Although introducing In dopant as an alternative to B is similar to using Ga dopant, In dopant may be advantageous due to potential of impurity photovoltaic effect (IPV) [27, 102, 103] but may have some disadvantage due to deeper In dopant level and presence of inactive In. This task reports on the investigation of performance of large area In-doped screen-printed

full Al-BSF as well as advanced PERC cells before and after prolonged illumination, and its comparison with the counterpart B-doped cells.

9.1 Experimental Approach and Design

In this study, 3.6 ohm-cm and 6.4 ohm-cm In-doped ingots and a 6.2 ohm-cm B-doped Cz ingot were grown at SunEdison corporation by a continuous Cz (CCz) method in the same Cz puller [100]. Continuous Cz growth involves continuous feeding of the controlled amount dopant and silicon into the crucible during crystal growth so multiple Cz ingots can be grown from one crucible. This concept reduces cost and increases throughput. In addition, uniform doping profile over the entire ingot can be achieved by compensating for the segregation effect. For comparison, a commercial grade 239 cm^2 B-doped Cz material (2 ohm-cm) grown by standard Cz growth method was also included in this study. Area of all the continuous Cz wafers was 242.22 cm^2, little larger than the standard Cz wafer. Industry standard baseline cells with full Al-BSF as well as PERC cells (Figure 103) were fabricated and analyzed before and after 0.8 Sun 48-hour illumination at 37°C to quantify the impact of LID. This condition was found to be sufficient to complete the LID process for maximum degradation. Both cells had ion-implanted phosphorus emitter capped with PECVD SiNx AR coating on the front.

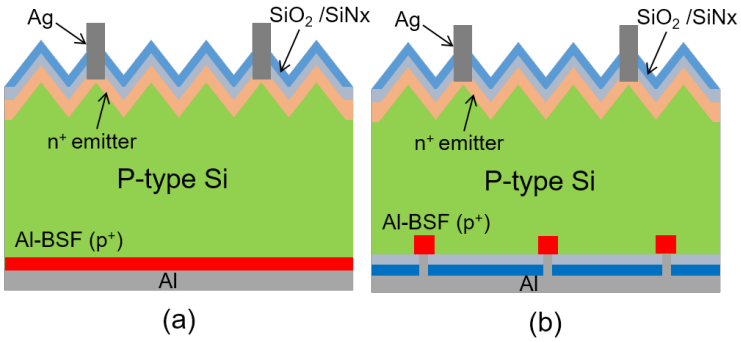

Figure 103: Structures of (a) full Al-BSF cell and (b) PERC cell.

In order to improve the fundamental understanding of the difference in properties

of B- and In-doped cells, four different test structures (Figure 104) were fabricated to determine un-metallized emitter saturation current density J_{oe}, back surface recombination velocity (BSRV, S), bulk lifetime and implied V_{oc} (iV_{oc}). J_{oe}, BSRV and iV_{oc} were measured and extracted by the well established Quasi-Steady-State Photoconductance (QSSPC) technique [29, 104] after subjecting them to the contact firing cycle without metal because this measurement can only be performed on unmetallized structures. Bulk lifetime in the as-grown silicon wafer was also measured by QSSPC tool after saw damage removal and liquid iodine-methanol surface passivation during the measurement which eliminates the impact of surface recombination [105].

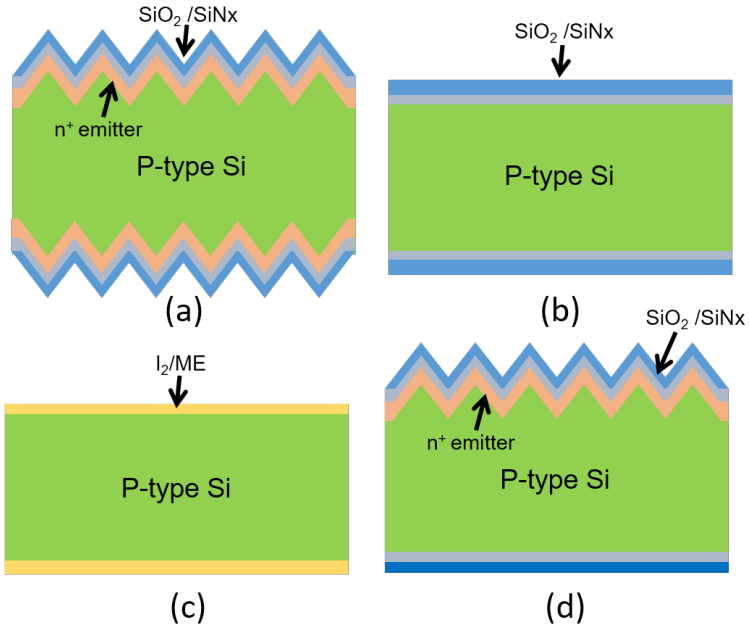

Figure 104: Test structures for (a) J_{oe} (b) SRV and J_{ob}' (c) bulk lifetime, and (d) implied V_{oc} (iV_{oc}).

The light IV data and cell efficiency were measured using a secondary Fraunhofer calibrated cell. After the initial IV characterization, some cells from each group were placed under a halogen lamp for 48 hours at ∼0.8 suns and 37°C for LID evaluation. Internal quantum efficiency measurements were performed in the wavelength range of 350nm∼1200nm, in addition to photoluminescence (PL) measurements with a 808

nm laser using LIS-R2 tool of BT Imaging system on the finished cells to characterize the change in recombination activity over the entire cell including bulk emitter and surface recombination.

9.2 Results and Discussion

9.2.1 Material characteristics

Table 22 shows resistivity and bulk lifetime of the four different In- and B-doped wafers used in this study. Measured as-grown bulk lifetimes were 459 us, 1171 us, 264 us and 1738 us for the 3.6 ohm-cm In-, 6.4 ohm-cm In-, 2 ohm-cm B-, and 6.2 ohm-cm B-doped wafers, respectively. Note that the higher resistivity In-doped wafer (6.4 ohm-cm) showed lower bulk lifetime compared to the similar resistivity (6.2 ohm-cm) B-doped wafer. Oxygen concentrations measured by FTIR spectroscopy in these wafers are also shown in Table 22. Since both the In-doped ingots and 6.2 ohm-cm B-doped ingot were grown by CCz method, the oxygen concentration and resistivity did not vary much ($\leq$10%) from seed to tail end of these ingots, even though indium has much lower segregation coefficient (4e-4) than boron (0.8) [100]. Also, In-doped ingot showed relatively flat axial resistivity gradient (<30%) by the CCz method [100].

Table 22: Measured Resistivity, Bulk Lifetime, and Oxygen Concentration.

Wafer Area (cm^2)	Dopant Type	Resistivity (Ω-cm)	Lifetime (us) @1e15cm^{-3}	Oxygen (ppm)
242.22	Indium	3.6	459	12
242.22	Indium	6.4	1171	13
239	Boron	2	264	18
242.22	Boron	6.2	1738	13

9.2.2 Comparison of In- and B-doped baseline solar cells with full Al-BSF

Table 23 shows the cell efficiency of In- and B-doped baseline cells with full Al-BSF. It is interesting to note that the baseline cells on all four materials gave ~19.2% efficiency regardless of the as grown lifetime and resistivity differences. This is because

baseline cell efficiency is not a strong function of bulk lifetime once it exceeds 200 us. After diffusion length exceeds about 2-3times the cell thickness cell performance becomes dominated by higher back surface recombination velocity (BSRV $\geq$300 cm/s) of the full Al-BSF cell. In the PERC cells, BSRV is <50cm/s due to dielectric passivation therefore lifetime is more important even beyond 300 us.

Table 23: Average and Best Cell Efficiency of Full Al-BSF Cells on In- and B-doped Wafers.

Wafer Type		V_{oc} (mV)	J_{sc} (mA/cm^2)	FF(%)	Efficiency (%)
In	Best	646	38.0	78.7	19.3
(3.6 Ω-cm)	AVG (6)	643	38.1	78.5	19.2±0.03
In	Best	645	38.0	78.6	19.3
(6.4 Ω-cm)	AVG (5)	645	38.1	78.2	19.2±0.03
B	Best	648	37.9	79.0	19.4
(2 Ω-cm)	AVG (4)	647	37.7	78.9	19.2±0.11
B	Best	648	38.2	78.5	19.4
(6.2 Ω-cm)	AVG (6)	648	38.0	78.4	19.3±0.10

Table 24 summarizes the cell data before and after the LID (~0.8 sun and 48 hours) which show that low and high resistivity B-doped cells suffered an appreciable loss of 0.7% and 0.2% in absolute efficiency, respectively. This is consistent with the measured boron and oxygen concentrations in these wafers because higher B and O concentrations are expected to result in more LID. In contrast to the B-doped Cz cells, In-doped cells showed no appreciable loss in cell efficiency ($\leq$0.1%) due to LID regardless of the base resistivity. In doped cells showed $\geq$ 0.4% higher absolute efficiency after LID compared to the 2 ohm-cm B-doped cells which are widely used in industry today. This endorses the strong potential of In-doped Cz Si for high stabilized efficiency.

Table 24: Measured Light I-V Data of Full Al-BSF Cells on In- and B-doped Wafers Before and After LID.

Wafer Type		V_{oc} (mV)	J_{sc} (mA/cm^2)	FF(%)	Efficiency (%)
In	Initial	640	38.1	78.7	19.2
(3.6 Ω-cm)	LID	641	38.1	78.4	19.1
In	Initial	642	38.0	78.0	19.0
(6.4 Ω-cm)	LID	644	38.1	77.6	19.0
B	Initial	644	37.7	79.5	19.3
(2 Ω-cm)	LID	637	37.4	78.4	18.6
B	Initial	648	38.1	78.4	19.3
(6.2 Ω-cm)	LID	647	38.1	77.3	19.1

9.2.3 Comparison of ≥20% efficient In- and B-doped PERC solar cells

9.2.3.1 Comparison of In- and B-doped PERC Cells Prior to LID Test

Table 25 shows average and best efficiency for PERC cells fabricated on In- and B-doped wafers. In each group ∼10 cells were fabricated for this study.

Table 25: Average and Best Cell Efficiency of PERC Cells on In- and B-doped Wafers.

Wafer Type		V_{oc} (mV)	J_{sc} (mA/cm^2)	FF(%)	Efficiency (%)
In	Best	656	39.2	78.6	20.2
(3.6 Ω-cm)	AVG (10)	656	39.1	78.3	20.1±0.11
In	Best	657	38.8	79.4	20.3
(6.4 Ω-cm)	AVG (7)	659	39.0	78.1	20.1±0.16
B	Best	664	39.0	79.8	20.6
(2 Ω-cm)	AVG (10)	663	39.0	79.2	20.5±0.15
B	Best	667	39.1	78.5	20.5
(6.2 Ω-cm)	AVG (7)	665	39.0	78.1	20.3±0.11

Unlike the baseline cells, where initial cell efficiencies on all four materials were very similar, there was a noticeable difference in the pre-LID efficiencies of PERC cells because these cells are more sensitive to bulk lifetime and surface passivation differences. In PERC cells, BSRV is much lower and back surface reflectance (BSR)

is higher due to dielectric, therefore, PERC cell efficiencies are superior ($\geq$20%) to baseline cells. In-doped PERC cells gave best efficiency of 20.3% which was lower compared to 20.6% and 20.5% efficient B-doped PERC cells on low and high resistivity materials. Table 25 shows that this is largely due to 6-10mV lower V_{oc} of the In-doped cells.

To investigate the reason for the observed difference between V_{oc} and efficiency of the 6.2 ohm-cm In and B-doped cells, un-metallized emitter and base saturation current densities (J_{oe} and J_{ob}) and bulk lifetime (τ_{bulk}) were determined using the three test structures shown in Figure 104. The first structure in Figure 104a gives un-metallized Joe value. The second structure (Figure 104b) gives effective bulk lifetime (τ_{eff}) including the bulk and back surface recombination velocity (S), and the third test structure (Figure 104c) gives true bulk lifetime (τ_{bulk}) because of the excellent surface passivation provided by iodine-methanol(I_2/ME) solution. Next, the following Equation,

$$\frac{1}{\tau_{eff}} = \frac{1}{\tau_{eff}} + \frac{2S}{W}, \tag{32}$$

was used to extract back surface recombination velocity (S) from the measured wafer thickness W, τ_{eff} and τ_{bulk} values [29, 90, 106], summarized in Table 26.

Table 26: Calculated S from Measured τ_{eff} and τ_{bulk} on the Test Structure in Figure 104b.

Wafer Type	Indium 6.4 Ω-cm	Boron 6.2 Ω-cm
τ_{bulk} (us)	716	762
τ_{eff} (us)	323	529
W (um)	140	140
S (cm/s)	12	4

Note that BSRV for In-doped sample was three times higher than B-doped sample

(12 vs 4 cm/s). Once BSRV (S), bulk lifetime or diffusion length (Ln), base doping (N_A) and wafer thickness (W) are known, J_{ob} was calculated from the following Equation 33 [23],

$$Job = \frac{q{n_i}^2 Dn}{N_A Ln} * \frac{S\cosh(W/Ln) + (Dn/Ln)\sinh(W/Ln)}{(Dn/Ln)\cosh(W/Ln) + S\sinh(W/Ln)}. \quad (33)$$

Since emitters were formed simultaneously, measured J_{oe} (Figure 104) was found to be similar (65-69fA/cm^2) for B- and In-doped samples (Table 27). However, Table 22 showed that the bulk lifetime of the In-doped sample was much lower (1171 us vs 1738 us) and BSRV of the In-doped cell was much higher (12 cm/s vs 4 cm/s) compared to the counterpart B-doped cells. As a result, the extracted un-metallized J_{ob} value from Equation (33) was found to be 145 fA/cm^2 for the In-doped device compared to 80 fA/cm^2 for the B-doped device. Using these un-metallized J_{oe} and J_{ob} values and a J_{sc} of 39mA/cm^2, implied V_{oc} or iV_{oc} for the In- and B-doped devices was calculated from the following Equation,

$$iV_{oc} = \frac{KT}{q}\ln\left(\frac{J_{sc}}{J_{oe} + J_{ob}} + 1\right). \quad (34)$$

Table 27: Comparison of Measured and Calculated iV_{oc} from J_{oe} and J_{ob} for Indium and Boron Doped Cells.

Wafer Type	Indium 6.4 Ω-cm	Boron 6.2 Ω-cm
J_{oe} (fA/cm^2)	69	65
S (cm/s)	12	4
τ_{ob} (fA/cm^2	982	1331
J_{ob} (fA/cm^2)	145	80
Calculated iV_{oc} (mV)	666	676
Measured iV_{oc} (mV)	670	678
Measured V_{oc} (mV)	659	665

In addition, iV_{oc} was directly measured using the test structure in Figure 104d. Table 27 shows that the measured and calculated iV_{oc} values for B- and In-doped samples agreed very well (±4mV). Table 27 also shows that the difference between the iV_{oc} (8-10mV) of the two devices was similar to the difference between the measured V_{oc} values of the finished In- and B-doped cells (Table 25). This analysis also shows that metal induced recombination from screen printed metallization reduced V_{oc} by ~10mV, which is the difference between iV_{oc} and cell V_{oc}. Lower bulk lifetime in In-doped devices can be explained by a recent study conducted by Binn et al [100], which showed that there is a large fraction of inactive or unionized indium atoms in the In-doped wafers (Figure 105).

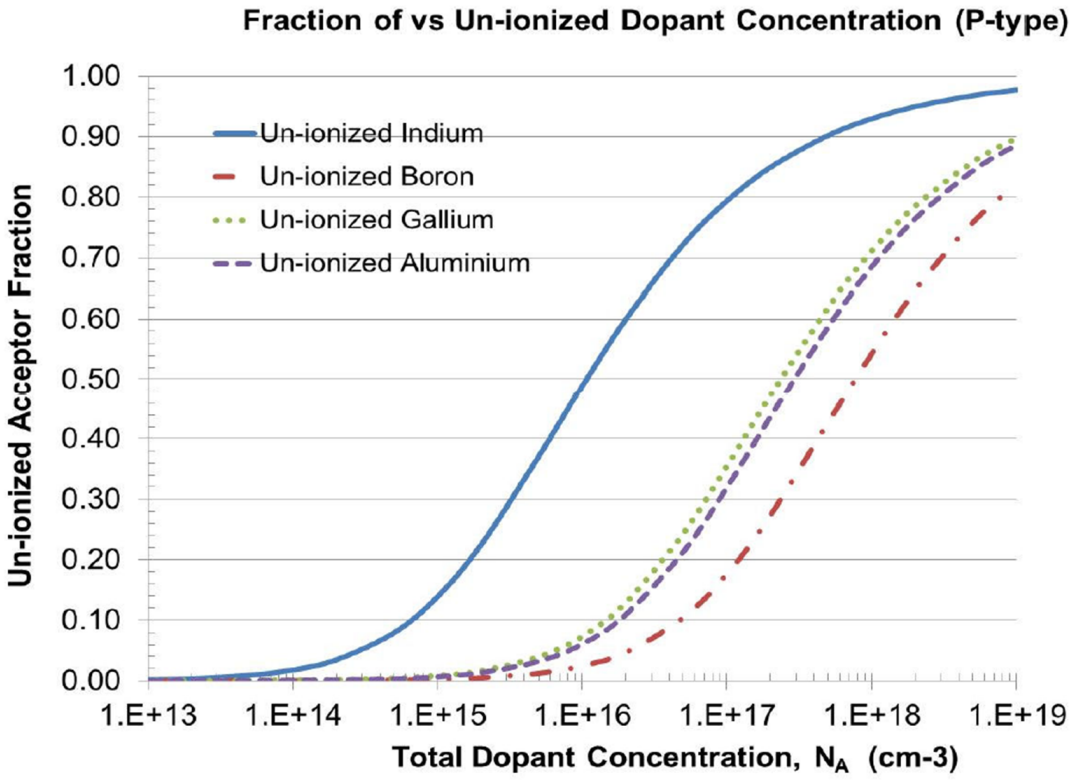

Figure 105: Un-ionized acceptor fraction as a function of total acceptor concentration for boron, gallium, aluminum and indium [100].

They also demonstrated that the inactive indium forms a recombination center to reduce bulk lifetime. It is possible that the presence of inactive indium on the back

surface may also be responsible for the observed higher S and J_{ob} values for In-doped cells compared to the B-doped cells. Note that higher S value was observed even on the as-received unprocessed In-doped wafers compared to B-doped wafers (4 vs 2 cm/s) passivated with I_2/ME solution during lifetime measurements (Figure 104c). Since the key difference in the pre-LID performance came from the difference in τ_{bulk} and S, photoluminescence (PL) measurements were performed on the finished In- and B-doped cells using 808nm laser to see the combined effect of bulk and surface recombination over the entire cell area. PL images in Figure 106 clearly show an appreciable difference in the effective lifetime of the two devices with In-doped cell showing an inferior PL response. Since at this time the pre-LID cell efficiency is higher for B-doped cells than In-doped cells, if LID can be prevented in B-doped cells by deactivation of B-O defects using a rapid high intensity illumination at elevated temperature [53, 95, 96], B-doped cells could give higher stabilized cell efficiency than the In-doped cells.

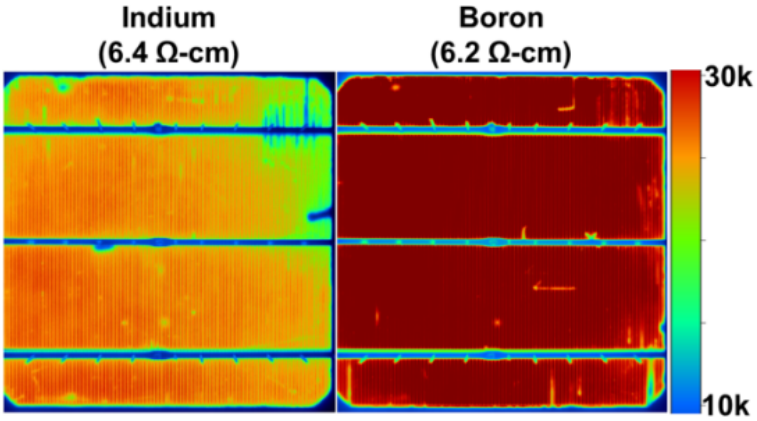

Figure 106: Photoluminescence images of the In- and B-doped PERC cells before LID.

9.2.3.2 Quantitative Comparison of LID in In- and B-doped Cells

This section compares the post LID performance of the PERC cells on four groups of material after they were subjected to 48 hours, 0.8 sun illumination at 37°C. Table

28 summarizes the impact of LID on the PERC cell parameters.

Table 28: Efficiency of In- and B-doped Cells Before and After LID.

Wafer Type	AVG (3)	V_{oc} (mV)	J_{sc} (mA/cm^2)	FF(%)	Efficiency (%)
In	Initial	650	39.1	78.4	20.0±0.08
(3.6 Ω-cm)	post LID	656	38.9	78.3	20.0±0.11
In	Initial	655	39.0	78.3	20.0±0.03
(6.4 Ω-cm)	post LID	660	39.0	78.1	20.1±0.05
B	Initial	659	39.0	79.1	20.4±0.12
(2 Ω-cm)	post LID	651	38.6	77.7	19.5±0.30
B	Initial	662	39.0	78.2	20.2±0.19
(6.2 Ω-cm)	post LID	663	38.9	76.9	19.8±0.15

Notice that there was no degradation in the In-doped PERC cell efficiency after the LID regardless of the base resistivity. In fact, a slight improvement was observed in V_{oc} of the In-doped PERC cells after the LID test. This is consistent with reference[13], which showed that effective lifetime of In-doped wafer may slightly increase after light exposure due to light-induced dissociation of Fe-In pairs if present in the wafer. This is because Fe-In pairs have higher electron and hole capture cross sections (σ_n- 3.5x10^{-13} cm^2, σ_p- 1.5x10^{-14} cm^2) than the dissociated Fei (σ_n- 4x10^{-14} cm^2, σ_p- 7x10^{-17} cm^{17}) [98]. Since the dissociated indium dopants remain on the substitutional sites [98], they do not contribute to the recombination centers. In contrast, B-doped PERC cells showed significant drop in cell efficiency from 20.4% to 19.5% and from 20.2% to 19.8% for the low and high resistivity B-doped wafers, respectively. This is because of the bulk lifetime degradation resulting from the formation of B-O complexes which act as recombination centers [12,47–51]. As expected, higher boron concentration produces greater LID. This was also further confirmed by the IQE measurements before and after LID on lower resistivity In- and B-doped cells.

Figure 107 shows that B-doped PERC cell showed appreciably lower long wavelength response after LID but the In-doped cells remained unaffected. As expected, LID impact was greater in the B-doped PERC cells compared to the full Al-BSF baseline cells because PERC cells are more sensitive to bulk lifetime. It is also important to note that in spite of slightly lower starting efficiency, the final stabilized efficiency of In-doped PERC cells after LID was decisively superior to the B-doped PERC cells.

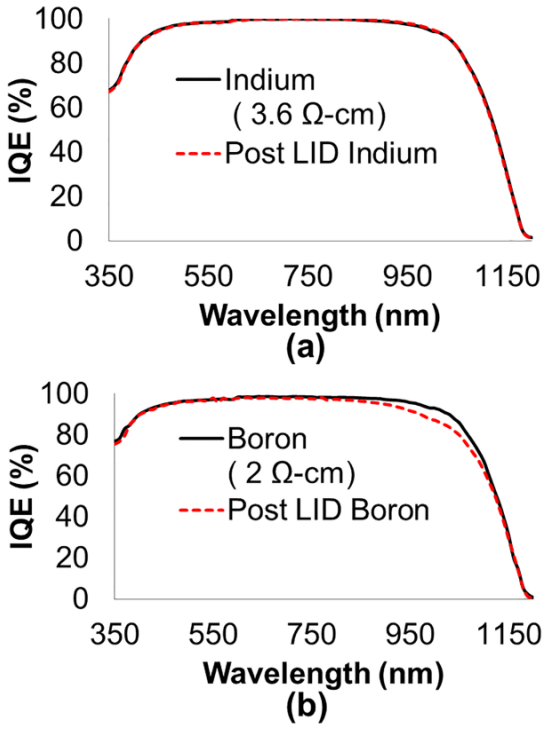

Figure 107: IQE measurements of PERC cells on (a) In- and (b) B-doped wafers before and after LID.

9.3 Conclusion

We demonstrated 20.3% efficient large-area screen-printed In-doped Cz PERC cells with no LID. Prior to LID, In- and B-doped baseline cells with full Al-BSF gave nearly identical efficiencies (19.2%). However, In-doped PERC cells gave 0.2 - 0.4% lower efficiency compared to the B-doped PERC cells due to lower bulk lifetime and higher BSRV. This is attributed to inactive or unionized indium atoms which can form recombination centers. After the LID at $\sim$0.8 sun illumination for 48 hours at 37°C, low and high resistivity B-doped cells showed 0.9% and 0.4% efficiency degradation, respectively. In contrast, In-doped cells showed no loss in performance after the illumination. Thus, in spite of slightly lower starting efficiency, In-doped PERC cells surpassed the B-doped PERC cell efficiency by 0.3 $\sim$ 0.5% after LID. This shows the promise of In-doped cells for higher stabilized efficiency, which makes them on attractive candidate for PV applications.

CHAPTER X

TASK 7: UNDERSTANDING AND DEVELOPMENT OF REGENERATION TREATMENT TO ELIMINATE LID IN B-DOPED CELLS

Although In-doped PERC cells were found LID-free in the previous Chapter, In-doped wafers are not readily available for production yet. Boron-doped cells still dominate the silicon solar cell market. Therefore, the goal of this task was to eliminate LID in B-doped cells by deactivating or preventing the formation of B-O complexes by a regeneration treatment, which involves light and heat. Since boron-doped wafers showed higher bulk lifetime than indium doped wafers, regeneration process should lead to higher stabilized efficiency for B-doped PERC solar cells.

Recently, a few research groups have reported on a regeneration phenomenon which appears to deactivate or passivate B-O complexes [53, 95, 96, 107–112]. Figure 108 shows three well known states of the metastable boron-oxygen complex with its paths.

Table 29 shows thermal activation energy for each path in Figure 108.

Table 29: Thermal Activation Energy E_A.

	E_A (eV)
Annealing	∼1.3 [47, 113]
Degradation	∼0.4 [114, 115]
Regeneration	∼1.0 [109]
Destabilization	∼1.25 [109]

The exact mechanism for regeneration process is not fully understood but it has been suggested that two factors are involved in the regeneration process: carrier injection by light and high temperature (≥65°C) to promote hydrogen passivation of

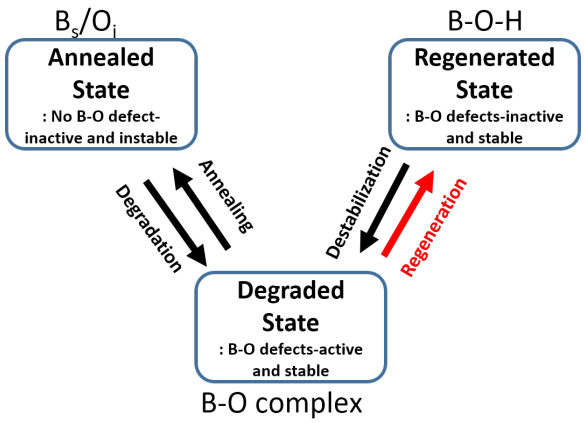

Figure 108: Three states of the metastable boron-oxygen complex: annealed, degraded and regenerated states [95, 110].

defect [53, 95, 96]. According to Wilking′s and Hahn′s model [53], combination of carrier injection and high temperature lowers the barrier for dissociation of hydrogen which is bound to impurities in the bulk Si, and in the case of B-H pairs, the dissociation energy decreases from ∼1.76eV to ∼1.0eV. This dissociated hydrogen also changes its charge state from H+ to H0 under the carrier injection and high temperature, and moves toward light-induced B-O defects to passivate them. Previous research also showed excellent long-term stability of the regenerated state with high destabilization energy of ∼1.25eV which translates into destabilization time constants of >8800 years at 25°C and >53 years at 60°C [109]. Some reports demonstrate nearly 100% regeneration [112] while others show only ∼95% or less [107,108] and this difference has been attributed to sub-optimum regeneration conditions or different amount of mobile hydrogen available to passivate the B-O complexes.

Since regeneration is a relatively new concept, there is only limited data in the literature that quantifies and compares performance of commercial size ($239cm^2$) high-efficiency screen printed full Al-BSF baseline and PERC cells before and after LID and regeneration [111, 112]. Therefore, in this task, we evaluated LID before and after regeneration process and also tested different regeneration conditions to achieve

full stabilization. Detailed characterization and analysis of regenerated boron-doped cells were performed to improve the fundamental understanding of the regeneration phenomenon and explain the difference between LID and regeneration behavior in the above two dominant cell structures in production today.

10.1 Design of Experiment for Regeneration Process

In this study, commercial grade 2 ohm-cm B-doped Cz wafers were used with 18 ppm of oxygen concentration. Commercial ready large area (239 cm^2) high efficiency screen printed full Al-BSF cells as well as high efficiency PERC cells with local Al-BSF were fabricated (Figure 103 in chapter IX). In this study, both cell structures had same emitter and SiO_2/SiNx passivation on the front. The only difference was the local back surface field and SiO_2/SiNx passivation on the back of the PERC cell as opposed to full Al-BSF in the baseline cell. These cells were subjected to (a) 48-hour LID at 37°C under 0.8 sun, (b) 30-second regeneration at 200°C under 3 suns, (c) 48-hour regeneration at 75°C under 1 sun and (d) 1.5-hour regeneration at 130°C under 2 suns to quantify and understand their LID and regeneration properties. Since degradation, regeneration and destabilization are all thermally activated processes (Table 29), higher the temperature faster the process. Since activation energy for regeneration is lower than destabilization, 1eV vs 1.25eV, it is possible to find an optimum temperature at which regeneration dominates without triggering destabilization. This is why regeneration temperatures in the range of 75-200°C were chosen.

The light IV (LIV) data including cell efficiency was obtained using a secondary Fraunhofer calibrated cell. After pre-LID characterization of all the cells, extent of LID was determined in both full Al-BSF and PERC cell structures by placing them under a halogen lamp for 48 hours at 37°C with 0.8 sun illumination. A second set of samples were first subjected to regeneration process under 3 suns illumination at

200°C for 30 seconds followed by the same 48-hour LID at 37°C and 0.8 sun. Such high temperature regeneration condition (200°C) speeds up the stabilization process but may also triggers destabilization and annealing paths (annealed and degraded states in Figure 108) which have higher activation energies (1.25 and 1.3 eV). Competition between the three processes will dictate the degree of stabilization. A third experiment was carried out by subjecting the baseline and PERC cells to a slower regeneration process involving 1 sun illumination for 48 hours at 75°C followed by 48-hour LID at 37°C with 0.8 sun. 75°C slows down the regeneration process but may avoid the formation of annealed and degraded states due to higher thermal activation energies (Table 29). Because of slow regeneration of 75°C, regeneration time was increased to 48 hours. Finally, a fourth experiment was performed by choosing an intermediate temperature (130°C at 2 suns) to achieve medium regeneration speed. This regeneration time was selected to be 1.5 hours to achieve max stabilization without too much destabilization and annealing. Light IV and internal quantum efficiency (IQE) measurements were performed to characterize the changes in key cell parameters including V_{oc}, J_{sc}, FF, efficiency and recombination activity.

10.2 Impact of LID and Three Different Regeneration Conditions on Full Al-BSF and PERC cells

10.2.1 Light-induced degradation (LID) in full Al-BSF and PERC cells prior to regeneration

In this study, large area PERC and full Al-BSF cells were fabricated and exposed to 0.8 sun illumination at 37°C to trigger the LID process, without any prior regeneration treatments. LID time was varied from 0 to 48 hours and the cell parameters were measured as a function of time (Table 30).

Table 30: Measured Average LIV Data of Full Al-BSF and PERC Cells After LID

Average of ()	LID Hours	Voc (mV)	Jsc (mA/cm^2)	FF (%)	Efficiency (%)
PERC (4)	0	664	39.0	78.9	20.4±0.10
	5	656	38.7	77.8	19.8±0.22
	24	653	38.7	77.5	19.6±0.26
	48	651	38.7	77.4	19.5±0.24
Full Al-BSF (4)	0	643	37.6	79.4	19.2±0.09
	5	639	37.4	78.6	18.8±0.12
	24	636	37.3	78.4	18.6±0.15
	48	635	37.4	78.4	18.6±0.06

Initial average cell efficiencies were 20.4% and 19.2% for the PERC and full Al-BSF cells, respectively. After 48 hours of LID, cell efficiency dropped to 19.5% and 18.6% for PERC and full Al-BSF cells due to the formation of B-O complexes [50,51,99,116]. PERC cells showed about 13mV drop in Voc, 0.3 mA/cm^2 decrease in Jsc with appreciable reduction in FF from 78.9% to 77.4%. As expected, full Al-BSF baseline cell showed smaller degradation with only 9mV decrease in Voc, 0.2mA/cm^2 drop in J_{sc} along with reduction in FF from 79.4% to 78.4%. As a result, full Al-BSF cells showed 0.6% efficiency degradation compared to 0.9% for the PERC cells even though both structures were fabricated on the same material (7e15 $atoms/cm^{-3}$ boron and 18 ppm oxygen). This is because the benefit of superior back surface passivation of PERC cells is also eroded by significant reduction in diffusion length after LID. In order to support this hypothesis, device modeling (using PC1D) was performed which showed greater absolute efficiency drop in a PERC structure for the same decrease in bulk lifetime (Figure 109). This PERC cell performance is more sensitive to bulk lifetime.

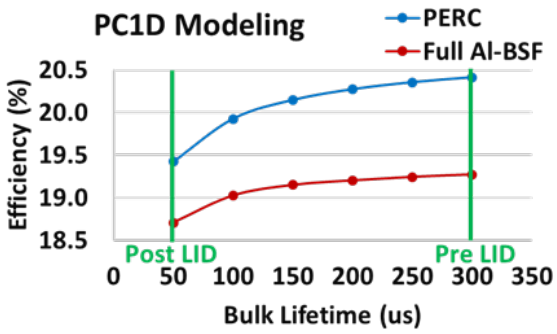

Figure 109: PC1D modeling for PERC and full Al-BSF cells as a function of bulk lifetime.

10.2.2 Impact of LID on Full Al-BSF and PERC Cells After a Prior Regeneration Treatment at 200°C for 30 Seconds Under 3 Suns

In this study, both full Al-BSF and PERC cells were first subjected to 30-second regeneration at 200°C at 3 suns followed by 48-hour LID at 37°C and 0.8 sun. This condition was used to accelerate the regeneration process and increase the throughput in mass production. Table 31 summarizes LIV data of full Al-BSF and PERC cells before and after regeneration followed by LID.

Table 31: Measured LIV Data of Full Al-BSF and PERC Cells After 200°C/3 sun/30s Regeneration and LID

Average of ()	Step	Voc (mV)	Jsc (mA/cm^2)	FF (%)	Efficiency (%)
PERC (5)	Initial	663	39.0	78.6	20.3±0.14
	Regeneration	663	39.0	78.4	20.3±0.17
	LID	662	39.0	78.3	20.2±0.18
Full Al-BSF (3)	Initial	643	38.0	78.6	19.2±0.11
	Regeneration	643	37.9	78.7	19.2±0.17
	LID	640	37.8	78.3	18.9±0.10

Table 31 shows that regeneration treatment itself had no appreciable effect on cell parameters and efficiency but a very significant impact on LID after regeneration. Contrary to the previous experiment, LID after this regeneration cycle showed only 0.1% decrease in absolute efficiency of the PERC cell as opposed to 0.9% drop in the absence of this regeneration treatment (Table 30). This is because during the

regeneration process B-O complexes are formed but are quickly passivated by mobile H0 created by dissociation of hydrogen impurity complexes (like B-H) under light and heat [53]. Since hydrogen passivated B-O complexes are stable under LID conditions, no appreciable degradation is observed for PERC. Also, notice that there was virtually no reduction in Voc and Jsc after regeneration + LID and only FF showed a small decrease to account for the observed 0.1% degradation in efficiency. Exact reason for this is not fully understood at this time but can be attributed to few non-regenerated B-O complexes which are also known to cause or increase injection level dependence of lifetime [117]. This is supported by measured effective lifetimes as a function of injection level for the same cell after initial, post regeneration and post LID conditions in Figure 110. Since this lowers the effective lifetime at V_{max} (1e13-1e14 cm^{-3} injection level) compared to effective lifetime at V_{oc}, V_{oc} remains unaffected much but the I-V curve becomes less square degrading the FF.

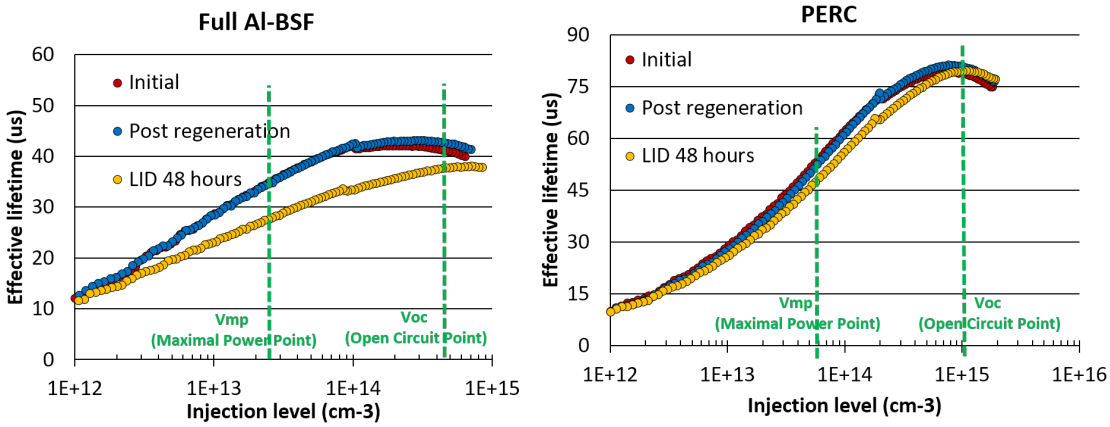

Figure 110: Measured effective lifetimes as a function of injection level on full Al-BSF and PERC cells - regeneration and LID.

Full Al-BSF cells also showed the benefit of this regeneration treatment prior to LID but the positive impact of this regeneration condition was much less, resulting in 0.3% degradation in absolute cell efficiency after LID as opposed to 0.6% without the regeneration treatment (Table 31). Thus, this regeneration process improves the LID

behavior of the PERC cells very significantly but it does not completely eliminate the LID effect. The regeneration is more effective in the PERC cells due to higher injection level, superior BSRV, and higher hydrogen supply from double side SiNx deposition [111].

10.2.3 A Study of Sequential Regeneration and LID Treatments

Table 32 shows the measured LIV data for several consecutive 30-second regeneration (3 suns at 200°C) and 48 horus LID (0.8 sun at 37°C) cycles to see the change in the LID characteristics.

Table 32: Measured LIV Data of Full Al-BSF and PERC Cells after Consecutive Regeneration (200°C/3 suns/30s) and LID Cycles

	Step	Voc (mV)	Jsc (mA/cm^2)	FF (%)	Efficiency (%)
PERC	Initial	664	38.9	78.0	20.2
	Regeneration	664	38.8	78.4	20.2
	LID	664	38.8	77.8	20.0
	Regeneration	664	39.0	78.2	20.2
	LID	662	38.9	77.8	20.0
Full Al-BSF	Initial	642	37.9	78.7	19.2
	Regeneration	643	37.6	79.1	19.1
	LID	640	37.4	78.5	18.8
	Regeneration	641	37.7	79.3	19.2
	LID	640	37.5	78.5	18.8

In this study, starting PERC cell efficiency was 20.2% which remained same after the regeneration treatment but dropped to 20.0% after the subsequent LID due to the FF loss. Subsequent regeneration treatment restored the cell efficiency back to 20.2% but it again dropped to 20.0% after the LID. Thus, this regeneration condition is not able to achieve 100% stabilization in our PERC cells. Partial regeneration at 200°C can be attributed to insufficient amount of mobile hydrogen or same destabilization via dissociation of some B-O complexes or regenerating back to the annealed state (Figure 108 and Table 29). Full Al-BSF cells showed a similar pattern but with much higher efficiency degradation (0.3%∼0.4%).

10.2.4 Understanding the Impact of Slower Regeneration at 75°C Under 1 Sun

In order to assess the significance of regeneration conditions, regeneration temperature and illumination intensity were decreased to 75°C and 1 sun, which is closer to what happens during the module operation [118]. Regeneration time was increased to 48 hours in order to make up for the slower regeneration rate. Tables 33 and 34 show measured LIV data of PERC and full Al-BSF cells for sequential LID and regeneration cycles. In this study (Table 33), pre-LID efficiencies were 20.1% and 19.1% for the PERC and full Al-BSF cells. After the first 48-hour LID at 37°C under 0.8 sun, efficiencies dropped to 19.3% and 18.5% for the PERC and full Al-BSF cells. After a subsequent 48-hour regeneration at 75°C under 1 sun, PERC and full Al-BSF cells partially regenerated to 20.0% and 18.7% with no appreciable change with subsequent LID.

Table 33: Measured Average LIV Data of Full Al-BSF and PERC Cells After LID, 75°C/1 sun/48 Hours Regeneration and LID Cycle.

Average of ()	Step	Voc (mV)	Jsc (mA/cm^2)	FF (%)	Efficiency (%)
PERC (3)	Initial	659	38.6	79.2	20.1±0.16
	LID	646	38.2	78.2	19.3±0.11
	Regeneration	658	38.6	78.9	20.0±0.12
	LID	658	38.5	78.7	19.9±0.12
Full Al-BSF (3)	Initial	644	37.3	79.7	19.1±0.05
	LID	635	36.9	78.9	18.5±0.06
	Regeneration	639	37.1	79.0	18.7±0.02
	LID	639	37.0	79.1	18.7±0.02

In Table 34, cells were first exposed to 48 hours regeneration at 75°C under 1 sun and then subjected to LID. Unlike the regeneration at 200°C, lower temperature regeneration at 75°C resulted in 0.1% efficiency drop from 20.2% to 20.1% and dropped again to 20.0% after the LID. This is probably because regeneration at 75°C

temperature also fail to convert all the B-O defects into the stable regenerated state even after 48 hours.

Table 34: Measured Average LIV Data of Full Al-BSF and PERC Cells After 75°C/1 Sun/48 Hours Regeneration Followed by LID

Average of ()	Step	Voc (mV)	Jsc (mA/cm^2)	FF (%)	Efficiency (%)
PERC (2)	Initial	662	39.1	78.2	20.2±0.25
	Regeneration	663	39.2	77.3	20.1±0.06
	LID	662	39.1	77.2	20.0±0.17
Full Al-BSF (1)	Initial	641	37.8	78.3	19.0
	Regeneration	642	37.7	77.2	18.7
	LID	639	37.9	77.3	18.7

Notice that unlike the 200°C regeneration (Tables 31 and 32), 75°C regeneration condition degraded the initial PERC cell efficiency by ∼0.1% and full Al-BSF cell efficiency by ∼0.3%. This is because LID and regeneration are competing during this 75°C regeneration cycle and regeneration is not fast enough to passivate all the defects and eliminate LID completely. Since regeneration rate is faster in PERC due to more hydrogen and higher injection level, the recovery was greater in PERC cells than in the Al-BSF cell (Table 34).

In order to understand and characterize recombination activities in these LID and regenerated cells, IQE measurements were performed on cells before and after LID and also after the regeneration followed by LID as shown in Figure 111 (Measured cells are from Table 33).

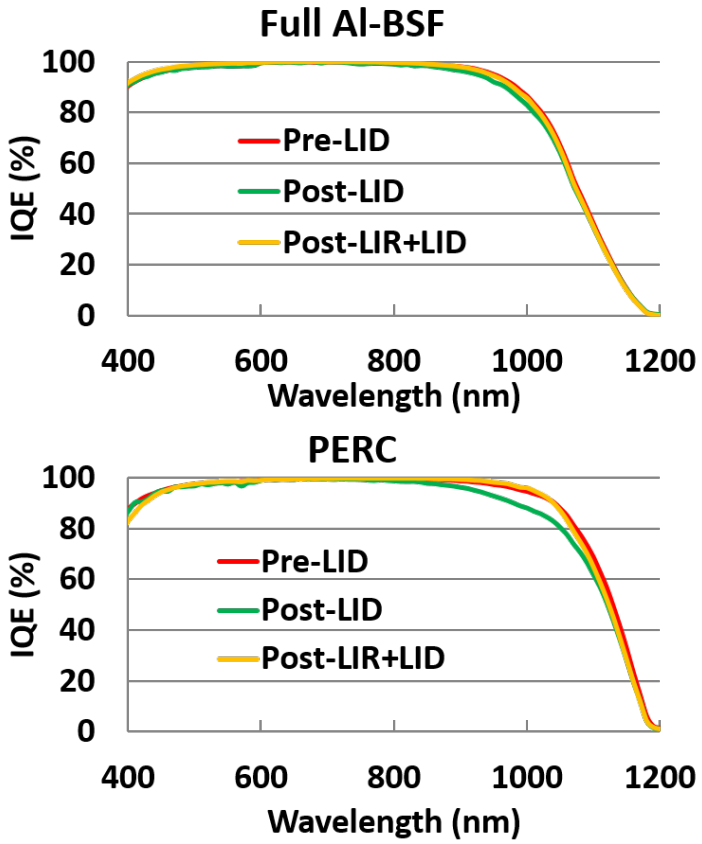

Figure 111: Measured IQE responses of pre-LID, post-LID, and post regeneration followed by LID for full Al-BSF and PERC cells.

As expected, initial LID treatment decreased IQE only in the long wavelength (800∼1100nm) range the for both cell structures due to bulk lifetime degradation. Lower bulk lifetime also makes back surface passivation opaque, mitigating the key advantage of PERC cells resulting in a bigger drop in IQE. This is why PERC cells show higher LID without any regeneration. After the 75°C regeneration process followed by LID, IQE response showed nearly full IQE recovery for both structures but the cell efficiency was not completely recovered. This is consistent with the cell data (Table 33) which showed Voc and Jsc were nearly recovered for PERC cells and the effcieincy gap was largely due to FF degradation. Figure 112 shows the relative degradation in key cell parameters after LID, with and without prior regeneration at 200°C/3 suns/30 seconds (Figure 112b).

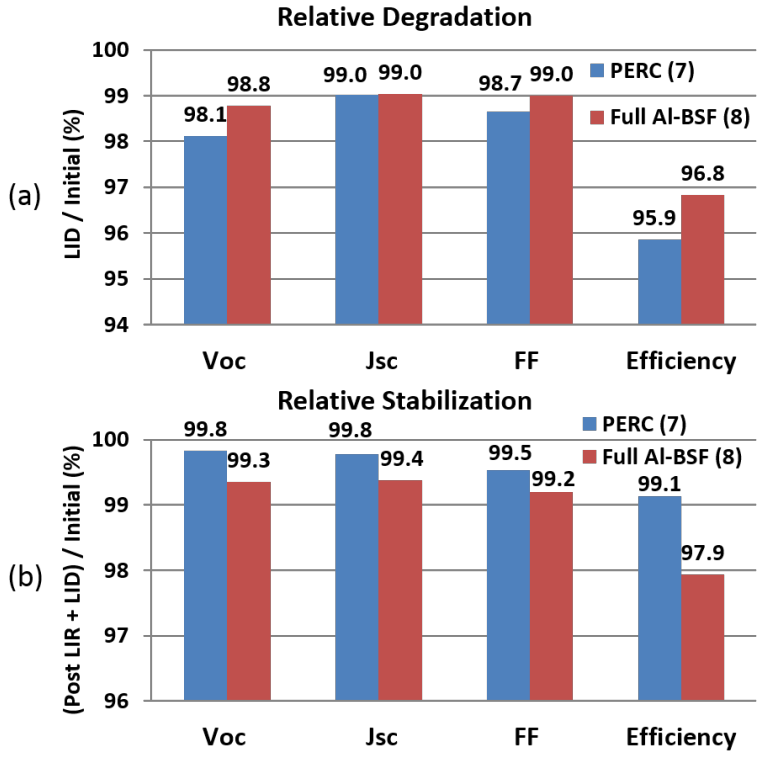

Figure 112: (a) Relative degradation after 48-hour LID at 37°C under 0.8 sun and (b) relative degradation after LID with prior regeneration at 200°C/3 suns/30s.

Without the prior regeneration treatment, PERC cells showed greater degradation in Voc, FF and efficiency after LID compared to the full Al-BSF cells (Figure 112a). However, Figure 112b shows that results are opposite if regeneration treatment is done prior to LID. This is because prior regeneration is more effective in PERC cells compared to the baseline full Al-BSF cells due to more mobile hydrogen in PERC for B-O defect passivation.

10.2.5 Full Stabilization Using Medium Speed Regeneration at 130°C Under 2 Suns

After understanding the rapid regeneration at 200°C and slow regeneration at 75°C, which did not achieve 100% stabilization. An intermediate speed regeneration condition (1.5 hours at 130°C under 2 suns) was investigated to achieve complete stabilization. This is probably because 200°C regeneration activates the destabilization

process and 75°C regeneration rate is too slow to passivate all the B-O complexes even after 48-hour regeneration. Therefore, we performed regeneration at 130°C in this experiment. Table 35 shows measured LIV data of full Al-BSF and PERC cells after LID, 130°C/1.5 hours/2 suns regeneration, followed by another LID treatments.

Table 35: Measured Average LIV Data of Full Al-BSF and PERC Cells After LID, 130°C/2 Suns/1.5 Hours Regeneration and LID Cycles

Average of ()	Step	Voc (mV)	Jsc (mA/cm2)	FF (%)	Efficiency (%)
PERC (2)	Initial	663	38.7	78.7	20.2±0.05
	LID	655	38.4	77.5	19.5±0.05
	Regeneration	663	38.8	78.6	20.2±0.06
	LID	664	38.7	78.8	20.2±0.02
Full Al-BSF (2)	Initial	638	37.6	79.8	19.1±0.02
	LID	630	37.2	79.2	18.6±0.03
	Regeneration	639	37.6	79.8	19.1±0.02
	LID	638	37.6	79.7	19.1±0.02

Table 35 shows that pre-LID efficiencies were 20.2% and 19.1% for the PERC and full Al-BSF cells. After 48-hour LID test at 37°C under 0.8 sun, efficiencies decreased to 19.5% and 18.6% for the PERC and full Al-BSF cells. After a subsequent 1.5-hour regeneration at 130°C under 2 suns, both PERC and full Al-BSF cells were fully regenerated to the original efficiency of 20.2% and 19.1% and were fully stabilized with no change in performance with subsequent LID (Table 36).

Table 36: Measured LIV Data of Full Al-BSF and PERC Cells After 2 Suns/130°C/1.5 Hours Regeneration Followed by LID

	Step	Voc (mV)	Jsc (mA/cm2)	FF (%)	Efficiency (%)
PERC	Initial	664	38.6	79.0	20.3
	Regeneration	664	38.6	79.4	20.3
	LID	664	38.7	79.2	20.3
Full Al-BSF	Initial	640	37.9	79.5	19.3
	Regeneration	640	37.5	79.9	19.2
	LID	638	37.7	79.8	19.2

Figures 113 and 114 show effective lifetimes as a function of injection level and IQE measurements of the cells in Table 35. These measurements give a picture of total recombination in the cell. As expected after first LID, we saw a significant decrease in effective lifetimes and long wavelength IQE responses (800-120nm). However, after subsequent regeneration and LID, response was identical to the initial or pre-LID condition, supporting full stabilization.

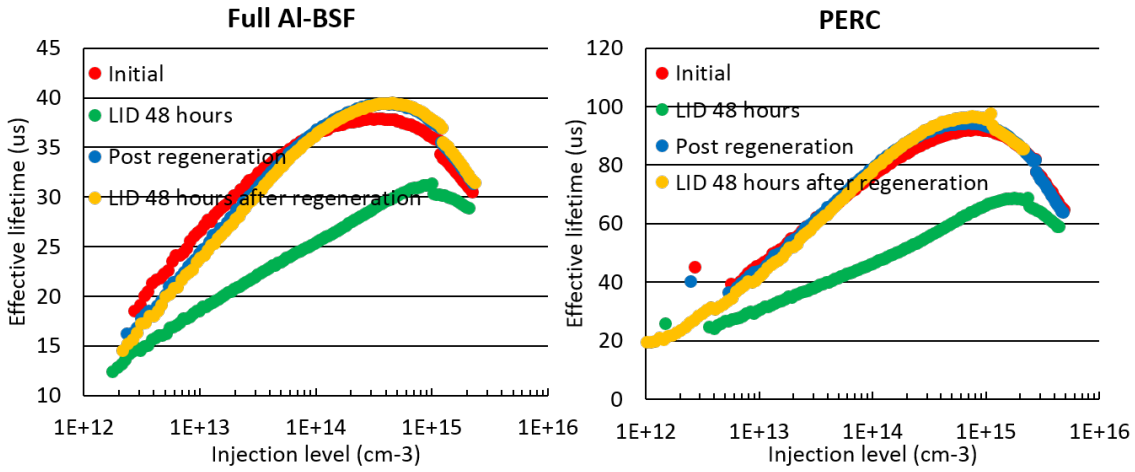

Figure 113: Measured effective lifetimes as a function of injection level on Full Al-BSF and PERC cells after LID, 130°C/2 suns/1.5 hours regeneration and subsequent LID.

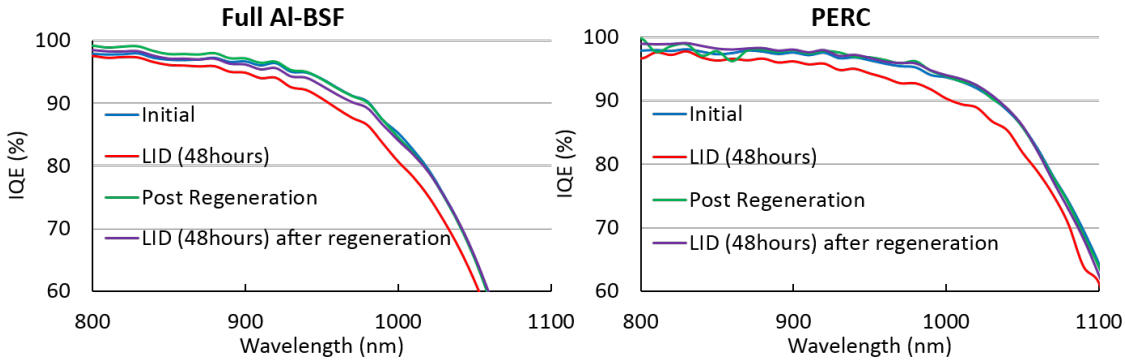

Figure 114: Measured internal quantum efficiency (IQE) on full Al-BSF and PERC cells for each step: initial, post 48 hours LID, post regeneration and post 48 hours LID.

10.3 Conclusion

In this chapter, we investigated the impact of LID on widely used full Al-BSF and PERC. LID test was performed at 37°C under 0.8 sun for 48 hours which showed sufficient time to form all the B-O complexes. In addition, three regeneration treatments were investigated (200°C/3 suns/30s, 75°C/1 sun/48 hours and 130°C/2 suns/1.5 hours) before and after the LID test in an attempt to eliminate LID either by preventing the formation of active B-O complexes or by passivating them by hydrogen during the regeneration cycle. Pre-LID efficiencies of PERC and full Al-BSF cells were ∼20.4% and 19.2%, respectively. After LID, efficiency of PERC and baseline full Al-BSF cells dropped to 19.5% and 18.5%, respectively. PERC cells showed a much greater loss in absolute cell efficiency (0.9% vs 0.6%) because the degradation in bulk lifetime also erodes the benefit of superior BSRV in PERC cells. The 200°C/3 suns/30s regeneration treatment prior to LID reduced the efficiency degradation from 0.9% to 0.1% in PERC cells and from 0.6% to 0.3% in baseline full Al-BSF cells, respectively. This is because PERC cell has more hydrogen in the bulk Si due to double side SiNx and higher injection level or quasi-fermi level split due to higher Voc. This helps in the creation more neutral hydrogen (H+ -> H0) which migrates to the B-O complexes. Hydrogen in silicon is tied to impurities like boron initially and dissociates as H+ at elevated temperature. It then changes its state from H+ to H0 due to quasi-fermi level split from light induced injection and migrate toward B-O complexes to deactivate them. Regeneration at 75°C/1 sun for 48 hours, prior to LID, reduced the efficiency loss to 0.1-0.2% and 0.3% in PERC and baseline full Al-BSF cells. Notice that both high and low temperature regeneration conditions were unable to reach 100% stabilization. This is probably because at high temperature (200°C) some of the passivated B-O complexes revert back to annealed or destabilized states during regeneration. For the low temperature (75°C) case, the regeneration or defect passivation is so slow that even after 48 hours of regeneration some B-O complexes are

active. Therefore, regeneration was attempted the regeneration at an intermediate temperature of 130°C at 2 suns for 1.5 hours. This condition achieved full passivation or stabilization because regeneration is fast enough to passivate all the B-O complexes without triggering the destabilization or annealed paths. Thus, optimized regeneration process can lead to full stabilization in PERC as well as baseline cells.

CHAPTER XI

FUTURE WORK

This thesis developed various commercially applicable technologies to further increase and stabilize p-type PERC cell efficiency using industrial grade large area (239 cm^2) p-type Cz silicon wafers. The topic covered in this research includes 1) comparison of phosphorus ion-implantation and $POCl_3$ diffusion, 2) optimization of front grid design with five busbars and 89 gridlines with fine grid line screen-printing, 3) field effect passivation by negative charge injection into silicon nitride using a novel plasma charging tool, 4) selective emitter by etch-back process, 5) development of a roadmap to 23% PERC cell by 2D Sentaurus modeling with practical and manufacturable technology developments, 6) fabrication and analysis of light-induced degradation (LID) free indium-doped PERC cells, and 7) understanding and development of regeneration treatment to eliminate LID in boron doped cells.

The p-type PERC cells fabricated with these technologies achieved 20.6% efficiency. However, this efficiency is on the lower-end of the current PERC cell industry. Higher efficiency is critical to further reduce PV module cost because the cost of PV installation is still more expensive than that of fossil fuels in most parts of the world. Therefore, this chapter suggests research directions to further improve cell efficiency and attain $\geq$23% efficienct p-type solar cells which involve enhancing cleaning process such as incorporating piranha solution cleaning step to increase bulk lifetime for etched-back selective emitter process and five additional feasible technologies as shown in Figure 115: 1) narrower finger and busbar screen printing, 2) formation of thicker local Al-BSF, 3) higher bulk lifetime (2ms), 4) self-aligned emitter by laser

doping and plating and 5) 15 wire busbar technologies. These five additional technologies were discussed in more detail in Chapter 8. These innovations can achieve the PERC cell efficiency to 23%.

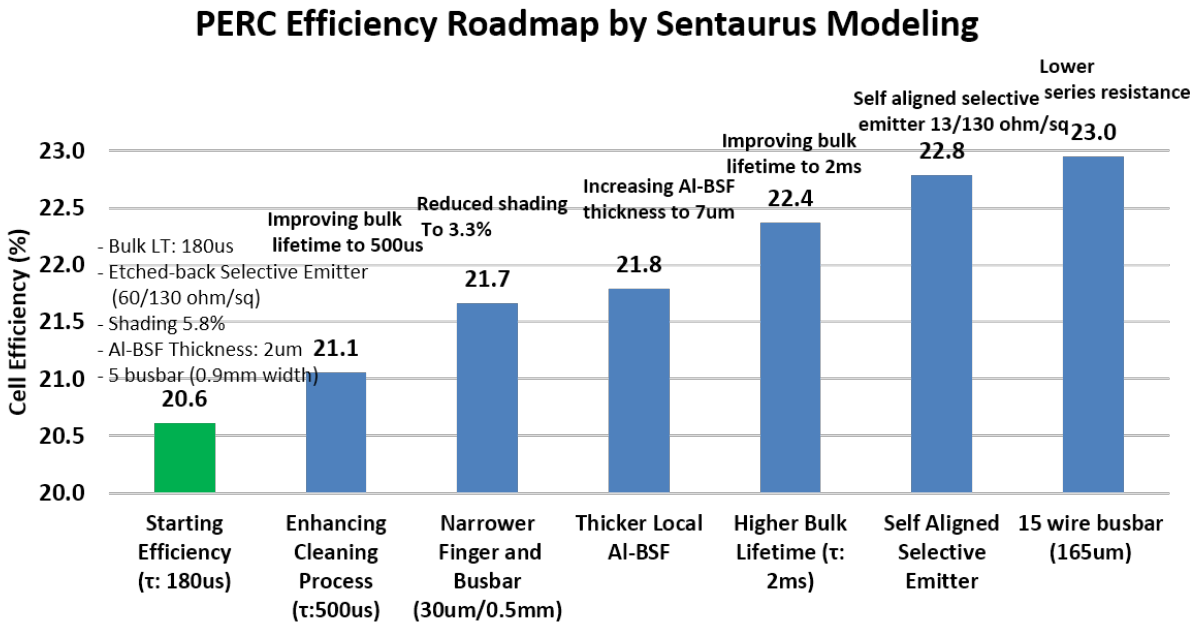

Figure 115: Technology roadmap to achieve 23% PERC cell efficiency by Sentaurus 2D modeling.

Further studies should also be conducted on LID degradation and development of low-cost high throughput commercial tool to eliminate LID completely in B-doped PERC cells. Additional studies should be conducted to ensure that regeneration process is stable over 30 years of module life. Since we had great success in injecting significant amount of charge using novel low-cost commercially viable plasma tool, it opens new areas of research where one can apply this not just for passivation but forming junctions. Charge injection in dielectrics on silicon wafers can be used to create electron- or hole-rich inversion or accumulation layers to eliminate conventional diffusion and dopants to form p-n junctions and back surface field, provided one can achieve enough carriers to get low sheet resistance.

APPENDIX A

PUBLICATIONS FROM THIS WORK

Journal Papers:

[1] **Eunhwan Cho**, Young-Woo Ok, Lila D Dahal, Arnab Das, Vijaykumar Upadhyaya, Ajeet Rohatgi, "Comparison of $POCl_3$ Diffusion and Phosphorus Ion-implantation Induced Gettering in Crystalline Si Solar Cells." *Solar Energy Materials and Solar Cells 157*, 2016, 245-249.

[2] **Eunhwan Cho**, Young-Woo Ok, Ajay D Upadhyaya, Martin Jeff Binns, Jesse Appel, Jason Guo, Ajeet Rohatgi, "P-Type Indium-Doped Passivated Emitter Rear Solar Cells (PERC) on Czochralski Silicon Without Light-Induced Degradation." *IEEE Journal of Photovoltaics, vol. 6*, 2016, pp. 795-800.

[3] Kyungsun Ryu, **Eunhwan Cho**, Ajeet Rohatgi, YoungWoo Ok, "Process development and comparison of various boron emitter technologies for higheffi-ciency (∼21%) ntype silicon solar cells." *Progress in Photovoltaics: Research and Applications*, 2016.

[4] Yuguo Tao, Keeya Madini, **Eunhwan Cho**, Brian Rounsaville, Vijaykimar Upadhyaya, Ajeet Rohatgi, "High-efficiency selective boron emitter formed by wet chemical etch-back for n-type screen-printed Si solar cells." *Applied Physics Letters (Vol.110, Issue 2)*, 2017.

[5] Woojun Yoon, James E Moore, **Eunhwan Cho**, David Scheiman, Nicole A Kotulak, Erin Cleveland, Young-Woo Ok, Phillip P. Jenkins, Ajeet Rohatgi and Robert J. Walters, "Hole-selective Molybdenum Oxide as a Full-area Rear Contact to Crystalline p-type Si Solar Cells." *Japanese Journal of Applied Physics (special issue, 2017)*, 2017.

Conference Papers:

[1] **Eunhwan Cho**, Youngwoo Ok, Kyungsun Ryu, Brian Rounsaville, Ajay D Upadhyaya, Vijaykumar Upadhyaya, Ajeet Rohatgi, "Comparison of $POCl_3$ Diffusion with Phosphorus Ion Implantation for Czochralski and Quasi-mono Silicon Solar Cells." *2014 IEEE 40th Photovoltaic Specialist Conference (PVSC)*, 2014.

[2] **Eunhwan Cho**, J-H Lai, Young-woo Ok, Ajay D Upadhyaya, A Rohatgi, MJ Binns, J Appel, J Guo, H Fang, EA Good, "Light-induced Degradation Free and High Efficiency P-type Indium-doped PERC Solar Cells on Czochralski Silicon." *2015 IEEE 42nd Photovoltaic Specialist Conference (PVSC)*, 2015.

[3] Woojun Yoon, **Eunhwan Cho**, Jason D Myers, Young-Woo Ok, Matthew P Lumb, Jesse A Frantz, Nicole A Kotulak, David Scheiman, Phillip P Jenkins, Ajeet Rohatgi, Robert J Walters, "Transparent conducting oxide-based, passivated contacts for high efficiency crystalline Si solar cells." *2015 IEEE 42nd Photovoltaic Specialist Conference (PVSC)*, 2015.

[4] Ajay D. Upadhyaya, Young Woo Ok, Elizabeth Chang, Vijaykumar Upadhyaya, Keeya Madani, Keith Tate, **Eunhwan Cho**, Brain Rounsaville, V. Chandrasekaran, V. Yelundur, Atul Gupta, Ajeet Rohatgi, "Ion implanted screen printed N-type solar cell with tunnel oxide passivated back contact." *2015 IEEE 42nd Photovoltaic Specialist Conference (PVSC)*, 2015.

[5] **Eunhwan Cho**, Young-Woo Ok, James Hwang, Ajay D. Upadhyaya, John Keith Tate, Francesco Zimbardi, A. Rohatgi, "Field-Effect Passivation by Charge Injection into SiNx Using a Novel Low-cost Plasma Charging Method." *2016 IEEE 43rd Photovoltaic Specialist Conference (PVSC)*, 2016.

[6] **Eunhwan Cho**, Young-Woo Ok, James Hwang, Aditi Jain, Vijay D. Upadhyaya, John Keith Tate, and Ajeet Rohatgi, "Field-Effect Passivation by Charge Injection into SiNx Using a Novel Low-cost Plasma Charging Method." *2017 IEEE 44th Photovoltaic Specialist Conference (PVSC)*, 2017.

REFERENCES

[1] R. Vos and M. F. e. a. Montes, "World economic and social survey 2011. the great green technological transformation.," *Department of Economic and Social Affairs of the United Nations Secretariat (UN/DESA), United Nations publication.*, 2011.

[2] B. PLC, "Bp statistical review of world energy 2015, data workbook," tech. rep., 2015.

[3] A. internationale de l'énergie, *Energy technology perspectives 2012: pathways to a clean energy system*. OECD/IEA, 2012.

[4] Con-struct, "World energy consumption," tech. rep., BP Statistical Review of World Energy, 2015.

[5] T. Boden, G. Marland, and R. Andres, "Global, regional, and national fossil fuel co2 emissions," *Trends: A Compendium of Data on Global Change*, 2015.

[6] R. Harrington, "This incredible fact should get you psyched about solar power," tech. rep., Tech Insider, 2015.

[7] W. T. F. Encyclopedia., "Growth of photovoltaics," *Wikimedia Foundation Inc. Web.*, 8th June 2016.

[8] H. Forstner *et al.*, "International technology roadmap for photovoltaic (itrpv) 2015 results," *SEMI Europe, Berlin, Germany*, p. 32, 2016.

[9] R. Jones-Albertus, D. Feldman, R. Fu, K. Horowitz, and M. Woodhouse, "Technology advances needed for photovoltaics to achieve widespread grid price parity," *Progress in Photovoltaics: Research and Applications*, 2016.

[10] L. Cost, "Levelized avoided cost of new generation resources in the annual energy outlook 2015 (us energy information administration, 2015)," 2015.

[11] T. S. Initiative, "The sunshot initiatives 2030 goal: 3 per kilowatt hour for solar electricity," tech. rep., U.S. Department of Energy, Office of Energy Efficiency & Renewable Energy, December, 2016.

[12] A. Das and A. Rohatgi, "The impact of cell design on light induced degradation in p-type silicon solar cells," in *Photovoltaic Specialists Conference (PVSC), 2011 37th IEEE*, pp. 000158–000164, IEEE, 2011.

[13] F. Colville, "Solar cell technology roadmap for 2016," *PV-tech & Solar Media LTd*, February 2016.

[14] S. K. Chunduri and M. Schmela, "Perc solar cell technology 2016 background, status and outlook," 2016.

[15] E. Cho, Y.-W. Ok, A. D. Upadhyaya, M. J. Binns, J. Appel, J. Guo, and A. Rohatgi, "P-type indium-doped passivated emitter rear solar cells (perc) on czochralski silicon without light-induced degradation," *IEEE Journal of Photovoltaics*, 2016.

[16] A. S. for Testing and N. R. E. L. Materials, "Reference solar spectral irradiance: Air mass 1.5," *Online, http://rredc.nrel.gov/solar/spectra/am1.5/*.

[17] T. at English Wikipedia, "A p-n junction in thermal equilibrium with zero bias voltage applied.," August 2007. [GFDL (http://www.gnu.org/copyleft/fdl.html) , CC-BY-SA-3.0 (http://creativecommons.org/licenses/by-sa/3.0/) or CC BY-SA 2.5-2.0-1.0 (http://creativecommons.org/licenses/by-sa/2.5-2.0-1.0)] , via Wikimedia Commons.

[18] P. Würfel and U. Würfel, *Physics of solar cells: from basic principles to advanced concepts*. John Wiley & Sons, 2009. pp.82-85.

[19] R. M. Swanson, "Approaching the 29% limit efficiency of silicon solar cells," in *Conference Record of the Thirty-first IEEE Photovoltaic Specialists Conference, 2005.*, pp. 889–894, IEEE, 2005.

[20] H. Panasonic, "solar cell achieves worlds highest energy conversion efficiency of 25.6% at research level," *Press release*, 2014.

[21] D. D. Smith, P. Cousins, S. Westerberg, R. De Jesus-Tabajonda, G. Aniero, and Y.-C. Shen, "Toward the practical limits of silicon solar cells," *IEEE Journal of Photovoltaics*, vol. 6, no. 4, pp. 1465–1469, 2014.

[22] M. A. Green and M. J. Keevers, "Optical properties of intrinsic silicon at 300 k," *Progress in Photovoltaics: Research and Applications*, vol. 3, no. 3, pp. 189–192, 1995.

[23] M. A. Green, *Operating Principles, Technology, and System Applications*. Prentice-Hall series in solid state physical electronics) by Martin A. Green, 1982.

[24] E. Wang, F. Yu, V. Simms, H. Brandhorst Jr, and J. Broder, "Optimum design of antireflection coating for silicon solar cells," 1974.

[25] B. Dale and H. Rudenberg, "Photovoltaic conversion-high efficiency silicon solar cells," 1960.

[26] M. A. Green, "Self-consistent optical parameters of intrinsic silicon at 300k including temperature coefficients," *Solar Energy Materials and Solar Cells*, vol. 92, no. 11, pp. 1305–1310, 2008.

[27] M. Keevers and M. Green, "Extended infrared response of silicon solar cells and the impurity photovoltaic effect," in *Photovoltaic Energy Conversion, 1994., Conference Record of the Twenty Fourth. IEEE Photovoltaic Specialists Conference-1994, 1994 IEEE First World Conference on*, vol. 2, pp. 1433–1436, IEEE, 1994.

[28] D. Kane and R. Swanson, "Measurement of the emitter saturation current by a contactless photoconductivity decay method," in *IEEE photovoltaic specialists conference. 18*, pp. 578–583, 1985.

[29] A. Cuevas and D. Macdonald, "Measuring and interpreting the lifetime of silicon wafers," *Solar Energy*, vol. 76, no. 1, pp. 255–262, 2004.

[30] R. A. Sinton and A. Cuevas, "Contactless determination of current–voltage characteristics and minority-carrier lifetimes in semiconductors from quasi-steady-state photoconductance data," *Applied Physics Letters*, vol. 69, no. 17, pp. 2510–2512, 1996.

[31] T. Fellmeth, A. Born, A. Kimmerle, F. Clement, D. Biro, and R. Preu, "Recombination at metal-emitter interfaces of front contact technologies for highly efficient silicon solar cells," *Energy Procedia*, vol. 8, pp. 115–121, 2011.

[32] D. Meier, E. Good, R. Garcia, B. Bingham, S. Yamanaka, V. Chandrasekaran, and C. Bucher, "Determining components of series resistance from measurements on a finished cell," in *2006 IEEE 4th World Conference on Photovoltaic Energy Conference*, vol. 2, pp. 1315–1318, IEEE, 2006.

[33] C. S. Solanki, *Solar photovoltaics: fundamentals, technologies and applications*. PHI Learning Pvt. Ltd., 2015.

[34] M. A. Green, "The path to 25% silicon solar cell efficiency history of silicon cell evolution," *Progress in Photovoltaics Research and Applications*, vol. 17, no. 3, pp. 183–189, 2009.

[35] R. S. Ohl, "Light-sensitive electric device including silicon," June 15 1941. US Patent 2,443,542.

[36] W. Palz, *Power for the World: The Emergence of Electricity from the Sun*. Pan Stanford Publishing, 2010.

[37] J. Perlin, *From Space to Earth: The Story of Solar Electricity*. No. ISBN 978-0-937948-14-9, Earthscan, 1999.

[38] W. T. F. Encyclopedia., "Solar cell," *Wikimedia Foundation Inc. Web.*, 10th June 2016.

[39] J. Richardson and R. Nordhaus, "The national energy act of 1978," *Natural Resources & Environment*, vol. 10, no. 1, pp. 62–88, 1995.

[40] A. W. Blakers, A. Wang, A. M. Milne, J. Zhao, and M. A. Green, "22.8% efficient silicon solar cell," *Applied Physics Letters*, vol. 55, no. 13, pp. 1363–1365, 1989.

[41] K. Masuko, M. Shigematsu, T. Hashiguchi, D. Fujishima, M. Kai, N. Yoshimura, T. Yamaguchi, Y. Ichihashi, T. Mishima, N. Matsubara, *et al.*, "Achievement of more than 25% conversion efficiency with crystalline silicon heterojunction solar cell," *IEEE Journal of Photovoltaics*, vol. 4, no. 6, pp. 1433–1435, 2014.

[42] M. A. Green, K. Emery, Y. Hishikawa, W. Warta, and E. D. Dunlop, "Solar cell efficiency tables (version 45)," *Progress in photovoltaics: research and applications*, vol. 23, no. 1, pp. 1–9, 2015.

[43] I. Clover, "Trina solar sets new 22.61

[44] D. Erath, "Printing techniques in the c-si pv industry-a brief technological overview," *International Circular of Graphic Education and Research*, vol. 3, pp. 8–15, 2010.

[45] P. Mariani, L. Vesce, and A. Di Carlo, "The role of printing techniques for large-area dye sensitized solar cells," *Semiconductor Science and Technology*, vol. 30, no. 10, p. 104003, 2015.

[46] W. T. F. Encyclopedia., "Electrical resistivity and conductivity," *Wikimedia Foundation Inc. Web.*, 11th June 2016.

[47] J. Schmidt and K. Bothe, "Structure and transformation of the metastable boron-and oxygen-related defect center in crystalline silicon," *Physical review B*, vol. 69, no. 2, p. 024107, 2004.

[48] J. Schmidt, A. G. Aberle, and R. Hezel, "Investigation of carrier lifetime instabilities in cz-grown silicon," in *Photovoltaic Specialists Conference, 1997., Conference Record of the Twenty-Sixth IEEE*, pp. 13–18, IEEE, 1997.

[49] S. W. Glunz, S. Rein, W. Warta, J. Knobloch, and W. Wettling, "Degradation of carrier lifetime in cz silicon solar cells," *Solar energy materials and solar cells*, vol. 65, no. 1, pp. 219–229, 2001.

[50] K. Bothe, R. Hezel, and J. Schmidt, "Recombination-enhanced formation of the metastable boron–oxygen complex in crystalline silicon," *Applied physics letters*, vol. 83, no. 6, pp. 1125–1127, 2003.

[51] K. Bothe, R. Sinton, and J. Schmidt, "Fundamental boron–oxygen-related carrier lifetime limit in mono-and multicrystalline silicon," *Progress in Photovoltaics: Research and Applications*, vol. 13, no. 4, pp. 287–296, 2005.

[52] T. Hicks, A. Organ, and N. Riley, "Oxygen transport in magnetic czochralski growth of silicon with a non-uniform magnetic field," *Journal of crystal growth*, vol. 94, no. 1, pp. 213–228, 1989.

[53] S. Wilking, A. Herguth, and G. Hahn, "Influence of hydrogen on the regeneration of boron-oxygen related defects in crystalline silicon," *Journal of Applied Physics*, vol. 113, no. 19, p. 194503, 2013.

[54] V. Meemongkolkiat, K. Nakayashiki, A. Rohatgi, G. Crabtree, J. Nickerson, and T. L. Jester, "The effect of the variation in resistivity and lifetime on the solar cells performance along the commercially grown ga-and b-doped czochralski ingots," in *Photovoltaic Specialists Conference, 2005. Conference Record of the Thirty-first IEEE*, pp. 1115–1118, IEEE, 2005.

[55] E. Cho, J.-H. Lai, Y.-w. Ok, A. D. Upadhyaya, A. Rohatgi, M. Binns, J. Appel, J. Guo, H. Fang, and E. Good, "Light-induced degradation free and high efficiency p-type indium-doped perc solar cells on czochralski silicon," in *Photovoltaic Specialist Conference (PVSC), 2015 IEEE 42nd*, pp. 1–4, IEEE, 2015.

[56] D. Macdonald, L. Geerligs, and A. Azzizi, "Iron detection in crystalline silicon by carrier lifetime measurements for arbitrary injection and doping," *Journal of Applied Physics*, vol. 95, no. 3, pp. 1021–1028, 2004.

[57] J. Cotter, J. Guo, P. Cousins, M. Abbott, F. Chen, and K. Fisher, "P-type versus n-type silicon wafers: prospects for high-efficiency commercial silicon solar cells," *IEEE Transactions on Electron Devices*, vol. 53, no. 8, pp. 1893–1901, 2006.

[58] D. Macdonald, L. Geerligs, *et al.*, "Recombination activity of interstitial iron and other transition metal point defects in p-and n-type crystalline silicon," 2004.

[59] J. Hofstetter, J. F. Lelièvre, D. P. Fenning, M. I. Bertoni, T. Buonassisi, and C. Del Cañizo, "Towards the tailoring of p diffusion gettering to as-grown silicon material properties," in *Solid State Phenomena*, vol. 178, pp. 158–165, Trans Tech Publ, 2011.

[60] S. Rein and S. Glunz, "Electronic properties of interstitial iron and iron-boron pairs determined by means of advanced lifetime spectroscopy," *Journal of Applied Physics*, vol. 98, no. 11, pp. 113711–113711, 2005.

[61] T. Buonassisi, A. Istratov, M. Pickett, M. Heuer, J. Kalejs, G. Hahn, M. Marcus, B. Lai, Z. Cai, S. Heald, *et al.*, "Chemical natures and distributions of metal impurities in multicrystalline silicon materials," *Progress in Photovoltaics: Research and Applications*, vol. 14, no. 6, pp. 513–531, 2006.

[62] M. Seibt, A. Sattler, C. Rudolf, O. Voß, V. Kveder, and W. Schröter, "Gettering in silicon photovoltaics: current state and future perspectives," *physica status solidi (a)*, vol. 203, no. 4, pp. 696–713, 2006.

[63] S. Myers, M. Seibt, and W. Schröter, "Mechanisms of transition-metal gettering in silicon," *Journal of Applied Physics*, vol. 88, no. 7, pp. 3795–3819, 2000.

[64] J. Kang and D. Schroder, "Gettering in silicon," *Journal of Applied Physics*, vol. 65, no. 8, pp. 2974–2985, 1989.

[65] N. Khedher, M. Hajji, M. Hassen, A. B. Jaballah, B. Ouertani, H. Ezzaouia, B. Bessais, A. Selmi, and R. Bennaceur, "Gettering impurities from crystalline silicon by phosphorus diffusion using a porous silicon layer," *Solar energy materials and solar cells*, vol. 87, no. 1, pp. 605–611, 2005.

[66] M. B. Shabani, T. Yamashita, and E. Morita, "Study of gettering mechanisms in silicon: competitive gettering between phosphorus diffusion gettering and other gettering sites," in *Solid state phenomena*, vol. 131, pp. 399–404, Trans Tech Publ, 2008.

[67] A. Istratov, H. Hieslmair, and E. Weber, "Iron contamination in silicon technology," *Applied Physics A*, vol. 70, no. 5, pp. 489–534, 2000.

[68] G. Zoth and W. Bergholz, "A fast, preparation-free method to detect iron in silicon," *Journal of Applied Physics*, vol. 67, no. 11, pp. 6764–6771, 1990.

[69] J. Lagowski, P. Edelman, A. Kontkiewicz, O. Milic, W. Henley, M. Dexter, L. Jastrzebski, and A. Hoff, "Iron detection in the part per quadrillion range in silicon using surface photovoltage and photodissociation of iron-boron pairs," *Applied physics letters*, vol. 63, no. 22, pp. 3043–3045, 1993.

[70] G. Rozgonyi, P. Petroff, and M. Read, "Elimination of oxidation-induced stacking faults by preoxidation gettering of silicon wafers i. phosphorus diffusion-induced misfit dislocations," *Journal of The Electrochemical Society*, vol. 122, no. 12, pp. 1725–1729, 1975.

[71] D. Lecrosnier, J. Paugam, G. Pelous, F. Richou, and M. Salvi, "Gold gettering in silicon by phosphorous diffusion and argon implantation: mechanisms and limitations," *Journal of Applied Physics*, vol. 52, no. 8, pp. 5090–5097, 1981.

[72] D. Lecrosnier, J. Paugam, F. Richou, G. Pelous, and F. Beniere, "Influence of phosphorus-induced point defects on a gold-gettering mechanism in silicon," *Journal of Applied Physics*, vol. 51, no. 2, pp. 1036–1038, 1980.

[73] J. Hofstetter, C. Cañizo, H. Wagner, S. Castellanos, and T. Buonassisi, "Material requirements for the adoption of unconventional silicon crystal and wafer growth techniques for high-efficiency solar cells," *Progress in Photovoltaics: Research and Applications*, vol. 24, no. 1, pp. 122–132, 2016.

[74] A. G. Aberle, "Overview on sin surface passivation of crystalline silicon solar cells," *Solar energy materials and solar cells*, vol. 65, no. 1, pp. 239–248, 2001.

[75] J. Schmidt and M. Kerr, "Highest-quality surface passivation of low-resistivity p-type silicon using stoichiometric pecvd silicon nitride," *Solar Energy Materials and Solar Cells*, vol. 65, no. 1, pp. 585–591, 2001.

[76] S. Dauwe, L. Mittelstädt, A. Metz, and R. Hezel, "Experimental evidence of parasitic shunting in silicon nitride rear surface passivated solar cells," *Progress in Photovoltaics: Research and Applications*, vol. 10, no. 4, pp. 271–278, 2002.

[77] B. Hoex, J. Schmidt, P. Pohl, M. Van de Sanden, and W. Kessels, "Silicon surface passivation by atomic layer deposited al 2 o 3," *Journal of Applied Physics*, vol. 104, no. 4, p. 044903, 2008.

[78] J.-S. Chang, P. A. Lawless, and T. Yamamoto, "Corona discharge processes," *IEEE Transactions on plasma science*, vol. 19, no. 6, pp. 1152–1166, 1991.

[79] S. Glunz, D. Biro, S. Rein, and W. Warta, "Field-effect passivation of the sio 2 si interface," *Journal of Applied Physics*, vol. 86, no. 1, pp. 683–691, 1999.

[80] W. Shockley and W. Read Jr, "Statistics of the recombinations of holes and electrons," *Physical review*, vol. 87, no. 5, p. 835, 1952.

[81] R. B. Girisch, R. P. Mertens, and R. De Keersmaecker, "Determination of si-sio/sub 2/interface recombination parameters using a gate-controlled point-junction diode under illumination," *IEEE Transactions on Electron Devices*, vol. 35, no. 2, pp. 203–222, 1988.

[82] A. Lorenz, J. John, B. Vermang, E. Cornagliotti, and J. Poortmans, "Comparison of illumination level dependency and rear internal reflectance of perc-type cells with different dielectric passivation stacks," in *Proc. 26th Eur. Photovoltaic Sol. Energy Conf*, pp. 1486–1488, 2011.

[83] H. Hieslmair and J. Appel, "Effects of injection-level dependent bulk lifetime on cell properties," in *Photovoltaic Specialists Conference (PVSC), 2016 IEEE 43rd*, pp. 2434–2439, IEEE, 2016.

[84] T. Röder, P. Grabitz, S. Eisele, C. Wagner, J. Köhler, and J. Werner, "0.4% absolute efficiency gain of industrial solar cells by laser doped selective emitter," in *Photovoltaic Specialists Conference (PVSC), 2009 34th IEEE*, pp. 000871–000873, IEEE, 2009.

[85] C. E. Dubé, B. Tsefrekas, D. Buzby, R. Tavares, W. Zhang, A. Gupta, R. J. Low, W. Skinner, and J. Mullin, "High efficiency selective emitter cells using patterned ion implantation," *Energy Procedia*, vol. 8, pp. 706–711, 2011.

[86] Z. Liang, F. Zeng, H. Song, and H. Shen, "Effect of porous si and an etch-back process on the performance of a selective emitter solar cell," *Solar Energy Materials and Solar Cells*, vol. 109, pp. 26–32, 2013.

[87] D. Turner, "On the mechanism of chemically etching germanium and silicon," *Journal of the electrochemical Society*, vol. 107, no. 10, pp. 810–816, 1960.

[88] Y. Tao, K. Madani, E. Cho, B. Rounsaville, V. Upadhyaya, and A. Rohatgi, "High-efficiency selective boron emitter formed by wet chemical etch-back for n-type screen-printed si solar cells," *Applied Physics Letters*, vol. 110, no. 2, p. 021101, 2017.

[89] K. W. Kolasinski, "Silicon nanostructures from electroless electrochemical etching," *Current Opinion in Solid State and Materials Science*, vol. 9, no. 1, pp. 73–83, 2005.

[90] R. King, R. Sinton, and R. Swanson, "Studies of diffused phosphorus emitters: saturation current, surface recombination velocity, and quantum efficiency," *IEEE Transactions on electron devices*, vol. 37, no. 2, pp. 365–371, 1990.

[91] R. Sinton, A. Cuevas, *et al.*, "A quasi-steady-state open-circuit voltage method for solar cell characterization," in *Proceedings of the 16th European Photovoltaic Solar Energy Conference*, vol. 1152, 2000.

[92] S. D. U. Guide and G. Version, "Synopsis," *Mountain View, CA*, 2012.

[93] P. P. Altermatt, "Models for numerical device simulations of crystalline silicon solar cellsa review," *Journal of computational electronics*, vol. 10, no. 3, p. 314, 2011.

[94] J. Walter, M. Tranitz, M. Volk, C. Ebert, and U. Eitner, "Multi-wire interconnection of busbar-free solar cells," *Energy Procedia*, vol. 55, pp. 380–388, 2014.

[95] A. Herguth and G. Hahn, "Kinetics of the boron-oxygen related defect in theory and experiment," *Journal of Applied Physics*, vol. 108, no. 11, p. 114509, 2010.

[96] D. Walter, B. Lim, K. Bothe, R. Falster, V. Voronkov, and J. Schmidt, "Lifetimes exceeding 1ms in 1-ωcm boron-doped cz-silicon," *Solar Energy Materials and Solar Cells*, vol. 131, pp. 51–57, 2014.

[97] S. Glunz, B. Köster, T. Leimenstoll, S. Rein, E. Schäffer, J. Knobloch, and T. Abe, "100 cm2 solar cells on czochralski silicon with an efficiency of 20· 2%," *Progress in Photovoltaics: Research and Applications*, vol. 8, no. 2, pp. 237–240, 2000.

[98] J. Schmidt and D. Macdonald, "Recombination activity of iron-gallium and iron-indium pairs in silicon," *Journal of applied physics*, vol. 97, no. 11, p. 113712, 2005.

[99] S. Glunz, S. Rein, J. Knobloch, W. Wettling, and T. Abe, "Comparison of boron- and gallium-doped p-type czochralski silicon for photovoltaic application," *Progress in Photovoltaics Research and Applications*, vol. 7, no. 6, pp. 463–469, 1999.

[100] M. Binns, J. Appel, J. Guo, H. Hieslmair, J. Chen, T. Swaminathan, and E. Good, "Indium-doped mono-crystalline silicon substrates exhibiting negligible lifetime degradation following light soaking," in *Photovoltaic Specialist Conference (PVSC), 2015 IEEE 42nd*, pp. 1–6, IEEE, 2015.

[101] C. Möller and K. Lauer, "Light-induced degradation in indium-doped silicon," *physica status solidi (RRL)-Rapid Research Letters*, vol. 7, no. 7, pp. 461–464, 2013.

[102] S. Z. Karazhanov, "Impurity photovoltaic effect in indium-doped silicon solar cells," *Journal of Applied Physics*, vol. 89, no. 7, pp. 4030–4036, 2001.

[103] M. Keevers and M. Green, "Efficiency improvements of silicon solar cells by the impurity photovoltaic effect," *Journal of Applied Physics*, vol. 75, no. 8, pp. 4022–4031, 1994.

[104] H. Mäckel and K. Varner, "On the determination of the emitter saturation current density from lifetime measurements of silicon devices," *Progress in Photovoltaics: Research and Applications*, vol. 21, no. 5, pp. 850–866, 2013.

[105] T. Horanyi, T. Pavelka, and P. Tüttö, "In situ bulk lifetime measurements on silicon with a chemically passivated surface," *Appl. Surf. Sci*, vol. 63, pp. 306–311, 2012.

[106] D. Kray and S. Glunz, "Investigation of laser-fired rear-side recombination properties using an analytical model," *Progress in Photovoltaics: Research and Applications*, vol. 14, no. 3, pp. 195–201, 2006.

[107] A. Herguth, G. Schubert, M. Käs, and G. Hahn, "Investigations on the long time behavior of the metastable boron–oxygen complex in crystalline silicon," *Progress in Photovoltaics: Research and Applications*, vol. 16, no. 2, pp. 135–140, 2008.

[108] J.-R. Huang, Y.-F. Lin, K. Liang, S. Su, S. H. Chen, and L.-W. Cheng, "Investigation of light-induced regeneration phenomena on p-type cz perc cells," in *Photovoltaic Specialist Conference (PVSC), 2015 IEEE 42nd*, pp. 1–3, IEEE, 2015.

[109] S. Wilking, C. Beckh, S. Ebert, A. Herguth, and G. Hahn, "Influence of bound hydrogen states on bo-regeneration kinetics and consequences for high-speed regeneration processes," *Solar Energy Materials and Solar Cells*, vol. 131, pp. 2–8, 2014.

[110] S. Wilking, M. Forster, A. Herguth, and G. Hahn, "From simulation to experiment: Understanding bo-regeneration kinetics," *Solar Energy Materials and Solar Cells*, vol. 142, pp. 87–91, 2015.

[111] A. Herguth, R. Horbelt, S. Wilking, R. Job, and G. Hahn, "Comparison of bo regeneration dynamics in perc and al-bsf solar cells," *Energy Procedia*, vol. 77, pp. 75–82, 2015.

[112] M. Cascant, N. Enjalbert, R. Monna, and S. Dubois, "Influence of various p-type czochralski silicon solar cell architectures on light-induced degradation and regeneration mechanisms," in *Proceedings of the 29th European Photovoltaic Solar Energy Conference and Exhibition*, 2014.

[113] S. Rein, T. Rehrl, W. Warta, S. Glunz, and G. Willeke, "Electrical and thermal properties of the metastable defect in boron-doped czochralski silicon (cz-si)," in *Proceedings of the 17th European Photovoltaic Solar Energy Conference*, p. 1555, 2001.

[114] J. Schmidt, K. Bothe, and R. Hezel, "Formation and annihilation of the metastable defect in boron-doped czochralski silicon," in *Photovoltaic Specialists Conference, 2002. Conference Record of the Twenty-Ninth IEEE*, pp. 178–181, IEEE, 2002.

[115] S. Glunz, E. Schaffer, S. Rein, K. Bothe, and J. Schmidt, "Analysis of the defect activation in cz-silicon by temperature-dependent bias-induced degradation of solar cells," in *Photovoltaic Energy Conversion, 2003. Proceedings of 3rd World Conference on*, vol. 1, pp. 919–922, IEEE, 2003.

[116] S. Glunz, S. Rein, J. Lee, and W. Warta, "Minority carrier lifetime degradation in boron-doped czochralski silicon," *Journal of Applied Physics*, vol. 90, no. 5, pp. 2397–2404, 2001.

[117] J. Schmidt, A. Cuevas, S. Rein, and S. W. Glunz, "Fill factor limitations and non-ideal diode behaviour of czochralski silicon solar cells due to light-induced recombination centres," in *Proceedings of the 17th European Photovoltaic Solar Energy Conference, Munich, Germany*, pp. 1396–1399, 2001.

[118] F. Kersten, P. Engelhart, H.-C. Ploigt, A. Stekolnikov, T. Lindner, F. Stenzel, M. Bartzsch, A. Szpeth, K. Petter, J. Heitmann, *et al.*, "Degradation of multicrystalline silicon solar cells and modules after illumination at elevated temperature," *Solar Energy Materials and Solar Cells*, vol. 142, pp. 83–86, 2015.

[119] alfa img.com, "Phosphorus atom model." http://alfa-img.com/show/3d-atom-model-phosphorus.html.

[120] K. Bothe, J. Schmidt, and R. Hezel, "Effective reduction of the metastable defect concentration in boron-doped czochralski silicon for solar cells," in *Photovoltaic Specialists Conference, 2002. Conference Record of the Twenty-Ninth IEEE*, pp. 194–197, IEEE, 2002.

[121] S. A. Campbell, S. A. Campbell, and A. C. Stephen, *Fabrication engineering at the micro-and nanoscale*. No. Sirsi) i9780195320176, 2008. pages 50-51.

[122] O. Edenhofer, R. Pichs-Madruga, Y. Sokona, E. Farahani, S. Kadner, K. Seyboth, A. Adler, I. Baum, S. Brunner, P. Eickemeier, B. Kriemann, J. Savolainen, S. Schlmer, C. von Stechow, T. Zwickel, and J. M. (eds.), "Climate change 2014: Mitigation of climate change. contribution of working group iii to the fifth assessment report of the intergovernmental panel on climate change," tech. rep., IPCC, Cambridge University Press, Cambridge, United Kingdom and New York, NY, USA, 2014.

[123] M. Galiazzo, A. Voltan, E. Bortoletto, M. Zamuner, M. Martire, O. Borsato, M. Bertazzo, and D. Tonini, "Fine line double printing and advanced process control for cell manufacturing," *Energy Procedia*, vol. 67, pp. 116–125, 2015.

[124] S. Gatz, J. Müller, T. Dullweber, and R. Brendel, "Analysis and optimization of the bulk and rear recombination of screen-printed perc solar cells," *Energy Procedia*, vol. 27, pp. 95–102, 2012.

[125] B. J. Hallam, P. G. Hamer, S. R. Wenham, M. D. Abbott, A. Sugianto, A. M. Wenham, C. E. Chan, G. Xu, J. Kraiem, J. Degoulange, *et al.*, "Advanced bulk defect passivation for silicon solar cells," *IEEE Journal of Photovoltaics*, vol. 4, no. 1, pp. 88–95, 2014.

[126] R. Horbelt, G. Hahn, R. Job, and B. Terheiden, "Void formation on perc solar cells and their impact on the electrical cell parameters verified by luminescence and scanning acoustic microscope measurements," *Energy Procedia*, vol. 84, pp. 47–55, 2015.

[127] T. Lauermann, B. Fröhlich, G. Hahn, and B. Terheiden, "Diffusion-based model of local al back surface field formation for industrial passivated emitter and rear cell solar cells," *Progress in Photovoltaics: Research and Applications*, vol. 23, no. 1, pp. 10–18, 2015.

[128] V. Meemongkolkiat, K. Nakayashiki, D. S. Kim, S. Kim, A. Shaikh, A. Kuebelbeck, W. Stockum, and A. Rohatgi, "Investigation of modified screen-printing al pastes for local back surface field formation," in *2006 IEEE 4th World Conference on Photovoltaic Energy Conference*, vol. 2, pp. 1338–1341, IEEE, 2006.

[129] I. Périchaud, "Gettering of impurities in solar silicon," *Solar Energy Materials and Solar Cells*, vol. 72, no. 1, pp. 315–326, 2002.

[130] Rfassbind, "Price history chart of crystalline silicon solar cells in us$ per watt since 1977," *Wikipedia The Free Encyclopedia. Wikimedia Foundation, Inc. Web. (source - Bloomberg, New Energy Finance(1977-2013) & EnergyTrend.com(2013-2015)*, 2015.

[131] E. Seale, "Photovoltaic (effect)," *http://encyclobeamia.solarbotics.net/articles/photovoltaic.html*, 2003.

[132] SEIA, "Q2 2015 solar market insight fact sheet," tech. rep., Solar Energy Industries Association, 2015.

[133] J. Tsao, N. Lewis, and G. Crabtree, "Solar faqs," *US department of Energy*, 2006.

[134] D. S. W. T. F. Encyclopedia.), "ion implantation," *Wikimedia Foundation Inc. Web.*, July 3rd, 2005.

[135] F. Ye, W. Deng, W. Guo, R. Liu, D. Chen, D. Chen, Y. Chen, Y. Yang, N. Yuan, J. Ding, Z. Feng, *et al.*, "22.13perc solar cell," *PVSC*, 2016.

[136] J. Zhao, A. Wang, and M. A. Green, "24· 5% efficiency silicon pert cells on mcz substrates and 24· 7% efficiency perl cells on fz substrates," *Progress in Photovoltaics: Research and Applications*, vol. 7, no. 6, pp. 471–474, 1999.

VITA

Eunhwan Cho was born in Seoul, South Korea in 1984. He received the B.S. degree in electrical and computer engineering from Hanyang University, Seoul, South Korea, in 2010 and the M.S. degree in electrical and computer engineering from Georgia Institute of Technology, Atlanta, GA, USA, in 2013. He joined the Ph.D. program at the School of Electrical and Computer Engineering, Georgia Institute of Technology, Atlanta, GA, USA, in 2011. He has been a graduate research assistant at the University Center of Excellence Photovoltaics (UCEP) under the supervision of Dr. Ajeet Rohatgi since 2012. His research interests are modeling, fabrication and characterization of high-efficiency silicon solar cells. During his Ph.D. research, he published 11 papers in high-impact peer-reviewed journals and international refereed conference proceedings.